

# Surveys of clumps, cores, and condensations in Cygnus X

## Temperature and nonthermal velocity dispersion revealed by VLA NH<sub>3</sub> observations<sup>\*</sup>

X. Zhang<sup>1,2,3</sup>, K. Qiu<sup>1,3</sup>, Q. Zhang<sup>4</sup>, Y. Cao<sup>1,3</sup>, Y. Cheng<sup>5</sup>, J. Liu<sup>5</sup>, Y. Wang<sup>1,3</sup>, X. Lu<sup>6</sup>, and X. Pan<sup>1,3,4</sup>

<sup>1</sup> School of Astronomy and Space Science, Nanjing University, 163 Xianlin Avenue, Nanjing 210023, PR China  
e-mail: kpqiu@nju.edu.cn

<sup>2</sup> Max-Planck-Institut für Radioastronomie, Auf dem Hügel 69, 53121 Bonn, Germany

<sup>3</sup> Key Laboratory of Modern Astronomy and Astrophysics (Nanjing University), Ministry of Education, Nanjing 210023, PR China

<sup>4</sup> Center for Astrophysics | Harvard & Smithsonian, 160 Concord Avenue, Cambridge, MA 02138, USA

<sup>5</sup> National Astronomical Observatory of Japan, 2-21-1 Osawa, Mitaka, Tokyo, 181-8588, Japan

<sup>6</sup> Shanghai Astronomical Observatory, Chinese Academy of Sciences, 80 Nandan Road, Shanghai 200030, PR China

Received January 21, 2023; accepted February 15, 2024

### ABSTRACT

**Context.** The physical properties, evolution, and fragmentation of massive dense cores (MDCs,  $\sim 0.1$  pc) are fundamental pieces in our understanding of high-mass star formation.

**Aims.** We aim to characterize the temperature, velocity dispersion, and fragmentation of the MDCs in the Cygnus X giant molecular cloud and to investigate the stability and dynamics of these cores.

**Methods.** We present the Karl G. Jansky Very Large Array (VLA) observations of the NH<sub>3</sub> ( $J, K$ ) = (1,1) and (2,2) inversion lines towards 35 MDCs in Cygnus X, from which we calculated the temperature and velocity dispersion. We extracted 202 fragments ( $\sim 0.02$  pc) from the NH<sub>3</sub> (1,1) moment-0 maps with the GAUSSCLUMPS algorithm. We analyzed the stability of the MDCs and their NH<sub>3</sub> fragments through evaluating the corresponding kinetic, gravitational potential, and magnetic energies and the virial parameters.

**Results.** The MDCs in Cygnus X have a typical mean kinetic temperature  $T_K$  of  $\sim 20$  K. Our virial analysis shows that many MDCs are in subvirialized states, indicating that the kinetic energy is insufficient to support these MDCs against their gravity. The calculated nonthermal velocity dispersions of most MDCs are at transonic to mildly supersonic levels, and the bulk motions make only a minor contribution to the velocity dispersion. Regarding the NH<sub>3</sub> fragments, with  $T_K \sim 19$  K, their nonthermal velocity dispersions are mostly trans-sonic to subsonic. Unless there is a strong magnetic field, most NH<sub>3</sub> fragments are probably not in virialized states. We also find that most of the NH<sub>3</sub> fragments are dynamically quiescent, while only a few are active due to star formation activity.

**Key words.** Stars: formation – ISM: kinematics and dynamics – Stars: massive – ISM: molecules

## 1. Introduction

High-mass stars ( $> 8 M_\odot$ ) play a vital role in shaping their host galaxies via their intense feedback effects in the form of powerful outflows, strong stellar winds, and violent UV radiation (Motte et al. 2018). However, the formation of high-mass stars is still an open question. Unlike the star formation model built in low-mass stars (Shu et al. 1993), accretion onto high-mass protostars is difficult to model because of the radiation pressure problem (Wolfire & Cassinelli 1987) and the violent wind (Krumholz 2015). In observations, it is difficult to catch the high-mass stellar embryos as their birthplaces are usually far away and deeply embedded (Zinnecker & Yorke 2007). The small populations and short timescales of critical evolutionary phases mean that the sample of high-mass stellar embryos is even more insufficient (Zinnecker & Yorke 2007).

Several candidate theories of high-mass star formation have been proposed, such as competitive accretion in protostellar

clusters (Bonnell et al. 1997, 2001), mergers of protostars (Bonnell et al. 1998), turbulent core accretion (McKee & Tan 2003), and inertial inflow (Padoan et al. 2020). To verify these theories, it is necessary to observationally investigate the initial conditions of high-mass star formation. Observations with a range of tracers in a variety of wavelengths and resolutions have been carried out towards massive dense cores (MDCs), the possible birth places of high-mass stars (e.g., Beuther et al. 2002; Motte et al. 2007; Lu et al. 2014; Rathborne et al. 2016; Cao et al. 2019; Zhang et al. 2019). By characterizing the physical conditions of high-mass star formation with observations, we can test and provide practical constraints to the corresponding theories.

The CENSUS project (Surveys of Clumps, CorEs, and CoNdenSations in CygnUS X, PI: Keping Qiu) is dedicated to a systematic study of the 0.01–10 pc hierarchical molecular structures and the high-mass star formation process in the molecular complex Cygnus X. In order to investigate the temperature structures and dynamic conditions of MDCs in our project, we make use of the NH<sub>3</sub> (1,1) and (2,2) inversion emission lines, which trace gas with critical density of  $\sim 10^4$  cm<sup>-3</sup> and excitation temperature of  $\sim 10$ –30 K (Ho & Townes 1983; Mangum & Shirley 2015). These lines are widely used for studying the initial conditions of

\* Table of the physical parameters of NH<sub>3</sub> fragments is only available in electronic form at the CDS via anonymous ftp to cdsarc.u-strasbg.fr (130.79.128.5) or via <http://cdsweb.u-strasbg.fr/cgi-bin/qcat?J/A+A/> after publishing.

star formation. Previous NH<sub>3</sub> surveys find a mean temperature of  $\lesssim 15$  K in less-evolved structures and  $\sim 20$  K in protostellar cores with significant star-forming activity (e.g., Pillai et al. 2006; Wu et al. 2006; Chira et al. 2013; Kerr et al. 2019). The velocity dispersion of these lines is found to be dominated by nonthermal components in most cases (e.g., Lu et al. 2014; Billington et al. 2019). Furthermore, analyses of the dynamical stability of star-forming structures at various scales and evolutionary stages can be done with these lines via the virial analysis (e.g., Jijina et al. 1999; Zhang et al. 2020). Therefore, a high-resolution unbiased NH<sub>3</sub> survey towards the MDCs in the Cygnus X cloud complex offers a remarkable observational sample that can be used to unravel the initial conditions of high-mass star formation.

The Cygnus X cloud, located at 1.4 kpc from the Sun (Rygl et al. 2012), is one of the richest and most active molecular and HII complexes in the Galaxy. It is massive ( $\sim 4 \times 10^6 M_{\odot}$ ) and large (extends over  $\sim 100$  pc in diameter) (Leung & Thaddeus 1992), and consists of substantial HII regions (Wendker et al. 1991) and OB associations (Uyaniker et al. 2001). All these features make Cygnus X an ideal object for studying high-mass star formation. Several surveys and numerous case studies towards Cygnus X have been carried out over recent decades (e.g., Motte et al. 2007; Gottschalk et al. 2012; Takekoshi et al. 2019). The CENSUS project has published several works on Cygnus X: Cao et al. (2019) generated a complete sample of MDCs in Cygnus X and performed an analysis of their far-infrared emission; Wang et al. (2022) provide radio continuum views of the MDCs; Pan et al. (2023) provide a survey of the possible circumstellar disks in Cygnus X; Yang et al. (2023) analyzed the high-velocity outflow using Submillimeter Array (SMA) observations of SiO (5-4). In the CENSUS project, we adopt the terminology that clumps, cores, and condensations correspond to cloud structures of a physical full width at half maximum (FWHM) size of  $\sim 1$ ,  $\sim 0.1$ , and  $\sim 0.01$  pc, respectively, which is also widely used in other studies (e.g., Pokhrel et al. 2018; Zhang et al. 2019).

As a part of CENSUS, we report an unbiased NH<sub>3</sub> survey towards 37 fields in Cygnus X observed with the Karl G. Jansky Very Large Array (VLA) with a spatial resolution of  $\sim 0.02$  pc. This paper is organized as follows. Section 2 outlines details of the sample and observational setups. In Sect. 3, we describe the methods we used to analyze the NH<sub>3</sub> data. The derived physical parameters and their distributions and correlations are presented in Sect. 4. The NH<sub>3</sub> morphology, a virial analysis, the dynamical states of MDCs, and a comparison between dust and gas temperatures are discussed in Sect. 5. Finally, the study is summarized in Sect. 6, where we outline our conclusions.

## 2. Sample and observations

### 2.1. Sample selection

The interferometer observations of the CENSUS project (PI: Keping Qiu, also see Cao et al. 2019) were designed to target most MDCs in Cygnus X (Wang et al. 2022). We first selected 42 sources with estimated masses of greater than  $30 M_{\odot}$  from Motte et al. (2007), though one source (S26) was later found to be outside of Cygnus X (Rygl et al. 2012) and another (N58) should have a much lower mass (see Table 1 for more details). In this work, we exclude 10 sources in the DR 21 region, which were observed by the VLA in a mosaic setup (Project ID: 14A-241; PI: Qizhou Zhang) and will be presented in a separate work. The other 32 sources, as well as an additional source (NW12, see Table 1 for more details), were observed with the VLA in 29 fields. In the present work, we also include VLA observations

of another eight fields covering bright JCMT SCUBA-2 sources (Cao et al. 2019) located in the OB2 association region<sup>1</sup>. Here, VLA observations of a total of 37 fields are therefore presented (Table 1). As part of the CENSUS project, Cao et al. (2021) constructed a column density map of the entire Cygnus X complex based on SED fitting of multiband Herschel observations and extracted more than 8000 cores with the *getsources* algorithm. In the following analysis, we adopt the parameters of dense cores from Cao et al. (2021).

### 2.2. Very Large Array

The NH<sub>3</sub> data were obtained from the NRAO<sup>2</sup> VLA program 17A-107 (PI: Keping Qiu), which observed with 27 antennas in the D-array configuration. The program 17A-107 is an unbiased and high-resolution survey dedicated to observing the NH<sub>3</sub> (J,K)=(1,1), (2,2), (3,3), (4,4), and (5,5) rotation-inversion transitions, CCS (1,2-2,1) and CCS (6,5-5,5) emissions, and H<sub>2</sub>O maser lines for MDCs in Cygnus X. The baselines of the array range from 0.035 km to 1.03 km, corresponding to the largest recoverable angular scale of  $\sim 66''$  (0.45 pc for Cygnus X) and an angular resolution of  $\sim 3''.1$  (0.02 pc for Cygnus X), respectively. The correlator setup provides eight independent spectral windows with a spectral channel spacing of 7.8 kHz and a bandwidth of 8 MHz, corresponding to a velocity resolution of 0.1 km s<sup>-1</sup> and a velocity coverage of 100 km s<sup>-1</sup> for the NH<sub>3</sub> (1,1) and (2,2) lines.

The VLA data were calibrated using the Common Astronomy Software Applications (CASA) package (McMullin et al. 2007). The flux calibrator and bandpass calibrator were both set as the quasar 1331+305 (3C286). Gain calibration was performed with observations of J2007+4029. The calibrated data were imaged using the CASA task *clean*, gridded with a pixel size of  $1''$ . The rms of these fields is  $\lesssim 0.013$  Jy beam<sup>-1</sup> in a 0.1 km s<sup>-1</sup> channel width. The coordinates of the field centers and noise levels are also listed in Table 1. The NH<sub>3</sub> (1,1) and (2,2) emission lines are the main interests of this paper. The rest frequencies of the (1,1) and (2,2) emission lines are 23.6945 and 23.72263 GHz, while upper energy levels are 23.4 and 64.9 K, respectively. Observations of the other spectral lines in 17A-107 are beyond the scope of this paper, and are listed in Appendix A.

### 2.3. MIR archive data from the Spitzer Space Telescope

We use the *Spitzer* IRAC 3.6, 4.5, and 8.0  $\mu\text{m}$  data from the *Spitzer* Legacy Survey of the Cygnus X Complex<sup>3</sup> (Kraemer et al. 2010) in this paper, which are downloaded from the NASA/IPAC Infrared Science Archive<sup>4</sup>. All these data cover the entire Cygnus X region, with a pixel size of  $2''$  and  $1\sigma$  rms noise levels of 25.1, 27.1, and 47.9 MJy.sr<sup>-1</sup>, respectively.

## 3. Methods

We checked detections in all data cubes before fitting the NH<sub>3</sub> lines. In order to determine whether there is detection in a spec-

<sup>1</sup> these sources were not included by Motte et al. (2007) as the OB2 region has a lower extinction while Motte et al. (2007) extracted sources from high-extinction regions.

<sup>2</sup> The National Radio Astronomy Observatory is a facility of the National Science Foundation operated under cooperative agreement by Associated Universities, Inc.

<sup>3</sup> <https://www.cfa.harvard.edu/cygnusX/>

<sup>4</sup> <http://irsa.ipac.caltech.edu/frontpage/>

trum, the NH<sub>3</sub> (1,1) data cubes are smoothed to a velocity resolution of 0.7 km s<sup>-1</sup>, or seven spectral channels in our observations, to improve signal-to-noise ratios (S/Ns). The criterion of significant detection within a beam is set as S/N ≥ 5 in the smoothed NH<sub>3</sub> (1,1) data. The corresponding original spectra were fitted in the following processes if their smoothed spectra exceeded the threshold. The detections and noise levels in all the fields are reported in Table 2. The detections in fields are marked as marginal if the emissions are only detected in one or two beams. We adopt the distance of 1.4 kpc (Rygl et al. 2012) for all the fields except for Field 21 (also known as AFGL2591), of which the distance is 3.3 kpc (Rygl et al. 2012).

### 3.1. Ammonia line fitting

Following the theoretical framework in Mangum & Shirley (2015), we built spectral models of the NH<sub>3</sub> (1,1) and (2,2) emission with the centroid velocity, line width, excitation temperature, NH<sub>3</sub> column density in the upper transition state, and beam-filling factor as free parameters and with the following assumptions: (1) the same beam-filling factor and excitation temperature for all hyperfine transitions; (2) local thermodynamic equilibrium (LTE). The NH<sub>3</sub> (1,1) and (2,2) data cubes were fitted simultaneously using the model to derive the aforementioned physical parameters.

We can get the relationship between the brightness temperature and excitation temperature as

$$T_B = f(T_{\text{ex}} - T_{\text{bg}})(1 - e^{-\tau_\nu}), \quad (1)$$

where  $f$  is the beam-filling factor and  $T_{\text{bg}}$  is the background temperature. We take the temperature of cosmic microwave background (CMB) as  $T_{\text{bg}}$ , which is 2.73K. The optical depth  $\tau_\nu$  can be written as

$$\tau_\nu = \frac{hc^3 N_u A_{ul}}{8\pi\nu^2 k_B T_{\text{ex}}} \Phi_\nu, \quad (2)$$

where  $N_u$  is the column density of molecules in the upper transition state. Here, we assume a Gaussian profile,

$$\Phi_\nu = \frac{1}{\sqrt{2\pi}\Delta\nu} e^{-\frac{(\nu-\nu_0)^2}{2(\Delta\nu)^2}}, \quad (3)$$

where  $\nu_0$  is the central frequency of the emission. The Einstein coefficient  $A_{ul}$  is

$$A_{ul} \equiv \frac{64\pi^4 \nu^3 \mu_{lu}^2}{3hc^3} \cdot \frac{K^2}{J(J+1)} \cdot R_s, \quad (4)$$

where  $\mu_{lu}$  and  $R_s$  are the permanent dipole moment of NH<sub>3</sub> and the relative strengths of the hyperfine structures, respectively. In our model,  $R_s$  is set as 1/2, 5/36, and 1/9 for the main, inner satellite, and outer satellite components of NH<sub>3</sub> (1,1) emission, respectively. As for the main and inner satellite components of NH<sub>3</sub> (2,2) emission,  $R_s$  is set as 0.796 and 0.052, respectively. We can derive the total NH<sub>3</sub> column density  $N_{\text{tot}}$  from the relationship between  $N_u$  and  $N_{\text{tot}}$  (Boltzmann distribution),

$$\frac{N_{\text{tot}}}{N_u} = \frac{Q_{\text{rot}}}{g_u} e^{\frac{E_u}{kT_{\text{ex}}}}, \quad (5)$$

where the rotation partition function  $Q_{\text{rot}} \approx 168.7\sqrt{T_{\text{ex}}^3/B^2C}$  ( $B = 298.117$  GHz,  $C = 186.726$  GHz), and  $g_u$  is the total degeneracy for the upper energy level, which can be found in Mangum & Shirley (2015).

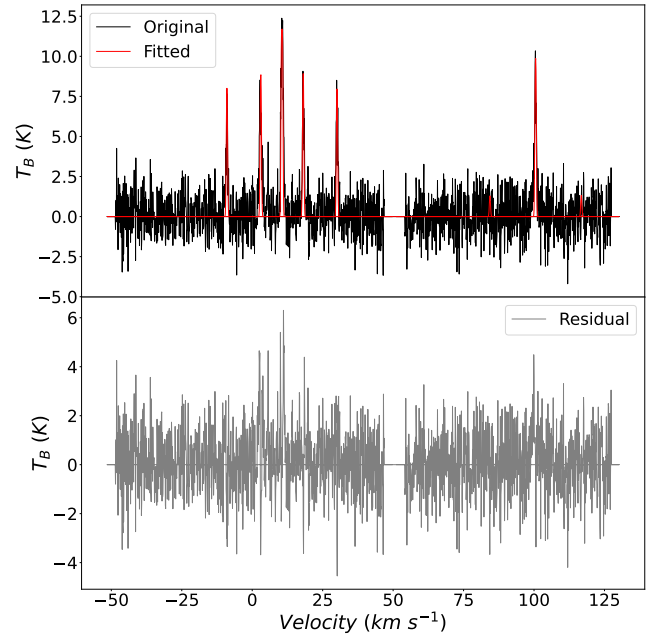


**Fig. 1.** Example five-component-fitting results on NH<sub>3</sub> (1,1) and (2,2) emission (pixel coordinate (142,131) in Field 3). Upper panel: Original spectrum and the fitted result are colored in black and red, respectively. Lower panel: Residual spectrum of this fitting result.

Using these formulas, we built a blended spectral model rather than the all-hyperfine model after comparing their fitted results. This model consists of five Gaussian components for NH<sub>3</sub> (1,1) emission and three Gaussian components for NH<sub>3</sub> (2,2) emission. We do not include the two outer satellite components in our model as most NH<sub>3</sub> (2,2) lines do not show remarkable satellite components in our data. The excitation temperature and the column density are derived only when the S/Ns of the (2,2) moment-0 maps are greater than 2 in order to avoid large uncertainties.

We then fitted the NH<sub>3</sub> (1,1) and (2,2) simultaneously with five Gaussian components for (1,1) emission and three Gaussian components for (2,2) emission. An example result is shown in Fig. 1.

### 3.2. Temperature threshold and kinetic temperature

Regarding the NH<sub>3</sub> inversion emission lines, the excitation temperature refers to the rotation temperature of NH<sub>3</sub>,  $T_{\text{rot}}$ . We set the upper limit and lower limit of  $T_{\text{rot}}$  in the fitting processes to 50 K and 8 K, respectively. The lower limit refers to the typical temperature of interstellar molecular clouds without star-forming activity, that is, ~10K, and the upper bound corresponds to the fact that the NH<sub>3</sub> (1,1) and (2,2) lines cannot be a good temperature probe when the  $T_{\text{rot}}$  of the gas exceeds ~30 K.

To obtain the kinetic temperature,  $T_K$ , from  $T_{\text{rot}}$ , we employ the empirical approximation provided by Ott et al. (2011),

$$T_K = 6.06e^{0.061(T_{\text{rot}}/K)}. \quad (6)$$

The temperature mentioned hereafter refers to the kinetic temperature.

Tafalla et al. (2004) and Swift et al. (2005) also derived  $T_{\text{rot}}-T_K$  relations. Comparing these results, we find that the empirical approximation from Ott et al. (2011) applies for a wider range of  $T_{\text{rot}}$  ( $T_{\text{rot}} \lesssim 500$  K), while the ranges are  $5 \text{ K} < T_{\text{rot}} < 20 \text{ K}$  and

**Table 1.** Observational fields and related MDCs

Field	MDCs (Cao21) <sup>a</sup>	MDCs (Motte07) <sup>b</sup>	R.A. (J2000)	Decl. (J2000)	Beam <sup>c</sup> ("×"; °)
1	220	N3	20:35:34.6	42:20:08.8	3.3×2.6; -29.0
2	341	N63	20:40:05.4	41:32:13.1	3.1×2.5; -24.0
3	274 584	N6	20:36:07.3	41:39:58.0	4.5×3.1; -69.0
4	725 1919	N10	20:35:52.2	41:36:23.0	4.5×3.1; -69.0
5	248 774 <sup>d</sup> 1669	N12	20:36:57.4	42:11:27.0	3.5×3.4; 61.0
6	714	N14	20:37:00.9	41:34:57.0	4.3×3.0; -69.0
7	1267 3188 6479	N24	20:38:04.6	42:39:54.0	3.5×3.3; 61.0
8	698 1179	N56	20:39:16.9	42:16:07.0	3.6×3.3; 58.0
9	532	N58 <sup>e</sup>	20:39:25.9	41:20:01.0	3.5×3.4; -11.0
10	801	N65	20:40:28.4	41:57:11.0	4.8×3.2; -72.0
11	684	N68	20:40:33.5	41:59:03.0	4.6×3.1; -71.0
12	4315 4797	N69	20:40:33.7	41:50:59.0	4.5×3.1; -69.0
13	327 619 742 <sup>d</sup>	NW1 NW2	20:19:39.0	40:56:45.0	4.4×3.0; -63.0
14	640 675	NW5	20:20:30.5	41:21:40.0	3.5×3.0; -70.0
15	839 <sup>e</sup>	NW12 <sup>f</sup>	20:24:14.3	42:11:43.0	3.5×3.0; -70.0
16	310	NW14	20:24:31.7	42:04:23.0	3.6×3.0; -70.0
17	507 753	S7 S8	20:20:38.6	39:38:00.0	4.1×3.0; -80.0
18	798	S10	20:20:44.4	39:35:20.0	4.0×2.9; -75.0
19	874	S15	20:27:14.0	37:22:58.0	3.5×3.1; -61.0
20	1201 1537	S18 S20	20:27:26.7	37:22:45.0	3.5×3.0; -61.0
21	277 <sup>g</sup>	S26 <sup>g</sup>	20:29:24.6	40:11:19.1	3.2×2.6; 54.0
22	723	S29	20:29:58.8	40:15:58.0	3.3×3.0; 87.0
23	509	S30	20:31:12.6	40:03:16.0	3.3×2.9; -87.0
24	351	S32	20:31:20.3	38:57:16.0	3.3×2.9; -86.0
25	1225	S34	20:31:57.8	40:18:30.0	4.7×3.3; -75.0
26	1454 2210	S37	20:32:28.6	40:19:41.5	3.5×3.0; -70.0
27	892	S41	20:32:33.4	40:16:43.0	3.5×3.0; -70.0
28	540	S43	20:32:40.8	38:46:31.0	3.3×2.9; -89.0
29	1460	–	20:35:00.0	41:34:57.0	5.0×2.9; -69.0
30	608	–	20:34:00.0	41:22:25.0	4.9×2.9; -68.0
31	302 520	–	20:35:09.5	41:13:30.0	4.3×3.0; -71.0
32	340	–	20:32:22.5	41:07:56.0	4.0×3.0; -69.0
33	2976	–	20:32:17.0	41:09:10.0	4.4×3.0; 86.0
34	214 247	–	20:30:28.5	41:15:55.0	3.6×3.0; -69.0
35	370 893	–	20:28:09.4	40:52:50.0	4.0×3.0; -61.0
36	–	–	20:28:05.5	40:51:17.0	3.9×3.0; -59.0
37	1112 1231 1244	N30 N32	20:38:36.4	42:37:34.8	3.3×2.6; -29.0

**Notes.** <sup>(a)</sup> MDCs from Cao et al. (2021) covered by the field. <sup>(b)</sup> MDCs in Motte et al. (2007) covered by the field, extracted from 1.2 mm continuum data from IRAM 30-m telescope (with effective angular resolution of  $\sim 11''$  and spatial resolution of  $\sim 0.09$  pc). <sup>(c)</sup> The beams are shown as “major axes  $\times$  minor axes; position angles”. <sup>(d)</sup> Dense core 774 and 742 have mass of 25.0 and 19.4  $M_{\odot}$ , slightly lower than 30  $M_{\odot}$ . However, both of them have remarkable NH<sub>3</sub> detections in our observations. We therefore took them into the following analysis and do not distinguish them from other MDCs. <sup>(e)</sup> The mass of N58 could be highly overestimated in Motte et al. (2007) due to the significant contribution of free-free emission in this core. N58 is therefore excluded from the sample in Wang et al. (2022). However, MDC 532 is included in this work as the SED-fitted mass of MDC 532 is 68.6  $M_{\odot}$ , which is still larger than 30  $M_{\odot}$ . <sup>(f)</sup> NW12 is an interesting isolated core in its parental clump. It is covered by VLA 14A-107 though its mass is lower than 30  $M_{\odot}$ . The mass of MDC 839 extracted by Cao et al. (2021) is also lower than 30  $M_{\odot}$ . <sup>(g)</sup> S26, also known as AFGL 2591, is excluded from our sample due to its different distance from Cygnus X region, of namely 3.3 kpc (Rygl et al. 2012).

$T_K \ll 41$  K for the relations in Tafalla et al. (2004) and Swift et al. (2005), respectively. In our results, a remarkable number of detections are hotter than 20 K, which is why we choose the relation from Ott et al. (2011).

### 3.3. Intrinsic line width and velocity dispersion

The line width derived from our fitting is blended by several hyperfine lines, because we do not conduct the full-hyperfine fitting. To derive the intrinsic line width that truly reflects the gas motion, we firstly subtract the channel width ( $0.1 \text{ km s}^{-1}$ ) from the FWHM line widths derived from the line fitting quadrati-

cally. We then apply the following empirical relation of Baranco & Goodman (1998) to eliminate the effect of hyperfine-line blending:

$$\Delta v_{\text{int}} = \sum_{n=0}^3 C_n(\tau_0) \Delta v_{\text{blended}}^n, \quad (7)$$

where  $C_n(\tau_0)$  is given as

$$C_n(\tau_0) = K_{n0} + K_{n1} e^{-K_{n2} \tau_0}. \quad (8)$$

Here,  $\tau_0$  is the total optical depth of NH<sub>3</sub> (1,1) emission. We take the optical depth of the NH<sub>3</sub> (1,1) main line,  $\tau_{11,m}$ , as the approximation of  $\tau_0$ . The conversion coefficient,  $K_{nm}$ , is listed in Table

**Table 2.** Detections in each field

Field	NH <sub>3</sub> detection <sup>a</sup>					r.m.s. level		Smoothed S/N (peak) <sup>b</sup>		H <sub>2</sub> O masers <sup>c</sup>
	(1,1)	(2,2)	(3,3)	(4,4)	(5,5)	(mJy Beam <sup>-1</sup> )	(K)	(1,1)	(2,2)	
1	√	√	×	×	×	11.5	3.0	11.7	11.0	–
2	√	√	×	×	×	9.7	2.8	7.9	6.0	–
3	√	√	–	–	–	7.5	1.2	25.2	16.8	1
4	√	√	√	–	–	8.0	1.3	19.9	15.9	–
5	√	√	√	√	*	6.5	1.2	32.2	20.3	1
6	√	√	√	*	–	7.8	1.3	12.1	7.2	1
7	√	√	–	–	–	6.5	1.2	18.7	10.2	2
8	√	√	√	*	–	6.1	1.1	27.4	17.2	1
9	√	√	–	–	–	9.2	1.7	9.8	7.7	–
10	√	√	√	–	–	9.5	1.4	16.5	11.1	–
11	√	√	√	–	–	9.2	1.4	19.5	9.2	1
12	√	√	–	–	–	9.1	1.4	17.4	7.6	1
13	√	√	√	–	–	8.5	1.4	26.4	19.4	–
14	√	√	–	–	–	8.4	1.7	14.7	5.7	1
15	√	–	–	–	–	8.4	1.7	7.4	–	–
16	√	√	*	–	–	8.2	1.6	15.0	6.9	1
17	√	√	√	–	–	6.8	1.2	33.7	20.3	2
18	√	√	–	–	–	6.6	1.3	20.9	10.8	–
19	√	√	–	–	–	8.2	1.6	20.9	14.7	–
20	√	√	–	–	–	8.8	1.9	17.3	13.7	2
21	√	√	√	√	√	7.6	1.9	14.9	9.3	2
22	√	√	–	–	–	6.8	1.5	15.0	7.1	–
23	√	√	√	–	–	7.0	1.6	22.2	13.2	3
24	√	√	√	–	–	7.4	1.7	16.7	8.8	–
25	√	√	–	–	–	8.4	1.2	18.6	8.6	3
26	√	√	–	–	–	7.8	1.6	17.4	10.9	–
27	√	√	√	–	–	7.5	1.5	22.2	20.6	–
28	√	√	–	–	–	7.4	1.7	23.0	13.9	–
29	√	√	–	–	–	11.6	1.7	11.6	7.6	–
30	–	–	–	–	–	11.8	1.8	–	–	–
31	√	√	–	–	–	8.5	1.4	11.8	8.3	–
32	√	√	–	–	–	7.0	1.2	22.8	12.4	1
33	√	*	–	–	–	8.9	1.5	13.6	7.7	–
34	√	√	√	–	–	6.5	1.3	26.8	19.5	1
35	–	–	–	–	–	10.8	2.0	–	–	–
36	–	–	–	–	–	11.2	2.1	–	–	–
37	√	√	×	×	×	12.0	3.1	11.3	10.4	–

**Notes.** <sup>(a)</sup> √ for remarkable detection, \* for marginal detection, and – for nondetection. × shows the lack of related cubes as we only obtain NH<sub>3</sub> (1,1) and (2,2) cubes for Fields 1, 2, and 37. <sup>(b)</sup> Nondetection cases are shown as – <sup>(c)</sup> The number of H<sub>2</sub>O maser spots.

3. As a polyfit result, this relation has its limitations for large FWHM line widths, which will make  $\Delta v_{\text{int}}$  larger than  $\Delta v_{\text{blended}}$ . In this case, we use  $\Delta v_{\text{blended}}$  as an approximation of  $\Delta v_{\text{int}}$ ; that is,  $\Delta v_{\text{int}} \approx \Delta v_{\text{blended}}$ . Furthermore, we also tested the full-hyperfine fitting in Fields 3 and 5 and compared the fitted line width with that derived from our fitting results. In Field 3, the mean and median differences between the line widths from these two fitting methods are 0.034 and 0.027 km s<sup>-1</sup> (5.4% and 6.7% for relative deviations, respectively). Regarding Field 5, these values are 0.062 (2.4%) and 0.008 (1.5%) km s<sup>-1</sup>, respectively. The empirical relation is therefore reliable and the differences are totally negligible.

The intrinsic line width can be further decomposed into  $\Delta v_{\text{int}}^2 = 8 \ln 2 \times (\sigma_{v_{\text{t,NH}_3}}^2 + \sigma_{v_{\text{t,NT}}}^2)$ , where  $\sigma_{v_{\text{t,NH}_3}}$  is the thermal velocity dispersion of NH<sub>3</sub> and  $\sigma_{v_{\text{t,NT}}}$  is the nonthermal component. We can calculate the thermal velocity dispersion via  $\sigma_{v_{\text{t,m}}} = 0.288 \text{ km s}^{-1} \cdot (m/m_{\text{H}})^{-1/2} \cdot (T_{\text{K}}/10\text{K})^{1/2}$ . Thus, we can derive the nonthermal velocity dispersion  $\sigma_{v_{\text{t,NT}}}$ . Taking the molec-

**Table 3.** Values of  $K_{nm}$ 

m	n			
	0	1	2	3
0	-0.3308	0.8572	-0.1062	0.0152
1	-0.6072	1.8001	-0.9679	0.2179
2	0.1808	0.1932	0.2479	0.2950

ular weight per mean free particle of typical interstellar molecular gas as 2.33  $m_{\text{H}}$  (Kauffmann et al. 2008), we can calculate the thermal velocity dispersion of the whole molecular gas,  $\sigma_{v_{\text{t,ISM}}}$ . We then derive the total velocity dispersion for the whole molecular gas from

$$\sigma_v = \sqrt{\sigma_{v_{\text{t,NT}}}^2 + \sigma_{v_{\text{t,ISM}}}^2}. \quad (9)$$

We refer to  $\sigma_v$  when we discuss velocity dispersion in the following context.

### 3.4. Uncertainties of the results

The uncertainties of the derived physical parameters could originate from both the observational process and the data reduction, including the missing flux, the calibration errors, the systematic errors of the calculating algorithms we use, and so on. The uncertainty of kinetic temperatures comes from two processes: the calculation of  $T_{\text{rot}}$  and the transformation from  $T_{\text{rot}}$  to  $T_K$ . Here,  $T_{\text{rot}}$  is mainly determined by the ratio of the main components of the  $\text{NH}_3$  (1,1) and (2,2) inversion lines. In this process, the uncertainty of  $T_{\text{rot}}$  is  $\sim 10.3/S/N$  K, where  $S/N$  is the signal-to-noise ratio of the  $\text{NH}_3$  (2,2) inversion line (Li et al. 2003). The  $S/N$ s of our results range from  $\sim 2$  to  $\geq 15$ , corresponding to the rms errors from  $\sim 5.2$  to  $\leq 0.69$  K. For the transformation process, we expect an uncertainty of  $\sim 4$  K according to Ott et al. (2011).

Regarding the velocity dispersion, there are three physical parameters involved in its calculation: the blended line width, the optical depth, and the kinetic temperature. The optical depth has little effect on the calculation of intrinsic line width (Barranco & Goodman 1998). According to Lu et al. (2014), the uncertainty of the blended line width can be written as

$$\frac{\delta\Delta v}{\Delta v} = \frac{1}{2} \frac{\delta F}{F}, \quad (10)$$

where  $F$  is the flux intensity.  $\delta F/F$  is estimated to be  $\sim 30\%$  in our data, indicating an uncertainty on the blended line width of  $\sim 15\%$ . The empirical relation between  $\Delta v_{\text{int}}$  and  $\Delta v_{\text{blended}}$  would increase this uncertainty to about 30%. Coupled with the uncertainty of kinetic temperatures, the uncertainty of the velocity dispersion could be  $\geq 30\%$ .

## 4. Results

### 4.1. Moment-0 maps and fragment extraction

In order to show the distributions of the spectral lines, we produce the moment-0 maps of all fields by integrating their intensities in the velocity ranges of the  $\text{NH}_3$  (1,1) main components. The  $\text{NH}_3$  (1,1) and (2,2) moment-0 maps of Field 3 are shown as an example in Fig. 2. The  $\text{NH}_3$  (1,1) and (2,2) moment-0 maps are plotted from  $3\sigma$  and  $2\sigma$  levels, respectively. Moment-0 maps of other fields and the other emission lines are presented in Appendix A.

As mentioned in Sect. 1, the  $\text{NH}_3$  (1,1) moment-0 maps could roughly illustrate the distribution of cold dense gas in our MDCs. We extracted 202 fragments from the  $\text{NH}_3$  (1,1) moment-0 maps using the Starlink GAUSSCLUMPS algorithm (Berry et al. 2007; Currie et al. 2014). The field 21 was excluded from the extraction as it is not at the distance of Cygnus X. The results of the identified  $\text{NH}_3$  fragments in Field 3 are also plotted in Fig. 2 with blue ellipses. In addition, the sizes of  $\text{NH}_3$  fragments are defined as the deconvolved radius, following

$$R = \sqrt{ab - \frac{1}{4\ln 2} \text{beam}_{\text{maj}} \text{beam}_{\text{min}}}, \quad (11)$$

where  $a$  and  $b$  are the semi-major and semi-minor axes of  $\text{NH}_3$  fragments.

We also show the positions of the condensations identified in the SMA 1.3 mm continuum data from Cao et al. (2021).

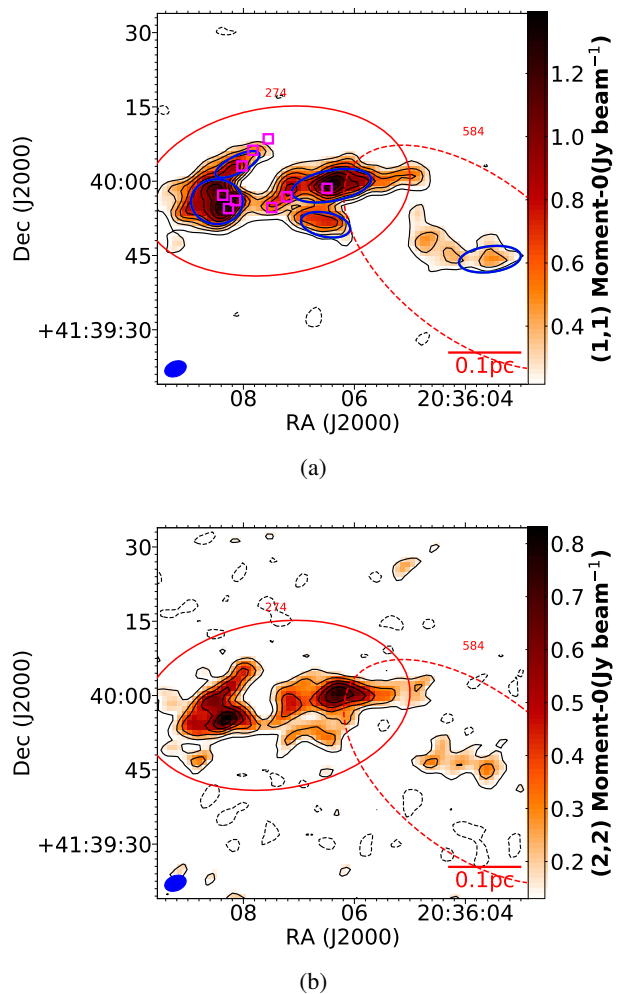


**Fig. 2.** (a) Moment-0 map of the  $\text{NH}_3$  (1,1) line for Field 3. The contour is plotted from  $3\sigma$  level and in steps of  $2\sigma$ . The red ellipses show the MDCs identified from the  $\text{H}_2$  column density map (resolution  $\sim 20''$ ) by Cao et al. (2021), and the blue ellipses illustrate the fragments extracted using the GAUSSCLUMPS algorithm. The magenta boxes show the condensations identified from the SMA 1.3 mm continuum. (b) Moment-0 map of the  $\text{NH}_3$  (2,2) line for Field 3. The contour is plotted from  $2\sigma$  level and in steps of  $2\sigma$ .

There are 148 condensations overlapping with the fields in this paper. The majority of them (103 out of 148) are distributed in the identified  $\text{NH}_3$  fragments, indicating that the  $\text{NH}_3$  fragments can probe the density structures well in most cases. As shown in Fig. 3, the (1,1) main components of most  $\text{NH}_3$  fragments have moderate optical depths, and the mean and median values are 2.2 and 1.9. Under such a moderate optical depth, the  $\text{NH}_3$  (1,1) lines might show different morphologies from the density profiles of the dust continuum emission, which could account for the condensations uncorrelated to the  $\text{NH}_3$  fragments. In conclusion, the majority of the  $\text{NH}_3$  fragments can be considered as density structures.

### 4.2. Maps of the derived physical parameters

The line-fitting process of the  $\text{NH}_3$  (1,1) and (2,2) emission lines provides the spatial distributions of the kinetic temperature, centroid velocity, velocity dispersion, optical depth of the  $\text{NH}_3$  (1,1) main component,  $\text{NH}_3$  column density, and the beam-filling fac-

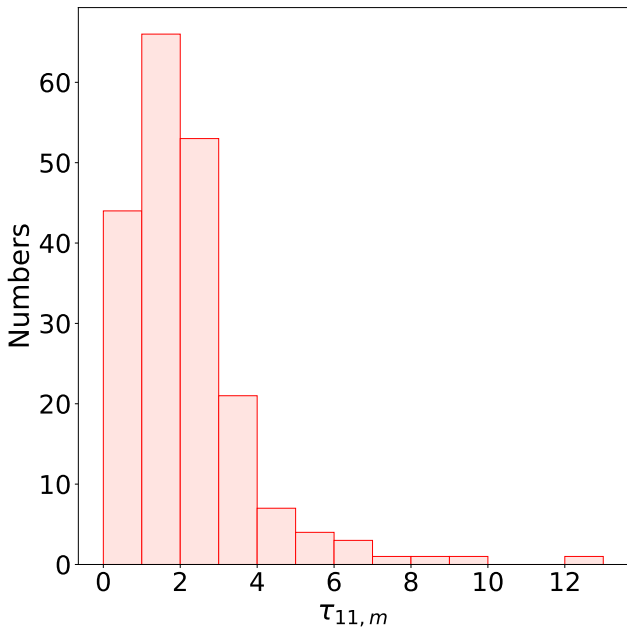


**Fig. 3.** Histogram of the average optical depth of the main component of the NH<sub>3</sub> (1,1) line for identified NH<sub>3</sub> fragments.

tor in all the fields, which allow us to investigate the temperature and dynamic conditions of the MDCs in Cygnus X and their fragments. We present maps of these derived parameters in Appendix B, and the maps of Field 3 in Fig. 4 as an example. Ranges of the derived physical parameters are listed by each field in Table 4. Using these maps, we obtain the average kinetic temperature, NH<sub>3</sub> column density, velocity dispersion, and its nonthermal component for all the NH<sub>3</sub> fragments. The contribution from the velocity gradients within the NH<sub>3</sub> fragments, which is usually considered as the bulk motion, is taken into account when calculating the velocity dispersion,  $\sigma_v$ , and its nonthermal component,  $\sigma_{v,NT}$ . We also fit the velocity gradients (following the method in e.g., Goodman et al. 1993; Wu et al. 2018) and deduct them from the nonthermal velocity dispersions, which are provided as  $\sigma_{v,ng}$ . The detailed calculation can be found in Appendix E. A brief statistic analysis of these physical parameters is reported in Table 5 and the histograms of their distributions are shown in Fig. 6. The detailed physical parameters of the NH<sub>3</sub> fragments are available in our online materials at the CDS.

Statistically, the NH<sub>3</sub> fragments have a mean deconvolved radius of 0.02 pc thanks to the high spatial resolution of our observations. Recently, Zhang et al. (2019) obtained the same value for the typical radius of condensations from their PdBI 1.3 mm continuum observations. In the other two papers of CENSUS (Pan et al. 2023; Yang et al. 2023), the properties of condensations in the Cygnus X regions are explored in more detail using submillimeter continuum and spectral observations from SMA.

The temperatures of NH<sub>3</sub> fragments range from  $\sim 11.0$  K to 34.1 K, with mean and median values of 18.6 K and 17.5 K, respectively. The mean temperature of the condensations in Zhang et al. (2019), which are selected from several massive proto-cluster clumps, is 28.3 K, which is higher than the value found in the present study. Lu et al. (2014) derived a mean temperature of  $\sim 18.3$  K for NH<sub>3</sub> dense cores (with a typical size of  $\sim 0.08$  pc) in 62 high-mass star-forming regions, which is consistent with our results. Temperature is one of the commonly used indicators of the evolutionary stage of molecular structures. For example, Sánchez-Monge et al. (2013) calculated the mean tem-

peratures of the quiescent starless cores and the protostellar cores (with typical sizes of  $\sim 0.05$  pc) as 18.8 K and 28.8 K, respectively. To verify this relation in our data, we matched the NH<sub>3</sub> fragments with the condensations from Cao et al. (2021) and the IR sources from the Cygnus X Archive catalog (the *Spitzer* Cygnus X Legacy Survey, Kraemer et al. 2010). The temperature distribution of the NH<sub>3</sub> fragments coincident with the continuum condensations (70 out of 202) is shown in Fig. 5, indicating that these fragments are more likely to be density structures. These condensation-related fragments are divided into two groups: those associated and not associated with the IR sources (44 and 26 in number). The mean temperature of the former group is  $20.4 \pm 4.5$  K, slightly higher than that of the latter group of  $19.1 \pm 4.4$  K. Also, their median temperature values are 19.4 K and 17.3 K. In general, those with IR sources are considered to be more evolved than those without IR sources. We performed a two-sample Kolmogorov-Smirnov test on the temperature distribution of these two groups and the p-value is calculated as 0.18. The p-value is higher than the threshold 0.05, indicating the two groups are not distinguishable. As shown in Fig. 5, there are also considerable overlaps in temperatures between the two groups, suggesting that there is no significant difference in internal heating for the sources in the two groups. Instead, we find that the morphology of the NH<sub>3</sub> fragments is more correlated with the evolutionary stage; we discuss this topic in Sect. 5.1.

The mean values of  $\sigma_v$ ,  $\sigma_{v,NT}$  and  $\sigma_{v,ng}$  are  $0.46 \pm 0.20$  km s<sup>-1</sup>,  $0.37 \pm 0.23$  km s<sup>-1</sup>, and  $0.34 \pm 0.21$  km s<sup>-1</sup>, respectively. The typical velocity dispersion of the condensations in Zhang et al. (2019) is  $\sim 0.9$  km s<sup>-1</sup>. Considering that their temperature is also higher than that of our NH<sub>3</sub> fragments, the larger velocity dispersion could also result from them being a more evolved sample. In contrast, our results are comparable to those of quiescent starless cores ( $0.44$  km s<sup>-1</sup> for nonthermal component) in Sánchez-Monge et al. (2013). The cores in Lu et al. (2014) have a smaller typical velocity dispersion of  $\sim 0.46$  km s<sup>-1</sup>. Detailed discussions on the dynamic states of the MDCs are given in Sect. 5.3. The mean NH<sub>3</sub> column density of the NH<sub>3</sub> fragments is  $3.9 \times 10^{15}$  cm<sup>-2</sup>, of the same order of magnitude as the values found by Sánchez-Monge et al. (2013) ( $\sim 10^{15}$  cm<sup>-2</sup>) and Lu et al. (2014) ( $\sim 2.3 \times 10^{15}$  cm<sup>-2</sup>).

#### 4.3. Correlation analysis

In this section, we present analyses of the correlations between physical parameters of the NH<sub>3</sub> fragments. We find one possible correlation between the nonthermal velocity dispersion and the kinetic temperature in our results, which are presented in Fig. 7.

Figures 7 (a) and (b) show  $\sigma_{v,NT}$  and  $\sigma_{v,ng}$  versus kinetic temperature. Though the distributions show large scatters, both of them show weak positive correlations:  $\sigma_{v,NT} = 0.012 T_K^{1.13 \pm 0.17}$  with a correlation coefficient of  $r = 0.43$ , and  $\sigma_{v,ng} = 0.007 T_K^{1.28 \pm 0.17}$  with  $r = 0.47$ . Similar correlations have been reported in previous NH<sub>3</sub> and H<sub>2</sub>CO observations, such as  $T_K \propto \Delta v^{0.53 \pm 0.14}$  in Wu et al. (2006),  $T_{\text{rot}} \propto \Delta v^{0.65}$  in Sánchez-Monge et al. (2013),  $\Delta v \propto T_{\text{rot}}^{1.16 \pm 0.29}$  in Lu et al. (2014), and  $T_K \propto \sigma_{v,NT}^{1.01 \pm 0.25}$  in Tang et al. (2018). This relation is interpreted by Wu et al. (2006) and Tang et al. (2018) as the turbulent heating effect, which converts the turbulent energy into the internal energy of gas (Guesten et al. 1985). In particular, Tang et al. (2018) obtain a positive correlation between temperature and nonthermal velocity dispersion with the APEX H<sub>2</sub>CO observations. Using the equations of turbulent temperature from Ao et al. (2013), Tang et al. (2018) suggest that the turbulent heating could play

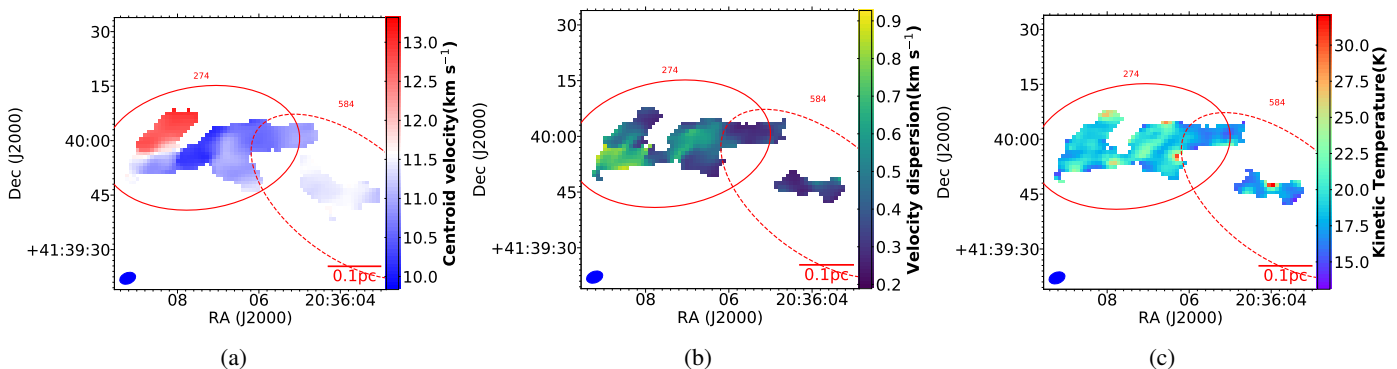


**Fig. 4.** Physical parameter maps of Field 3. (a) Centroid velocity map. (b) Velocity dispersion map. (c) Kinetic temperature map. The ellipses are the same as those in Fig. 2

**Table 4.** Ranges of derived physical properties in each field

Field	$v_{peak}$ ( $\text{km s}^{-1}$ )	$\sigma_v$ ( $\text{km s}^{-1}$ )	$T_K$ (K)	$\tau_{11,m}$	$N(\text{NH}_3)$ ( $10^{15} \text{ cm}^{-2}$ )	$\sigma_{v,NT}^a$ ( $\text{km s}^{-1}$ )
1	13.61–15.15	0.26–1.05	14.72–62.22	0.16–4.81	0.95–17.52	0.06–0.98
2	-5.54–3.87	0.26–1.01	13.84–29.30	0.22–6.44	1.05–9.81	0.12–0.95
3	10.11–13.19	0.25–0.87	14.00–35.04	0.17–5.37	0.47–14.50	0.01–0.83
4	-4.00–1.02	0.23–1.48	13.11–38.01	0.11–7.16	0.38–12.57	0.05–1.44
5	13.97–16.96	0.26–1.85	11.63–66.97	0.05–7.03	0.33–53.44	0.11–1.80
6	-3.71–0.33	0.66–1.82	18.28–32.81	0.03–66.72	0.63–18.62	0.59–1.80
7	-3.12–1.70	0.20–0.94	10.94–24.27	0.11–13.58	0.34–9.83	0.01–0.91
8	17.34–20.36	0.25–1.36	12.53–30.12	0.10–6.01	0.40–15.49	0.10–1.33
9	-3.03–2.42	0.23–0.59	13.97–31.05	0.15–4.06	0.40–7.22	0.03–0.54
10	-7.48–5.46	0.22–0.84	12.58–36.26	0.13–4.53	0.34–6.29	0.02–0.78
11	-6.97–5.16	0.22–1.53	13.38–39.98	0.13–4.77	0.30–10.81	0.02–1.49
12	-6.06–3.70	0.23–0.56	11.96–28.93	0.10–5.46	0.25–8.51	0.03–0.50
13	-0.60–1.88	0.23–0.74	13.22–45.89	0.10–9.63	0.35–10.20	0.02–0.64
14	6.75–8.59	0.23–0.72	13.30–31.18	0.14–4.45	0.36–5.50	0.01–0.68
16	5.52–6.43	0.26–1.39	13.46–22.84	0.15–4.61	0.55–11.62	0.11–1.36
17	0.31–3.11	0.21–1.39	11.85–87.87	0.03–30.02	0.35–29.15	0.01–1.29
18	-1.28–0.59	0.21–0.80	12.51–30.34	0.12–4.33	0.28–10.43	0.02–0.77
19	-2.52–0.15	0.21–0.61	11.54–27.32	0.18–33.36	0.30–21.23	0.01–0.56
20	-3.22–0.81	0.27–0.83	15.99–53.48	0.14–5.11	0.44–11.40	0.02–0.79
21 <sup>b</sup>	-7.03–4.59	0.41–1.37	16.21–127.96 <sup>c</sup>	0.14–2.70	0.74–79.52	0.31–1.30
22	4.70–7.14	0.23–1.00	11.56–18.29	0.24–5.72	0.57–9.71	0.02–0.98
23	3.88–8.07	0.24–1.18	11.12–41.60	0.14–18.47	0.42–39.98	0.01–1.14
24	-1.43–1.12	0.25–0.82	14.48–28.72	0.10–3.01	0.44–8.91	0.10–0.78
25	-0.19–2.90	0.20–0.59	9.87–19.20	0.21–83.00	0.75–69.41	0.01–0.56
26	-0.57–1.99	0.22–0.52	9.87–27.98	0.17–7.70	0.38–7.72	0.01–0.45
27	4.68–4.99	0.30–0.50	21.34–53.26	0.12–2.12	0.45–6.85	0.05–0.41
28	-1.97–0.65	0.22–0.70	12.60–34.68	0.19–10.97	0.47–16.27	0.03–0.64
29	-3.55–0.15	0.24–0.84	9.99–25.74	0.27–5.64	0.50–12.22	0.12–0.80
31	7.96–9.13	0.22–0.58	12.91–40.77	0.12–4.65	0.31–6.13	0.03–0.47
32	-12.30–10.53	0.23–0.75	11.59–21.83	0.14–8.34	0.51–8.90	0.05–0.71
33	-10.52–8.97	0.24–0.47	14.24–24.56	0.18–4.36	0.52–4.89	0.08–0.38
34	-5.39–2.19	0.26–1.30	14.70–57.77	0.08–3.04	0.31–11.74	0.07–1.27
37 <sup>d</sup>	6.54–10.29	0.24–1.90	11.47–127.96 <sup>c</sup>	0.04–36.71	0.95–8.00	0.09–1.79

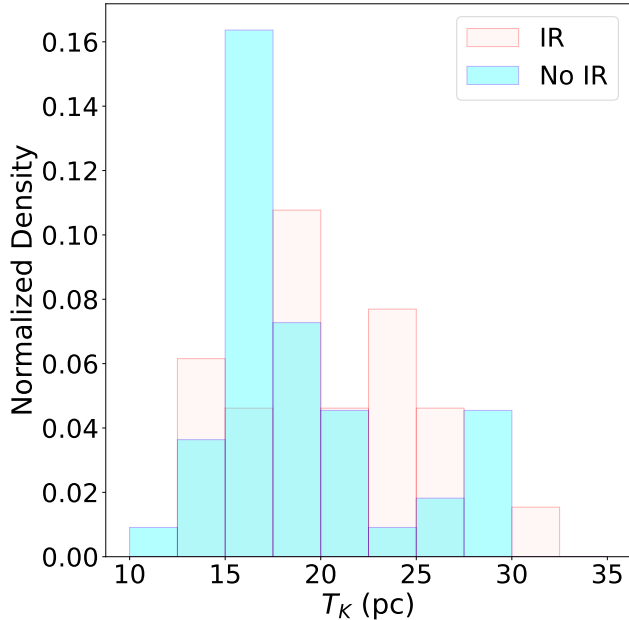
**Notes.** <sup>(a)</sup> The nonthermal velocity dispersion <sup>(b)</sup> Also known as AFGL 2591 <sup>(c)</sup> Derived from the upper limit of  $T_{\text{rot}}$ , 50 K. <sup>(d)</sup> Field 37 is fitted with two velocity components

an important role in widely existing massive star formation regions on scales of  $\sim 0.06$ –2 pc. However, such an effect usually dominates in the central molecular zone (Ginsburg et al. 2016; Immer et al. 2016) or other regions with strong nonthermal motions, which is not the case in our sample (e.g.,  $\sim 0.6$ –4  $\text{km s}^{-1}$

in Tang et al. 2018, much larger than our result of  $\sim 0.4$   $\text{km s}^{-1}$ ). Using the same method as Ao et al. (2013), we find a turbulent temperature of only  $\sim 8$  K, which is comparable to the background temperature ( $\sim 10$  K) of cold molecular gas. Therefore, the turbulent heating does not seem to be remarkable in our

**Table 5.** Statistics of physical parameters of NH<sub>3</sub> fragments

	$R$ pc	$\sigma_v$ km s <sup>-1</sup>	$\sigma_{v,NT}$ km s <sup>-1</sup>	$\sigma_{v,ng}$ km s <sup>-1</sup>	$T_K$ K	$N(\text{NH}_3)$ 10 <sup>15</sup> cm <sup>-2</sup>
Mean	0.021	0.46	0.37	0.34	18.6	3.9
Medium	0.021	0.40	0.30	0.29	17.5	3.6

**Fig. 5.** Histogram of average kinetic temperatures of the NH<sub>3</sub> fragments coinciding with the condensations of 1.3mm continuum emission. Those matched with IR sources are colored in red, while the rest are colored in cyan.

results. Lu et al. (2014) linked temperature with velocity dispersion using the black-body radiation law ( $L \sim T^4$ ), the mass-luminosity relation ( $L \sim M^\alpha$ ), and the virial equilibrium approximation ( $M \sim \sigma^2$ ), which gives an index varying from 0.67 to 2. Nevertheless, the assumptions of black-body radiation and virial equilibrium are questionable in molecular cores, and the mass-luminosity relation is very uncertain. In our results, the relation is considered as a natural consequence of the star-forming activity. An NH<sub>3</sub> fragment with stronger star-forming activity tends to be hotter and to have stronger infall and shearing motions that contribute to its nonthermal velocity dispersion. Conversely, an NH<sub>3</sub> fragment with weaker star-forming activity would be cooler and would have a smaller nonthermal velocity dispersion. This scenario is also consistent with the fact that our derived temperatures and velocity dispersions are higher at the positions of water masers and radio sources from Wang et al. (2022), where strong star-forming activities reside.

We also plot  $\sigma_{v,NT}$  and  $\sigma_{v,ng}$  versus the radius of fragments in panels (c) and (d). Such a relation is known as one of Larson's laws (Larson 1981), and is found in a number of works (e.g., Jijina et al. 1999; Wu et al. 2006; Lu et al. 2014). However, this relation is not found in our results. The main reason for the absence of these correlations could be the narrow range of the radius in our sample, which is within an order of magnitude. On the other hand, our mean value of  $\sigma_{v,ng}$  0.34 km s<sup>-1</sup> coincides with the prediction of Larson's laws of 0.32 km s<sup>-1</sup> at the scale of 0.02 pc.

## 5. Discussion

### 5.1. Morphology

#### 5.1.1. Comparison between ammonia observations and H<sub>2</sub> column density

The NH<sub>3</sub> (1,1) emissions in our data show diverse morphologies in the moment-0 maps, such as filaments (Field 28), core-like structures (Field 6), hub-like structures (Field 13), and dispersed features (Field 17). The morphology of the NH<sub>3</sub> (1,1) emission can be affected by protostellar feedback during core evolution. During the star formation process, increasing feedback from protostars can distort their envelopes (Motte et al. 2018) and heat the surrounding gas. The NH<sub>3</sub> (1,1) line gets much weaker and becomes undetectable when the gas temperature rises beyond 100 K (Ho & Townes 1983). Therefore, the morphology of the NH<sub>3</sub> in MDCs could evolve from a concentrated distribution at the peak of the H<sub>2</sub> density profile (hereafter, the M1 stage) to a dispersed shape around the protostar (hereafter, M2), and finally become undetectable (hereafter, M3). In order to construct an evolutionary sequence of the MDCs in Cygnus X, we compared the morphology of the NH<sub>3</sub> (1,1) emission to that of the H<sub>2</sub> column density (from the column density map, hereafter N-map, derived from spectral energy distribution (SED) fitting in Cao et al. 2019) of the MDCs, and classified the MDCs with infrared emissions. We present our findings in the following subsection.

As shown in Fig. 8 and Appendix C, the NH<sub>3</sub> (1,1) emission is strongly correlated with dense regions of the N-map in most fields, indicating that the NH<sub>3</sub> (1,1) line emission generally traces the dense structures in molecular gas. Nevertheless, the difference in resolution ( $\sim 3''.1$  for NH<sub>3</sub> data and  $\sim 20''$  for the N-map) leads to a more complicated morphology of NH<sub>3</sub> (1,1) emission than that of the N-map for our MDCs. We also find that many of the peaks of the NH<sub>3</sub> (1,1) emission show slight offsets from the peaks in the N-map, which could result from the depletion of NH<sub>3</sub> around protostars (Tobin et al. 2011; Sewilo et al. 2017) and from the difference in resolution between the N-map and the NH<sub>3</sub> cubes.

In light of their morphologies, we find that most (27 out of 35) MDCs are at the M1 stage. This result is consistent with our expectations, because the majority of our MDCs are not very evolved. As for the MDCs at the M2 stage (8 out of 35), we find evident star-forming activity (radio continuum emission, water masers, or bright sources on Spitzer images) in all of them, which corroborates the mentioned mechanism for distorted NH<sub>3</sub> (1,1) morphology. The MDCs at the M3 stage are not included in Table 6 because of their nondetection with the NH<sub>3</sub> (1,1) line. Figures 8 and 9 present some example MDCs in each stage.

#### 5.1.2. A possible evolutionary sequence in our sample

The evolution of MDCs is a fundamental piece in our understanding of high-mass star formation. There have been many studies focusing on this topic, both observational and theoretical (e.g., Chambers et al. 2009; Battersby et al. 2014b; Molinari et al. 2019). Based on theoretical frameworks and observations,

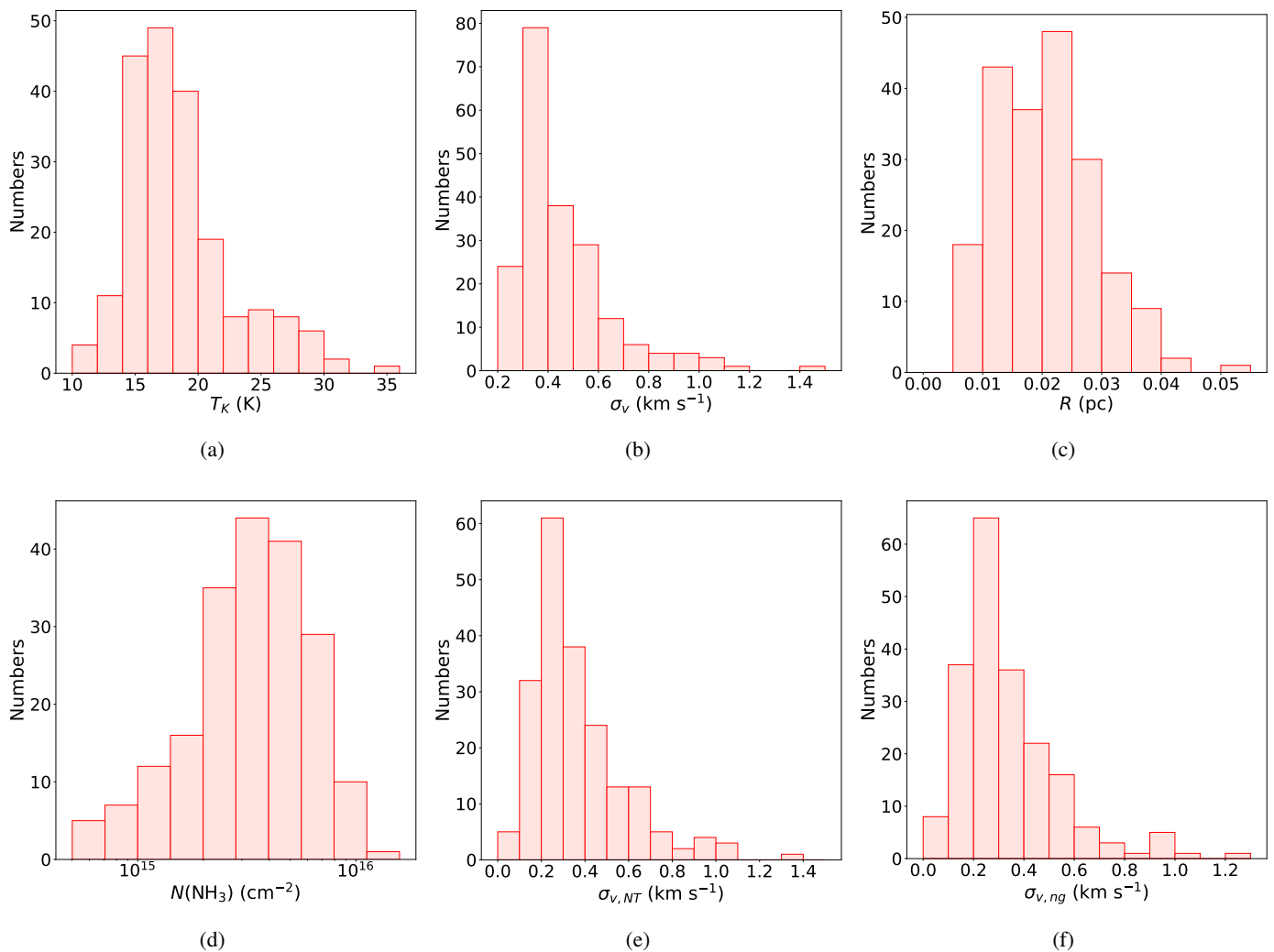


**Fig. 6.** Distributions of the physical parameters of  $\text{NH}_3$  fragments. (a) Histogram of kinetic temperatures  $T_K$ . (b) Histogram of total velocity dispersions  $\sigma_v$  (including bulk motions and using the thermal component of the entirety of the molecular gas). (c) Histogram of deconvolved radii of  $\text{NH}_3$  fragments  $R_{\text{dec}}$ . (d) Histogram of  $\text{NH}_3$  column density  $N(\text{NH}_3)$ . (e) Histogram of nonthermal velocity dispersion with bulk motions  $\sigma_{v,NT}$ . (f) Histogram of nonthermal velocity dispersion without bulk motions  $\sigma_{v,ng}$ .

a simple four-stage evolutionary scenario of MDCs is proposed as CDMC→HDMC→DAMS→FIMS by Zinnecker & Yorke (2007), where CDMC, HDMC, DAMS and FIMS stand for cold dense massive core, hot dense massive core, disk-accreting main sequence star, and final main sequence star, respectively. Recently, Motte et al. (2018) updated the star-formation pictures in different scales: (1) at the scale of 1–10 pc, the gas is fed into clumps by the inflow on ridges and hubs; (2) at the scale of  $\sim 0.1$  pc, the beginning of star-forming activity will make starless MDCs grow into protostellar MDCs; (3) the stellar embryos in high-mass protostars grow from low-mass ones into high-mass ones, which transform the high-mass protostars from IR-quiet into IR-bright at  $\sim 0.02$  pc scales; and (4) the HII region phase at 0.01–10 pc scales is the end of this scenario.

Although the evolution of high-mass protostars cannot be properly determined based on their infrared SEDs—as is possible for the low-mass ones—due to their complicated environments (Andre et al. 1993; Marseille et al. 2010), the infrared properties can still serve as an indicator of the evolution of embedded high-mass protostars. In order to obtain a better estimation of evolutionary stage, we adopt the infrared classification of

Wang et al. (2022)<sup>5</sup>. The MDCs are divided into three groups: 8 IR-bright MDCs, 25 IR-quiet MDCs, and 2 starless MDCs. The IR-bright MDCs correspond to MDCs with possible embedded high-mass protostar(s), while the IR-quiet ones only harbor low-mass protostars. Regarding the MDCs without any star-forming activity according to the criterion of Wang et al. (2022), we take them as starless MDC candidates. To illustrate the evolutionary stages of MDCs, we combine the data at hand, which include  $\text{NH}_3$  emission data, the N-map, water masers, radio continuum sources, and mid-infrared pseudo three-color maps (8, 4.5, and  $3.6 \mu\text{m}$  emission colored in red, green, and blue, respectively), into a composite image for each field (see Figures 8 and 9).

Figure 8 shows three MDCs at the M1 stage. The MDC 774 and 1179 are the only two starless MDCs in our sample. In the IR-quiet MDC 1225, we find two radio sources and two water

<sup>5</sup> The IR-bright and quiet MDCs are classified according to their *Spitzer*  $24 \mu\text{m}$  fluxes or MSX  $21 \mu\text{m}$  fluxes when  $24 \mu\text{m}$  data are saturated. The criteria are 23 Jy for  $24 \mu\text{m}$  flux and 17 Jy for  $21 \mu\text{m}$  flux. The starless candidates are selected from IR-quiet MDCs, which are not associated with any water maser, radio source, or IR sources in 2MASS, *Spitzer*, *Herschel*, and MSX catalogs.

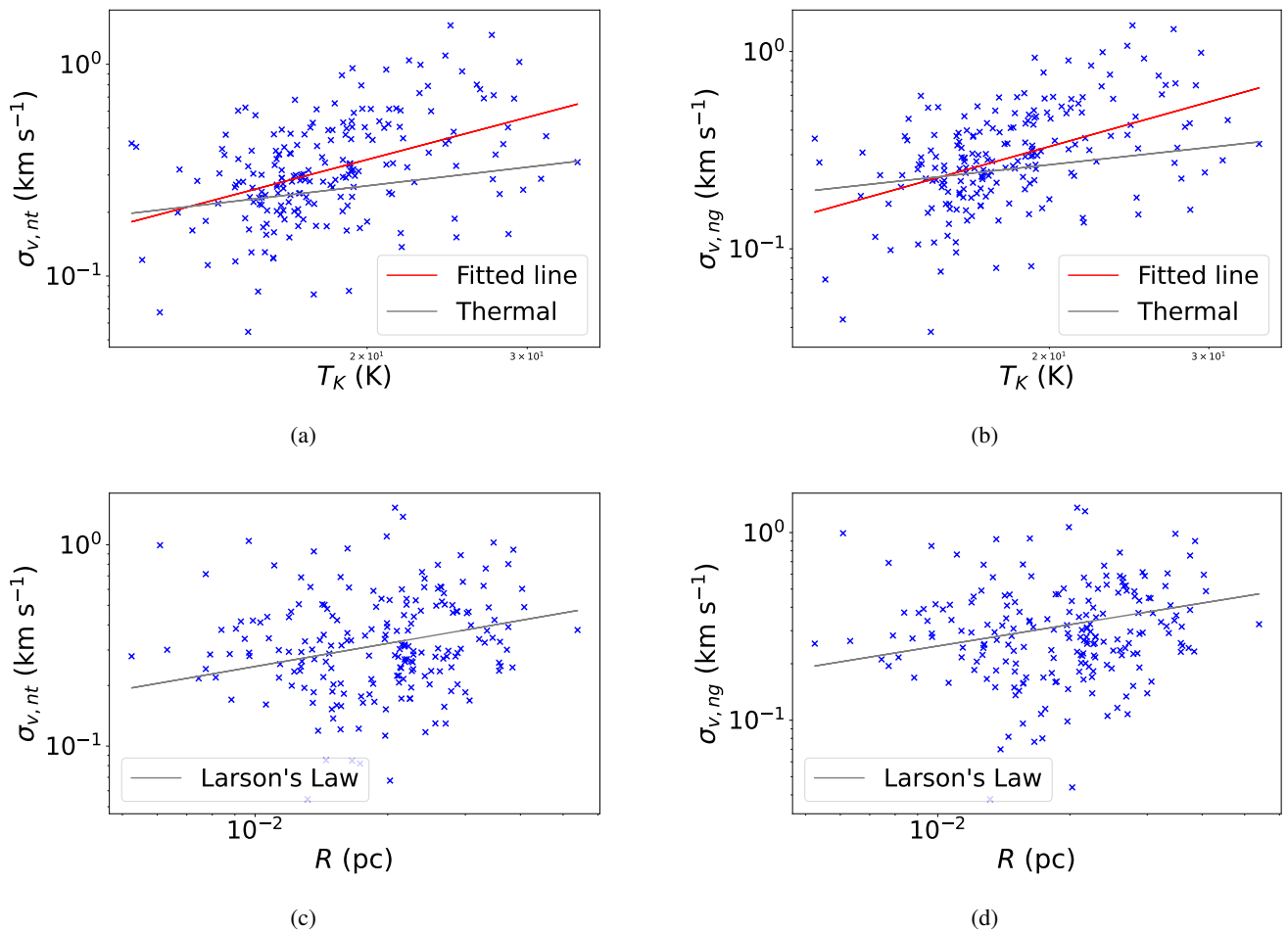


**Fig. 7.** Correlations between physical parameters of NH<sub>3</sub> fragments. Panels (a) and (b) plot nonthermal velocity dispersions including or excluding the bulk motions versus kinetic temperature. The red and gray lines show the fitted result of the linear regression and the thermal velocity dispersion. There are positive correlations in both of them. Panels (c) and (d) plot nonthermal velocity dispersions including or excluding the bulk motions versus deconvolved radius. The gray line shows Larson’s law.

masers, indicating star-forming activities and the existence of protostar(s). As the protostar or protostars grow, stronger feedback distorts the morphology of NH<sub>3</sub>, which could be the situation shown in Fig. 9. The MDC 725 and 1454 are considered to be at stage M2. The MDC 725 is an IR-bright MDC with a radio source; that is, the high-mass stellar embryo or embryos have formed in it, while the MDC 1454 is an IR-quiet MDC with NH<sub>3</sub> (1,1) emission distorted near the density peak. The MDC 1201 and 675 illustrate the latest stages in our sample, where most of the NH<sub>3</sub> is destroyed and NH<sub>3</sub> (1,1) emission is almost undetected within them. The MDC 1201 and 675 are IR-bright and IR-quiet, respectively. In conclusion, the morphology of the NH<sub>3</sub> (1,1) emission could be a possible indicator for the evolutionary stage of MDCs.

## 5.2. Virial analysis

The virial parameter, which is the ratio between the kinetic energy and the gravitational energy, is an important indicator of the dynamical conditions of molecular structures, especially for those in early evolutionary stages. Typically, the turbulent core accretion model requires a virialized MDC as the birth place of the high-mass star (McKee & Tan 2002). Previous studies in which a virial analysis was carried out using different gas tracers

at different size scales found that the distribution of virial parameters varies greatly with the sizes of molecular structures (e.g., Larson 1981; Heyer et al. 2001; Chen et al. 2019). The virial parameters of molecular clouds ( $\sim 10$  pc) are mostly  $\gg 2$ , which is the critical value of an isothermal sphere in hydrostatic equilibrium embedded in a pressurized medium (Bonnor 1956; Ebert 1955; Larson 1981), while virial ( $1 \leq \alpha_{\text{vir}} \leq 2$ ) and subvirial structures ( $\alpha_{\text{vir}} < 1$ ) are found in the fragments ( $\sim 0.01$ – $1$  pc) within molecular clouds (e.g., Pillai et al. 2011; Li et al. 2013). In this section, we perform a virial analysis of MDCs and try to understand their stability.

### 5.2.1. Calculation of virial parameters

As defined in Bertoldi & McKee (1992), the virial parameter,  $\alpha_{\text{vir}}$ , is in the form of

$$\alpha_{\text{vir}} \equiv \frac{5\sigma_v^2 R}{GM}, \quad (12)$$

where  $\sigma_v$  is the velocity dispersion and  $R$  is the radius of the structure. In this work, the total velocity dispersion of the whole molecular gas,  $\sigma_v$ , is obtained from the NH<sub>3</sub> results, and the mass of MDCs is provided by Cao et al. (2021). We therefore calculate the virial parameters for MDCs that have both NH<sub>3</sub> (1,1) and

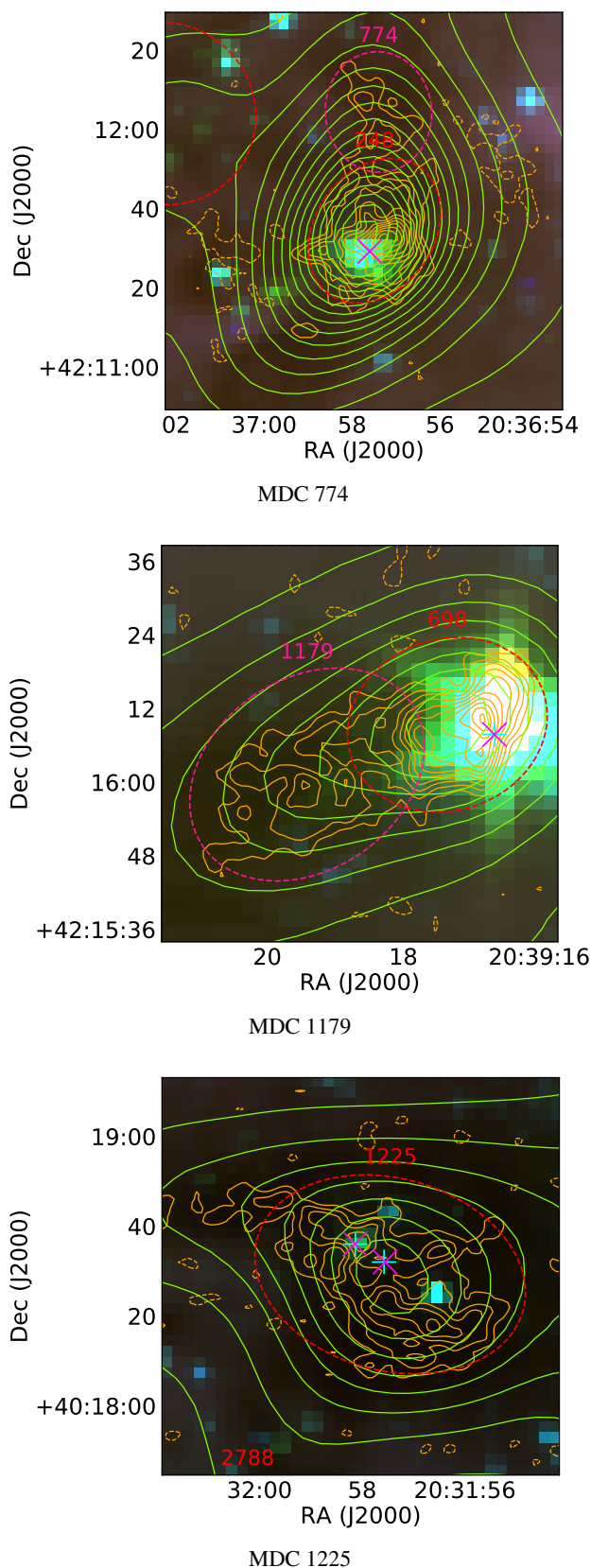


**Fig. 8.** MDCs at the M1 stage (i.e., the NH<sub>3</sub> (1,1) emission is roughly concentrated around the column density peaks). The background is pseudo three-color images of each field, with *Spitzer* 8, 4.5, and 3.6 $\mu$ m emission colored in red, green, and blue, respectively. The contours of H<sub>2</sub> column density and NH<sub>3</sub> (1,1) integrated emission are over-plotted with green and orange, respectively. Cyan and magenta crosses mark the positions of any H<sub>2</sub>O masers or radio continuum sources, respectively. The starless, IR-quiet, and IR-bright MDCs are shown as pink dashed, red dashed, and red solid ellipses, respectively. More figures are shown in Appendix C.

(2,2) detections. It is worth noting that we include the contributions from both turbulence and kinematics in the calculation of  $\sigma_v$ . Detailed calculation processes are listed in Appendix E.

In many MDCs, the detected NH<sub>3</sub> emission only covers part of the spatial extent of MDCs (such as the MDC 725 in Fig. 9). For these cases, we take the sizes of their detected parts,  $R_{\text{sel}}$ , and calculate the corresponding mass,  $M_{\text{sel}}$ , by multiplying their areas by the column densities taken from the N-map. Using  $R_{\text{sel}}$  and  $M_{\text{sel}}$ , the virial parameters are calculated for the detected parts of the MDCs, which are called “partial” virial parameters in our analysis. The partial virial parameters are considered to be an upper limit value for their host MDCs. Such overestimation comes from two aspects,  $R/M$  and  $\sigma_v$ . First, we compare  $R_{\text{sel}}/M_{\text{sel}}$  of the selected parts and  $R_{\text{total}}/M_{\text{total}}$  of their host MDCs. Figure 10 shows that all the ratios between  $R_{\text{sel}}/M_{\text{sel}}$  and  $R_{\text{total}}/M_{\text{total}}$  are larger than 1, suggesting  $R/M$  is overestimated in the partial virial parameters. Second, as shown in Appendices A and B, the velocity dispersion is usually enhanced where the integral NH<sub>3</sub> (1,1) emission is strong in most sources. The undetected parts should therefore have lower velocity dispersion than the detected parts, indicating the velocity dispersion is also overestimated in the partial virial parameters.

### 5.2.2. Distribution of virial parameters

Through the above calculations, we determined the virial parameters for 35 MDCs, including 14 full ones and 21 partial ones, as listed in Table 6. The mean and median values of the virial parameter are 1.0 and 0.9, respectively, with a standard deviation of 1.0. The majority of MDCs (23 out of 35) have a virial parameter of smaller than 1. Moreover, most full virial parameters (11 out of 14) are smaller than 1, with only one exceeding 2. Furthermore, the partial virial parameters, mostly distributed around 1, are considered as upper limits in our analysis, indicating that the majority of MDCs could be subvirialized. This result is consistent with previous findings that many MDCs are moderately to strongly subvirial (e.g., Pillai et al. 2011; Wielen et al. 2012; Li et al. 2013; Lu et al. 2014; Keown et al. 2017; Kerr et al. 2019; Traficante et al. 2020; Zhang et al. 2015; Ohashi et al. 2016; Li et al. 2020). Recently, Singh et al. (2021) proposed three possible sources of bias that could result in a false subvirial result when calculating virial parameters: neglected bulk motions, an overestimated density profile correction factor, and mass contribution from the fore- and/or background. We tried to exclude these sources of bias in our calculation: (1) The bulk motions are considered in the total kinetic energy of MDCs; (2) the density profile correction factor is taken as 1 as defined in Singh et al. (2021), which could result in an overestimated virial parameter rather than an underestimated one; and (3) the mass of our MDCs is derived from the SED fitting results of Cao et al. (2019), where the fore- and background are removed in the fitting processes. Our subvirial results should therefore not be affected by these sources of bias and we consider them to be trustworthy.

As a result, our MDCs appear to be mostly subvirialized, which is not expected based on the turbulence core accretion model (McKee & Tan 2002). This suggests that MDCs could undergo dynamical collapse in nonequilibrium in the early stages of star formation unless there is additional support. Regarding high-mass star formation, the subvirial prestellar cores, according to the simulation work by Rosen et al. (2019), are more likely to form massive stars than virialized ones due to their higher accretion rates and lower levels of fragmentation. Additionally, an anti-correlation between the virial parameter and mass has been found in many works using only a single gas tracer (e.g., Lada

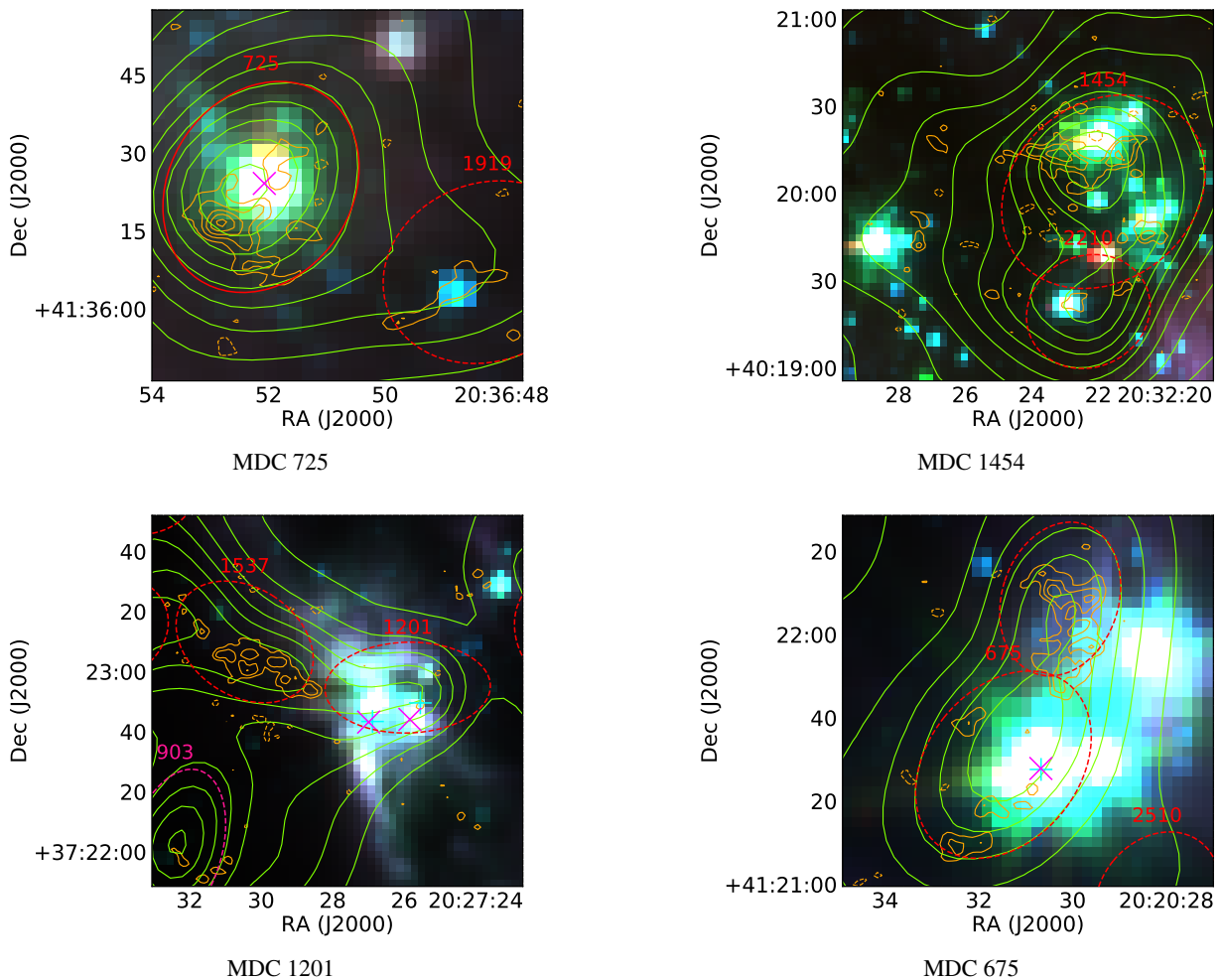


**Fig. 9.** MDCs at the M2 stage (MDC 725 and 1454) and M3 stage (MDC 1201 and 675). Marks are the same as those in Fig. 8. For MDC 1201, there is nearly no NH<sub>3</sub> (1,1) emission in it. As for MDC 675, NH<sub>3</sub> (1,1) emission is only detected in a few isolated beams around the density peak. We therefore consider both of them to be MDCs at the M3 stage.

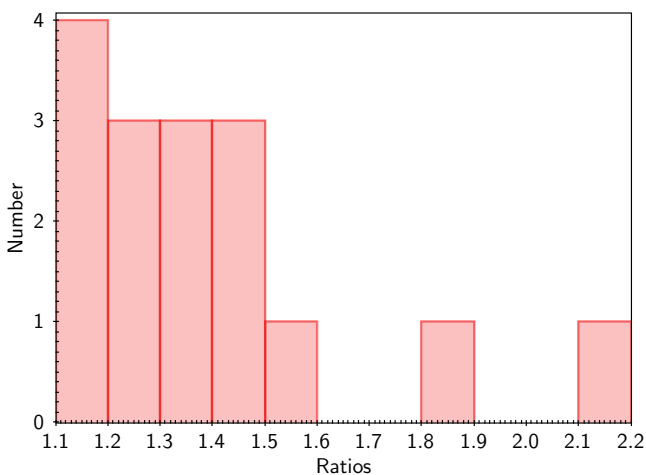


**Fig. 10.** Distribution of the ratios between  $R_{sel}/M_{sel}$  and  $R_{total}/M_{total}$

et al. 2008; Foster et al. 2009). We also plot virial parameter versus mass for our sample of MDCs in Fig. 11. However, the Pearson’s correlation coefficient of the fitted line is only 0.18, which indicates no correlation. This is mainly due to the fact that the mass range of the MDCs in our sample is very small com-

pared with other works (e.g., Roman-Duval et al. 2010; Wiene et al. 2012), namely  $\sim 10^1$ – $10^2 M_{\odot}$ . This trend also disappears in the combination of works with different gas tracers and different samples (Kauffmann et al. 2013). Traficante et al. (2018) interpret this trend as an observational bias due to the limitation of gas tracers.

As mentioned above, the subvirial MDCs would collapse if there were no additional support. Previous studies suggested that the magnetic field could provide significant support in MDCs (e.g., Frau et al. 2014; Hull & Zhang 2019; Liu et al. 2020, 2022). Following the methods in Liu et al. (2020), the total virial mass—which includes the contribution of magnetic field—can be calculated as

$$M_{k+B} = \sqrt{M_B^2 + \left(\frac{M_k}{2}\right)^2} + \frac{M_k}{2}, \quad (13)$$

where  $M_k = \alpha_{vir} M$  is the kinetic virial mass, and  $M_B$  here is

$$M_B = \frac{\pi R^2 B}{\sqrt{\frac{9}{10} \mu_0 \pi G}}. \quad (14)$$

We then calculated the total virial parameter,  $\alpha_{k+B} = M_{k+B}/M$ , by assuming a typical magnetic field strength of  $\sim 0.5$  mG (Hezareh et al. 2014). The results are shown in Fig. 12 for comparison with the original results in Fig. 11.

**Table 6.** Properties of MDCs with NH<sub>3</sub> Detection

MDC	IR-class	Morph <sup>a</sup>	NH <sub>3</sub> <sup>b</sup>	$R_{\text{sel}}^c$ (pc)	$M_{\text{sel}}^d$ (M <sub>⊙</sub> )	$\sigma_v$ (km s <sup>-1</sup> )	$\sigma_{v,\text{NT}}$ (km s <sup>-1</sup> )	$\sigma_{v,\text{ng}}$ (km s <sup>-1</sup> )	$T_{\text{dust}}^e$ (K)	$T_{\text{gas}}$ (K)	$\alpha_{\text{vir}}$	$\mathcal{M}_{\text{NT}}$	$\mathcal{M}_{\text{ng}}$	$N_{\text{H}_2}^f$ (10 <sup>22</sup> cm <sup>-2</sup> )
220	IR-quiet	M1	N	0.082	75.1	0.61	0.52	0.47	17.8	27.3	0.5	1.7	1.5	15.8
274	IR-bright	M2	N	0.122	59.4	0.97	0.93	0.76	21.3	19.0	2.2	3.6	2.9	5.7
584	IR-quiet	M1	N	0.055	7.4	0.34	0.23	0.23	20.3	17.4	1.0	0.9	0.9	3.5
725	IR-bright	M2	F	0.133	147.6	0.91	0.87	0.74	24.0	21.3	0.9	3.2	2.7	11.8
248	IR-quiet	M1	F	0.117	202.1	1.06	1.01	0.99	18.2	26.2	0.8	3.3	3.3	21.0
774	Starless	M1	F	0.098	25.0	0.53	0.46	0.45	16.4	18.9	1.3	1.8	1.7	3.7
714	IR-bright	M1	N	0.059	20.5	1.37	1.35	1.23	22.7	24.8	6.3	4.5	4.1	8.3
1267	IR-quiet	M1	F	0.155	202.5	0.44	0.37	0.31	15.3	14.7	0.2	1.6	1.4	12.0
3188	IR-quiet	M1	N	0.067	17.9	0.27	0.39	0.31	16.3	14.1	0.3	1.7	1.4	5.7
698	IR-quiet	M1	F	0.103	81.1	0.89	0.85	0.75	17.0	20.2	1.2	3.2	2.8	10.9
1179	IR-quiet	M1	F	0.123	35.9	0.78	0.73	0.55	16.0	17.5	2.4	2.9	2.2	3.4
532	IR-quiet	M2	N	0.055	10.5	0.41	0.30	0.28	23.2	21.4	1.0	1.1	1.0	4.9
801	IR-quiet	M2	N	0.117	76.3	0.55	0.48	0.45	17.8	18.4	0.5	1.9	1.7	7.9
684	IR-quiet	M1	F	0.117	109.5	0.64	0.59	0.54	17.6	19.3	0.5	2.3	2.1	11.4
327	IR-quiet	M1	N	0.097	47.1	0.35	0.26	0.25	20.9	16.4	0.3	1.1	1.0	7.1
619	Starless	M1	N	0.057	13.7	0.45	0.36	0.31	22.2	20.3	1.0	1.3	1.1	6.0
742	IR-quiet	M2	N	0.077	21.4	0.50	0.42	0.35	27.0	24.9	1.0	1.4	1.2	5.1
310	IR-quiet	M1	N	0.063	20.0	0.66	0.60	0.60	20.5	18.0	1.6	2.4	2.4	7.1
507	IR-quiet	M1	F	0.138	372.5	0.68	0.63	0.61	21.4	21.2	0.2	2.3	2.2	27.8
753	IR-quiet	M1	F	0.128	189.5	0.87	0.83	0.65	17.8	23.0	0.6	2.9	2.3	16.4
798	IR-quiet	M1	F	0.137	89.3	0.52	0.46	0.43	19.2	17.6	0.5	1.8	1.7	6.8
874	IR-quiet	M1	F	0.152	211.0	0.61	0.55	0.40	17.9	15.9	0.3	2.3	1.7	13.0
1537	IR-quiet	M1	N	0.099	44.7	0.67	0.62	0.58	25.3	23.7	1.2	2.1	2.0	6.5
723	IR-quiet	M1	N	0.087	33.9	0.66	0.62	0.57	16.0	14.5	1.3	2.7	2.5	6.4
509	IR-quiet	M2	F	0.155	300.6	0.72	0.67	0.64	18.2	18.9	0.3	2.6	2.4	17.8
351	IR-quiet	M1	N	0.081	35.0	0.69	0.64	0.49	18.3	18.2	1.3	2.5	1.9	7.6
1225	IR-quiet	M1	N	0.131	83.6	0.66	0.62	0.43	14.3	12.3	0.8	3.0	2.1	6.9
1454	IR-quiet	M2	N	0.158	142.7	0.59	0.52	0.37	16.2	17.4	0.4	2.1	1.5	8.1
892	IR-quiet	M1	N	0.038	3.9	0.37	0.18	0.18	31.6	29.6	1.5	0.6	0.5	3.9
540	IR-quiet	M1	F	0.159	240.8	0.63	0.58	0.47	15.5	16.3	0.3	2.4	1.9	13.5
302	IR-quiet	M2	N	0.08	18.1	0.48	0.39	0.35	22.3	20.3	1.2	1.5	1.3	4.0
520	IR-quiet	M1	N	0.057	8.9	0.36	0.24	0.20	23.4	18.3	1.0	0.9	0.8	3.9
340	IR-quiet	M1	F	0.139	119.3	0.57	0.52	0.47	16.1	15.0	0.4	2.3	2.0	8.8
214	IR-quiet	M1	N	0.084	53.4	0.84	0.78	0.77	21.2	27.2	1.3	2.5	2.5	10.7
247	IR-quiet	M1	N	0.092	41.3	0.56	0.46	0.41	21.3	20.1	0.8	1.7	1.5	6.9

**Notes.** <sup>(a)</sup> The morphology of NH<sub>3</sub>. MDCs at the M3 stage are not listed because of their nondetection. <sup>(b)</sup> Distribution of NH<sub>3</sub> within MDCs. “F” for NH<sub>3</sub> emission covering almost the whole spatial extent of MDCs and “N” for NH<sub>3</sub> emission only covering part of the spatial extent of MDCs. <sup>(c)</sup> The effective radii of selected regions. <sup>(d)</sup> The mass of selected regions. <sup>(e)</sup> Refer to [Cao et al. \(2021\)](#) <sup>(f)</sup> Measured from the N-map in [Cao et al. \(2019\)](#)

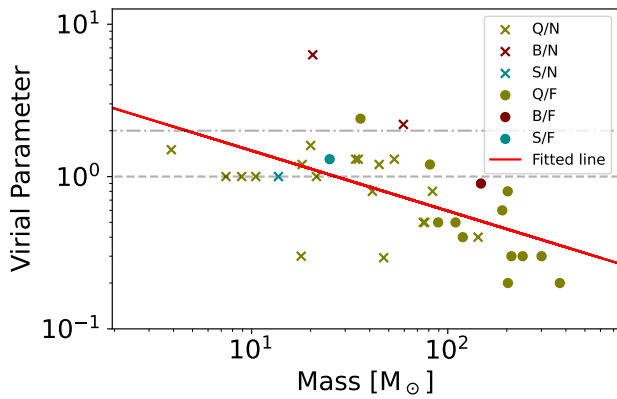


**Fig. 11.** Virial parameters vs. mass of the 35 MDCs in Cygnus X. In the legends, “B”, “Q”, and “S” refer to different infrared classes, IR-bright, IR-quiet, and starless, respectively. “F” and “N” are the same as those in Table 6. The red line shows the least-linear-square fitting result. The gray dashed lines show where virial parameters are equal to 1 and 2.

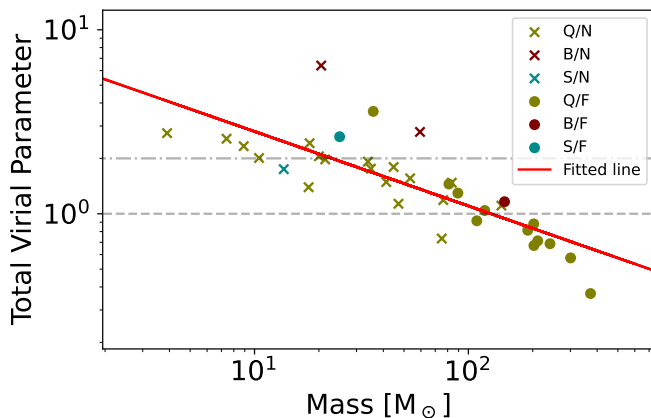


**Fig. 12.** Total virial parameter v.s. mass. The legends are the same as those in Fig. 11.

The mean and median values of the total virial parameter are 2.2 and 2.1, with a standard deviation of 1.2. The majority of total virial parameters are approximately 2 (as shown in [Kauffmann et al. 2013](#), the critical virial parameter is  $\sim 2$  for Bonnor-Ebert spheres), indicating that most MDCs are expected to be in stability with a typical magnetic field strength of 0.5 mG. In addition, if there is a strong magnetic field strength up to 1 mG, the total virial parameter would increase by  $\sim 1-2$  in value. In addition, [Liu et al. \(2022\)](#) find an anti-correlation between the magnetic virial parameter ( $\alpha_B = M_B/M$ ) and the column density of H<sub>2</sub>. Considering the typical column density of our MDCs, of namely  $\sim 10^{23} \text{ cm}^{-2}$ , the magnetic virial parameters are  $\sim 0.5$  in [Liu et al. \(2022\)](#), indicating that the magnetic field could provide remarkable support against the gravity. In our results, the nonthermal velocity dispersion of MDCs is lower than that predicted by [McKee & Tan \(2002\)](#),  $\sim 1.65(m/30M_\odot)^{1/4}\Sigma^{1/4} \text{ km s}^{-1}$ . Subsequent studies using this model ([Krumholz & McKee 2005](#), e.g.,) also proposed significant support from the magnetic field against the gravity at the scale of MDCs. The Cygnus X North and South regions are also covered by the lower resolution NH<sub>3</sub> survey (KEYSTONE) presented in [Keown et al. \(2019\)](#). The virial parameter of the NH<sub>3</sub> cores presented by these authors ( $\geq 0.1 \text{ pc}$ , referring to the NH<sub>3</sub> “leaves” in that paper) show higher

values than our results. A significant part of the NH<sub>3</sub> cores are at supervirial states in [Keown et al. \(2019\)](#). Therefore, the parent structures of our NH<sub>3</sub> fragments have larger virial parameters, indicating that the accretion of “cores” may not be dominated by the gravity. The gas might be fed to the “core” via the filament or the initial inflow suggested by [Motte et al. \(2018\)](#) and [Padoan et al. \(2020\)](#).

### 5.3. Dynamical states in star-forming regions

We produced nonthermal velocity dispersion maps of each field and mark the regions where the nonthermal velocity dispersion is higher than the sound speed with green contours (Fig. 13). We find the dynamical states vary among different MDCs. As shown in Fig. 13, the MDC 248 is dominated by the trans-sonic to supersonic nonthermal velocity dispersion ( $\mathcal{M}_{\text{NT}} \geq 1$ ), while the nonthermal velocity dispersion in MDC 892 is almost entirely subsonic. The majority of MDCs consist of both supersonic and subsonic regions, such as MDCs 274, 584, and 774. Maps of other fields are reported in Appendix D.

In Sect. 4.2, we provide the  $\sigma_{v,\text{NT}}$  and  $\sigma_{v,\text{ng}}$  of NH<sub>3</sub> fragments, where the resolved bulk motions are included and excluded, respectively. We also calculate  $\sigma_{v,\text{NT}}$  and  $\sigma_{v,\text{ng}}$  for MDCs. Then, using  $\sigma_{v,\text{NT}}$  and  $\sigma_{v,\text{ng}}$ , we obtain the Mach numbers,  $\mathcal{M}_{\text{NT}}$  and  $\mathcal{M}_{\text{ng}}$ , for both NH<sub>3</sub> fragments and MDCs (Fig. 14). For MDCs,  $\mathcal{M}_{\text{NT}}$  has mean and median values of 2.2 and 2.3, with a standard deviation of 0.8, while the mean and median values of  $\mathcal{M}_{\text{ng}}$  are 1.9 and 1.9, with a standard deviation of 0.7. As for NH<sub>3</sub> fragments, the majority of both  $\mathcal{M}_{\text{NT}}$  and  $\mathcal{M}_{\text{ng}}$  are smaller than 2 (trans-sonic to subsonic). The mean and median values of  $\mathcal{M}_{\text{NT}}$  are 1.4 and 1.2, with a standard deviation of 0.8, and the mean and median values of  $\mathcal{M}_{\text{ng}}$  are 1.3 and 1.1, with a standard deviation of 0.7. These distributions of NH<sub>3</sub> fragments are similar to previous results (e.g., [Sokolov et al. 2018](#); [Yue et al. 2021](#); [Li et al. 2020](#)) The differences between  $\mathcal{M}_{\text{NT}}$  and  $\mathcal{M}_{\text{ng}}$  of MDCs are more remarkable than those of NH<sub>3</sub> fragments, suggesting that the bulk motions have a larger contribution to the nonthermal velocity dispersions of MDCs than those of NH<sub>3</sub> fragments. In contrast, the  $\mathcal{M}_{\text{ng}}$  and  $\mathcal{M}_{\text{NT}}$  of NH<sub>3</sub> fragments are close. Moreover, both panels show a decreasing trend in Mach number from MDCs to NH<sub>3</sub> fragments.

Recently, high-spatial-resolution observations revealed similar transonic and subsonic nonthermal velocity dispersion in both low-mass and high-mass star-forming regions, such as L1517 ([Hacar & Tafalla 2011](#)), NGC 1333 ([Hacar et al. 2017](#)), the Orion integral filament ([Hacar et al. 2018](#)), OMC 2/3 ([Yue et al. 2021](#)), and NGC 6334S ([Li et al. 2020](#)). Comparing N<sub>2</sub>H<sup>+</sup>  $J=1-0$  observations from the Nobeyama 45m telescope and ALMA, [Yue et al. \(2021\)](#) propose the nonthermal motions would transit from supersonic motions to subsonic motions at a scale of  $\sim 0.05 \text{ pc}$ . In our results, the transition occurs at a scale of NH<sub>3</sub> fragments,  $\sim 0.04 \text{ pc}$ , which is consistent with the result of [Yue et al. \(2021\)](#). These latter authors interpret this transition as a resolution-dependent bias, where more bulk motions are involved in larger beams and give a greater nonthermal velocity dispersion. The large-scale dispersion measured from Nobeyama observations,  $\sigma_{\text{ls}}$ , is decomposed in [Yue et al. \(2021\)](#) into small-scale dispersion measured from ALMA observations,  $\sigma_{\text{ss}}$ , bulk motion probed by dispersion between the peak velocity of each ALMA beam,  $\sigma_{\text{bm}}$ , and residual dispersion,  $\sigma_{\text{rd}}$ , with the relation  $\sigma_{\text{ls}}^2 = \sigma_{\text{ss}}^2 + \sigma_{\text{bm}}^2 + \sigma_{\text{rd}}^2$ . Comparing  $\mathcal{M}_{\text{ng}}$  of MDCs with that of NH<sub>3</sub> fragments as shown in the panel (b) of Fig. 14, where the bulk motions are deducted, the decreasing trend of  $\mathcal{M}_{\text{ng}}$  from MDCs to NH<sub>3</sub> fragments still remains. The differences between

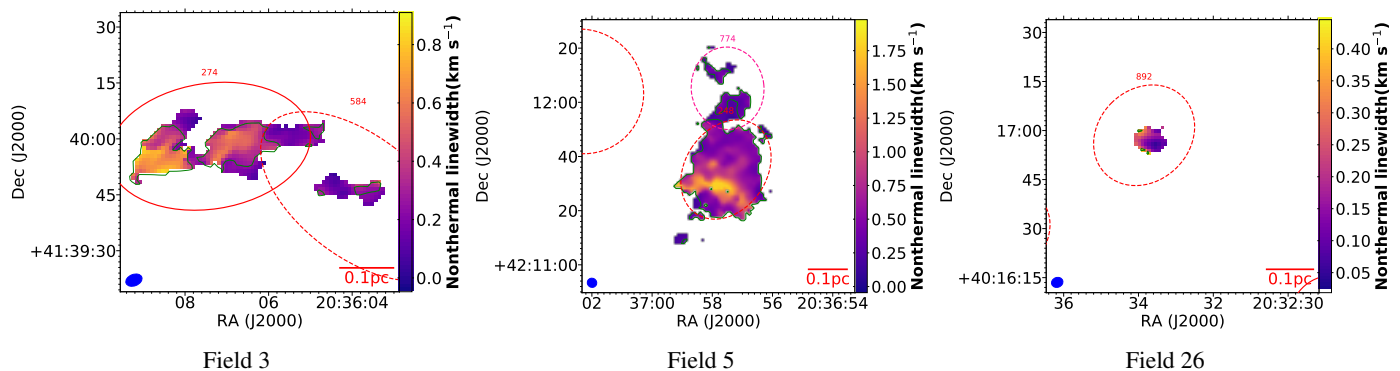


**Fig. 13.** Nonthermal velocity dispersion maps of Fields 3, 5, and 26. The green contours show the regions with Mach numbers of greater than 1. The ellipses are the same as those in Fig. 2

the  $M_{\text{ng}}$  of MDCs and that of  $\text{NH}_3$  fragments could refer to  $\sigma_{\text{rd}}$ . A possible explanation for  $\sigma_{\text{rd}}$  is turbulent vortex, as put forward by Yue et al. (2021). In most cases, the decrease in nonthermal velocity dispersion from large scale to small scale is also thought to be the dissipation of turbulence, as suggested by the relation between velocity dispersion and size at lower spatial resolutions ( $\sim 0.1 - 100$  pc) in Larson (1981). Considering that the typical size of  $\text{NH}_3$  fragments ( $\sim 0.04$  pc) is larger than the typical Kolmogorov scale in molecular clouds ( $\sim 10^{-5} - 10^{-4}$  pc) (McKee & Ostriker 2007; Kritsuk et al. 2011; Qian et al. 2018), the turbulent dissipation could be a possible cause for the decreasing trend of  $M_{\text{ng}}$ .

Furthermore, the lower Mach numbers imply that magnetic fields can play a more important role if the fragments are in a virialized state. However, as shown in Liu et al. (2022),  $\alpha_B$  would decrease with increasing column density. Considering that  $\alpha_B$  is about 0.5 in our MDCs, the gravity could be more dominant than the magnetic field in these fragments (usually the peaks on the column density map). As estimated by Sokolov et al. (2018), magnetic fields with strengths over  $\sim 1$  mG are needed to achieve virialization in these fragments. However, such a strong magnetic fields have only been detected in a small number of star-forming structures (e.g., Curran & Chrysostomou 2007; Fish & Sjouerman 2007; Palau et al. 2021). Therefore, the fragments of MDCs are probably not in virialized states.

#### 5.4. Gas and dust temperature

In general, there are two ways to trace the temperature of molecular clouds: from the dust continuum emission or from spectral line emission of a certain molecule. As the temperatures of MDCs are also provided in Cao et al. (2021) ( $T_{\text{dust}}$  column in Table 6), which were calculated from the SED fitting of the dust continuum data, we compared these temperatures with the temperatures derived from the  $\text{NH}_3$  data; we present our findings below.

In order to compare the  $\text{NH}_3$  temperature and the dust temperature in MDCs, the  $\text{NH}_3$  data cubes are convolved to the resolution of temperature map in Cao et al. (2019) and the  $\text{NH}_3$  temperatures of MDCs are rederived ( $T_{\text{gas}}$  column in Table 6). The correlation between them is plotted in Fig. 15. The gray line illustrates where  $T_{\text{gas}} = T_{\text{dust}}$  and the red line presents the linear regression fitting result,

$$T_{\text{dust}} = 0.60T_{\text{gas}} + 7.82, \quad (15)$$

with the correlation coefficient  $r = 0.66$ . According to this relation, the gas temperature is mostly higher than the dust temperature when  $T_{\text{gas}} \geq 20$  K. In the scatter plot, the turning point is also around 20 K. We find that  $T_{\text{dust}}$  is almost equal to  $T_{\text{gas}}$  when  $T_{\text{gas}} \leq 20$  K and deviates from  $T_{\text{gas}}$  when  $T_{\text{gas}} \geq 20$  K.

The gas and dust are expected to be well coupled—that is, they can be characterized by the same temperature—within a molecular core with a density of  $\geq 10^{4.5} \text{ cm}^{-3}$  (Goldsmith 2001; Young et al. 2004). This coupling has been confirmed by many works (e.g., Dunham et al. 2010; Merello et al. 2019). However, although all the MDCs in our sample have densities higher than  $10^5 \text{ cm}^{-3}$ ,  $T_{\text{gas}}$  and  $T_{\text{dust}}$  are not thermally well coupled. Similarly, in high-mass star-forming regions,  $T_{\text{gas}}$  is usually measured to be higher than  $T_{\text{dust}}$ , which is the case for example for the quiescent clumps in Battersby et al. (2014a), the S 140 in Koumpia et al. (2015), and the W40 in Tursun et al. (2020).

The origin of the excess gas temperature is a complex open question. In the photon-dominated region S 140, Koumpia et al. (2015) found an excess of  $\sim 5$ -15 K in their deeply embedded regions, where  $T_{\text{dust}}$  and  $T_{\text{gas}}$  are expected to be well coupled in the KOSMA- $\tau$  PDR model (Röllig et al. 2013). Koumpia et al. (2015) interpret these differences as the result of inhomogeneous clumpy structures, which could lead to a deeper penetration of the UV radiation and heating of the gas in the embedded cores. In addition, differences between  $T_{\text{gas}}$  and  $T_{\text{dust}}$  can also arise from different layers traced by the gas and the dust (Battersby et al. 2014a). Such differences arise from both different excitation conditions and different angular resolutions. The  $\text{NH}_3$  (1,1) and (2,2) lines are usually excited in the dense gas, while the dust continuum emission arises from a range of densities. In the present work, the resolutions of the  $\text{NH}_3$  data and the temperature map from Cao et al. (2019) are quite different. Only a few MDCs have sufficient temperature pixels as shown in Fig. 4 and Appendix B. The spatially extended  $\text{NH}_3$  emission, which usually has lower temperatures, is missed due to the filtering effect of VLA. In our results,  $T_{\text{gas}}$  deviates from  $T_{\text{dust}}$  at  $T_{\text{gas}} \geq 20$  K (Fig. 15). The MDCs with  $T_{\text{gas}} \geq 20$  K should have internal heating from the star-forming activity, but this heating is diluted by the large beam in the dust temperature data. Therefore, on average, we obtain a higher  $T_{\text{gas}}$  than  $T_{\text{dust}}$  in our results.

## 6. Summary

The initial conditions of the birth places of high-mass stars are of utmost importance in the study of high-mass star formation. We present VLA  $\text{NH}_3$  (1,1) and (2,2) observations of MDCs in

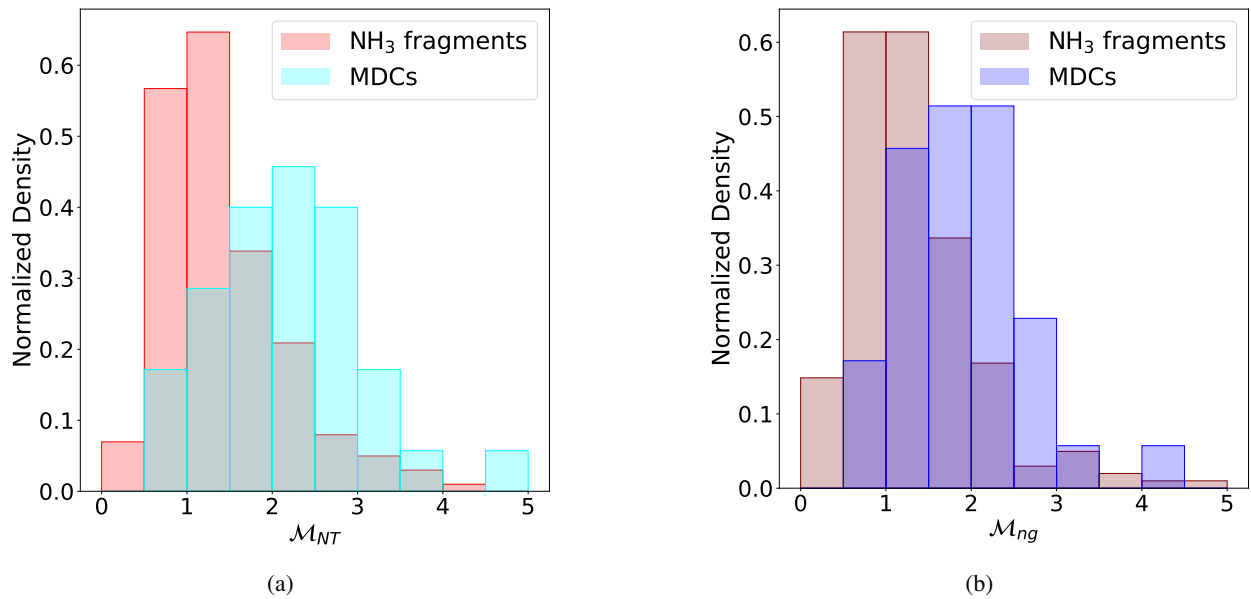


**Fig. 14.** Normalized density distribution of  $M_{NT}$  and  $M_{ng}$  in NH<sub>3</sub> fragments and MDCs. The contribution of velocity gradient is included in (a) and excluded in (b)

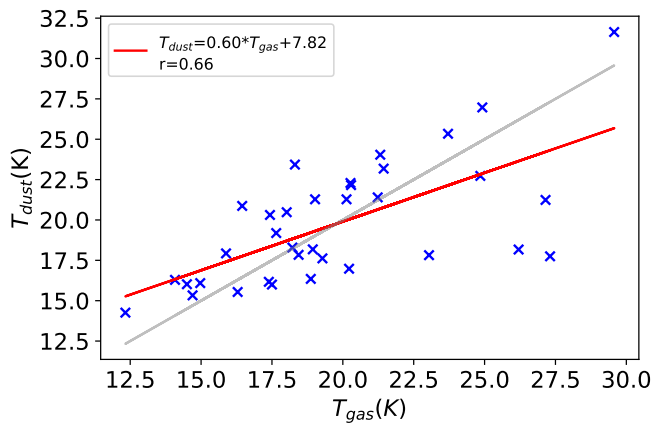


**Fig. 15.** Correlation between  $T_{gas}$  and  $T_{dust}$ . The red line shows the linear regression fitting results, and the gray line shows where  $T_{dust} = T_{gas}$ .

Cygnus X at a distance of 1.4 kpc. As a part of the CENSUS project, we provide the temperature and dynamical information derived from the simultaneous line fitting of the NH<sub>3</sub> (1,1) and (2,2) inversion emission lines.

We used the MDCs catalog from Cao et al. (2021) in our analysis. We compared the morphology between the H<sub>2</sub> column density map from Cao et al. (2019) and NH<sub>3</sub> (1,1) emission within each MDC and provide a possible indicator for estimating their evolutionary stages. We also performed a virial analysis for each MDC to evaluate the stability of the MDCs. The dynamical states of the MDCs are discussed based on their non-thermal velocity dispersions. We also compare the gas temperature with the dust temperature of MDCs. In addition, we identified 202 fragments from the NH<sub>3</sub> (1,1) moment-0 maps using the GAUSSCLUMPS algorithm. We derived the physical parameters of these NH<sub>3</sub> fragments and conducted a correlation analysis among them. We also analyzed the dynamical states of the NH<sub>3</sub> fragments and compared them with those of the MDCs. The main results of this paper can be summarized as follows:

1. The NH<sub>3</sub> fragments have a mean deconvolved radius of 0.02 pc, a mean velocity dispersion of 0.46 km s<sup>-1</sup>, a mean non-thermal velocity dispersion of 0.37 km s<sup>-1</sup>, a mean kinetic temperature of 18.6 K, and a mean NH<sub>3</sub> column density of  $3.9 \times 10^{15}$  cm<sup>-2</sup>. Comparison with the temperature of structures in previous works indicates that the NH<sub>3</sub> fragments are mostly early evolved structures.
2. We find a correlation between nonthermal velocity dispersion and kinetic temperature. This correlation is likely the result of different levels of star-forming activity. A molecular structure with more active star-forming activity is usually hotter and with larger velocity dispersion.
3. We perform a morphological analysis of the NH<sub>3</sub> (1,1) emission and column density map of MDCs. We propose a possible evolutionary sequence of MDCs based on the NH<sub>3</sub> (1,1) emission: in the early, relatively little-evolved MDCs, the NH<sub>3</sub> emission is concentrated around density peaks; the NH<sub>3</sub> emission is subsequently dispersed by the star-forming activity, after which, in the evolved MDC, the NH<sub>3</sub> emission becomes undetected.
4. We perform a virial analysis of all MDCs. The majority of the MDCs of our sample are subvirialized, indicating that the kinetic energy cannot support the MDCs alone in our sample. Considering the support from magnetic fields, MDCs could attain their stability states if there were a typical magnetic field strength of  $\sim 0.5$  mG.
5. We investigate the dynamic states of MDCs and the NH<sub>3</sub> fragments with their nonthermal Mach numbers. The Mach numbers show a decreasing trend from MDCs to NH<sub>3</sub> fragments, which could be an indication of the dissipation of turbulence. When the resolved bulk motions are excluded from the nonthermal velocity dispersion, we find the NH<sub>3</sub> fragments are mostly subsonic to trans-sonic, while the majority of MDCs are transonic.
6. The gas temperature derived from NH<sub>3</sub> (1,1) and (2,2) lines is compared with the dust temperature calculated by SED fitting from Cao et al. (2019). The two are well coupled when the gas temperature is  $\lesssim 20$  K, while the gas temperature is

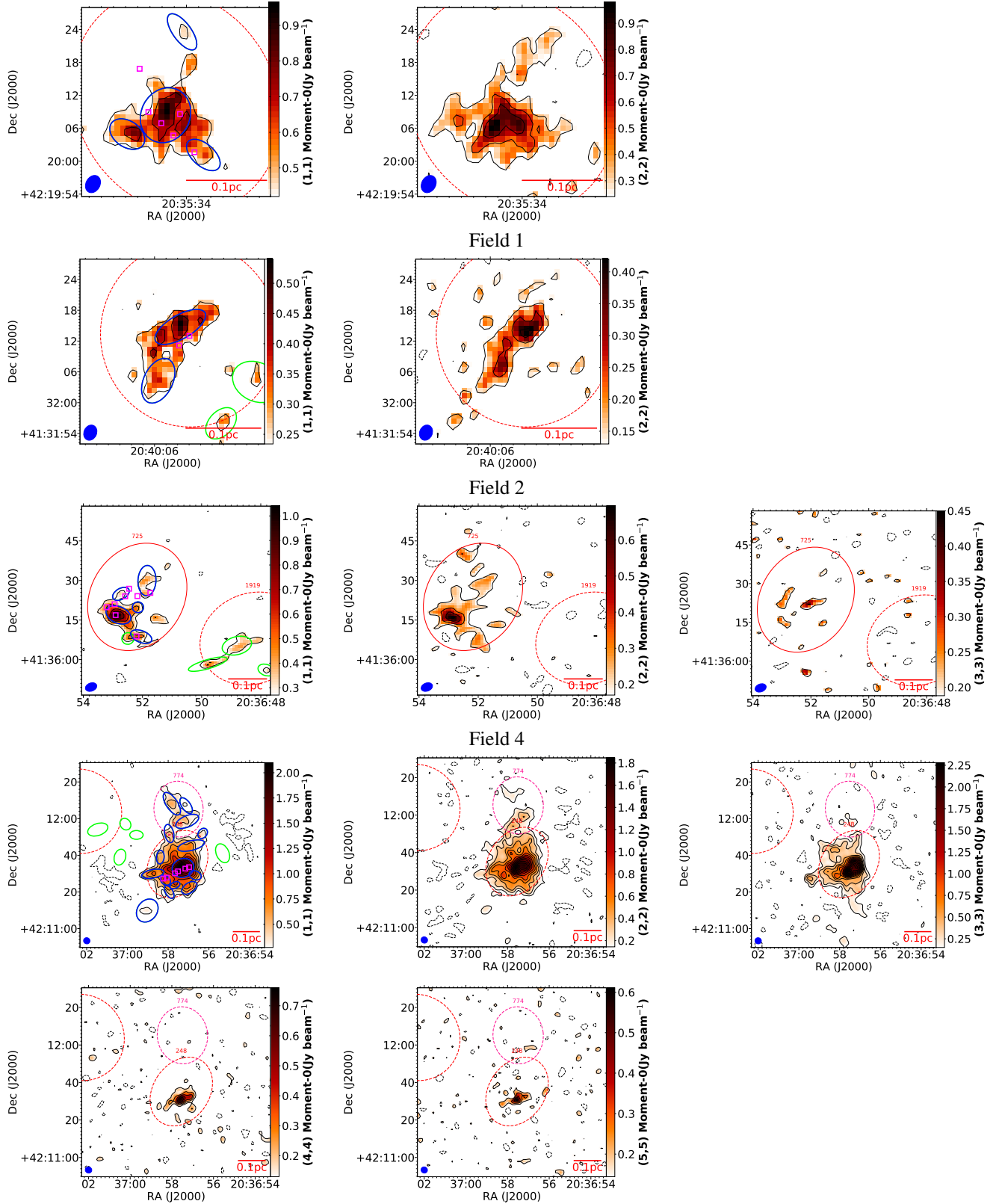
mostly larger than the dust temperature when the gas temperature is  $\geq 20$  K.

**Acknowledgements.** This work is supported by National Key R&D Program of China No. 2022YFA1603103, No. 2017YFA0402604, the National Natural Science Foundation of China (NSFC) grant U1731237, and the science research grant from the China Manned Space Project with No. CMS-CSST-2021-B06. This research made use of *APLpy*, an open-source plotting package for Python. (Robitaille & Bressert 2012) This research made use of *Astropy*, a community-developed core Python package for Astronomy. (Astropy Collaboration et al. 2013, 2018) This study used observations from the Spitzer Space Telescope Cygnus X Legacy Survey (PID 40184, P.I. Joseph L. Hora).

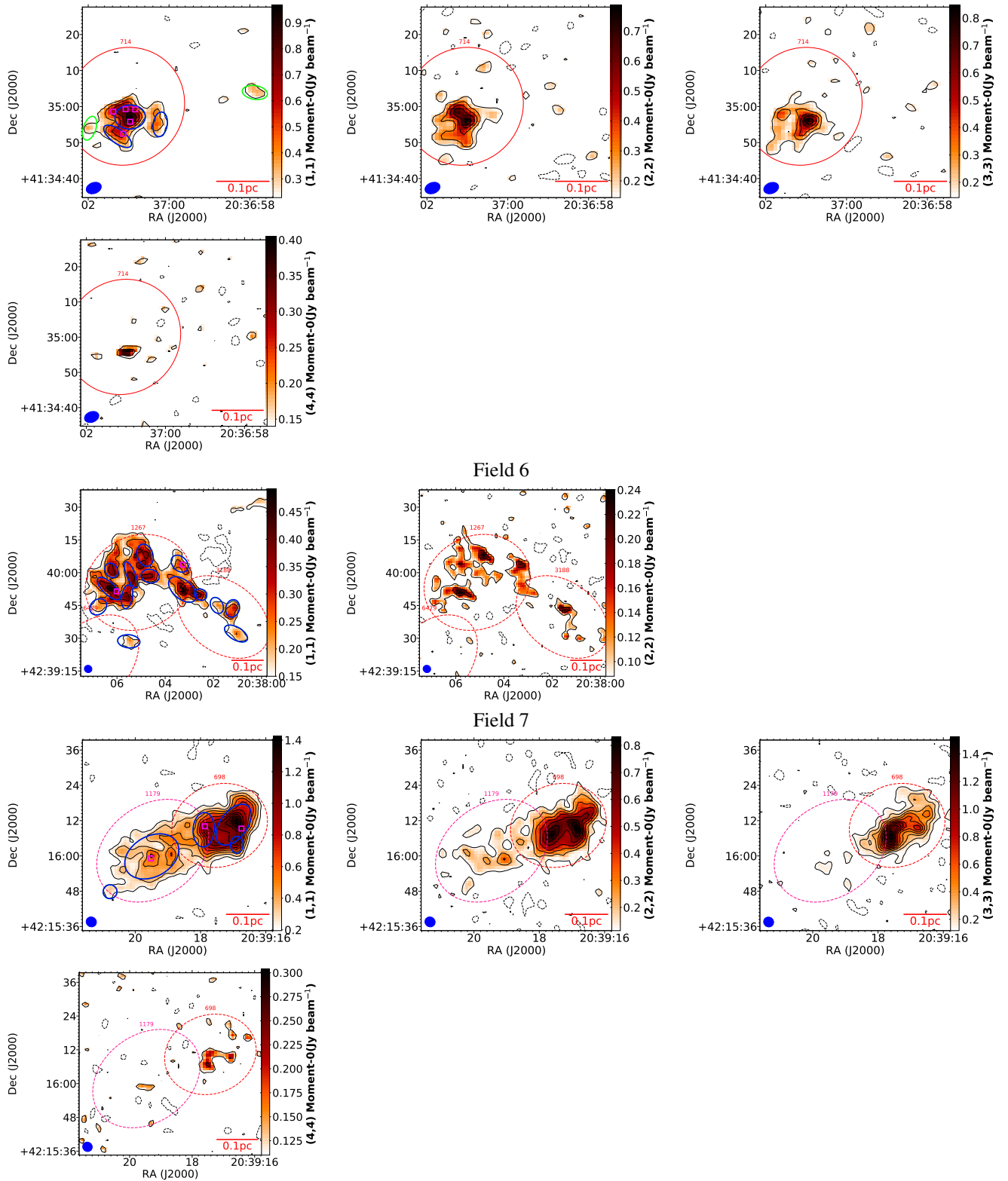
## References

- Andre, P., Ward-Thompson, D., & Barsony, M. 1993, *ApJ*, **406**, 122
- Ao, Y., Henkel, C., Menten, K. M., et al. 2013, *A&A*, **550**, A135
- Astropy Collaboration, Price-Whelan, A. M., Sipőcz, B. M., et al. 2018, *AJ*, **156**, 123
- Astropy Collaboration, Robitaille, T. P., Tollerud, E. J., et al. 2013, *A&A*, **558**, A33
- Barranco, J. A. & Goodman, A. A. 1998, *ApJ*, **504**, 207
- Battersby, C., Bally, J., Dunham, M., et al. 2014a, *ApJ*, **786**, 116
- Battersby, C., Ginsburg, A., Bally, J., et al. 2014b, *ApJ*, **787**, 113
- Berry, D. S., Reinhold, K., Jenness, T., & Economou, F. 2007, in *Astronomical Society of the Pacific Conference Series*, Vol. 376, *Astronomical Data Analysis Software and Systems XVI*, ed. R. A. Shaw, F. Hill, & D. J. Bell, **425**
- Bertoldi, F. & McKee, C. F. 1992, *ApJ*, **395**, 140
- Beuther, H., Schilke, P., Menten, K. M., et al. 2002, *ApJ*, **566**, 945
- Billington, S. J., Urquhart, J. S., Figura, C., Eden, D. J., & Moore, T. J. T. 2019, *MNRAS*, **483**, 3146
- Bonnell, I. A., Bate, M. R., Clarke, C. J., & Pringle, J. E. 1997, *MNRAS*, **285**, 201
- Bonnell, I. A., Bate, M. R., Clarke, C. J., & Pringle, J. E. 2001, *MNRAS*, **323**, 785
- Bonnell, I. A., Bate, M. R., & Zinnecker, H. 1998, *MNRAS*, **298**, 93
- Bonnor, W. B. 1956, *MNRAS*, **116**, 351
- Cao, Y., Qiu, K., Zhang, Q., et al. 2019, *ApJS*, **241**, 1
- Cao, Y., Qiu, K., Zhang, Q., Wang, Y., & Xiao, Y. 2021, *ApJ*, **918**, L4
- Chambers, E. T., Jackson, J. M., Rathborne, J. M., & Simon, R. 2009, *ApJS*, **181**, 360
- Chen, H.-R. V., Zhang, Q., Wright, M. C. H., et al. 2019, *ApJ*, **875**, 24
- Chira, R. A., Beuther, H., Linz, H., et al. 2013, *A&A*, **552**, A40
- Curran, R. L. & Chrysostomou, A. 2007, *MNRAS*, **382**, 699
- Currie, M. J., Berry, D. S., Jenness, T., et al. 2014, in *Astronomical Society of the Pacific Conference Series*, Vol. 485, *Astronomical Data Analysis Software and Systems XXIII*, ed. N. Manset & P. Forshay, **391**
- Dunham, M. K., Rosolowsky, E., Evans, Neal J., I., et al. 2010, *ApJ*, **717**, 1157
- Ebert, R. 1955, *ZAp*, **37**, 217
- Fish, V. L. & Sjouerman, L. O. 2007, *ApJ*, **668**, 331
- Foster, J. B., Rosolowsky, E. W., Kauffmann, J., et al. 2009, *ApJ*, **696**, 298
- Frau, P., Girart, J. M., Zhang, Q., & Rao, R. 2014, *A&A*, **567**, A116
- Ginsburg, A., Henkel, C., Ao, Y., et al. 2016, *A&A*, **586**, A50
- Goldsmith, P. F. 2001, *ApJ*, **557**, 736
- Goodman, A. A., Benson, P. J., Fuller, G. A., & Myers, P. C. 1993, *ApJ*, **406**, 528
- Gottschalk, M., Kothes, R., Matthews, H. E., Landecker, T. L., & Dent, W. R. F. 2012, *A&A*, **541**, A79
- Guesten, R., Walmsley, C. M., Ungerechts, H., & Churchwell, E. 1985, *A&A*, **142**, 381
- Hacar, A. & Tafalla, M. 2011, *A&A*, **533**, A34
- Hacar, A., Tafalla, M., & Alves, J. 2017, *A&A*, **606**, A123
- Hacar, A., Tafalla, M., Forbrich, J., et al. 2018, *A&A*, **610**, A77
- Heyer, M. H., Carpenter, J. M., & Snell, R. L. 2001, *ApJ*, **551**, 852
- Hezareh, T., Csengeri, T., Houde, M., Herpin, F., & Bontemps, S. 2014, *MNRAS*, **438**, 663
- Ho, P. T. P. & Townes, C. H. 1983, *ARA&A*, **21**, 239
- Hull, C. L. H. & Zhang, Q. 2019, *Frontiers in Astronomy and Space Sciences*, **6**, 3
- Immer, K., Kauffmann, J., Pillai, T., Ginsburg, A., & Menten, K. M. 2016, *A&A*, **595**, A94
- Jijina, J., Myers, P. C., & Adams, F. C. 1999, *ApJS*, **125**, 161
- Kauffmann, J., Bertoldi, F., Bourke, T. L., Evans, N. J., I., & Lee, C. W. 2008, *A&A*, **487**, 993
- Kauffmann, J., Pillai, T., & Goldsmith, P. F. 2013, *ApJ*, **779**, 185
- Keown, J., Di Francesco, J., Kirk, H., et al. 2017, *ApJ*, **850**, 3
- Keown, J., Di Francesco, J., Rosolowsky, E., et al. 2019, *ApJ*, **884**, 4
- Kerr, R., Kirk, H., Di Francesco, J., et al. 2019, *ApJ*, **874**, 147
- Koumpia, E., Harvey, P. M., Ossenkopf, V., et al. 2015, *A&A*, **580**, A68
- Kraemer, K. E., Hora, J. L., Adams, J., et al. 2010, in *American Astronomical Society Meeting Abstracts*, Vol. 215, *American Astronomical Society Meeting Abstracts #215*, **414.01**
- Kritsuk, A. G., Nordlund, Å., Collins, D., et al. 2011, *ApJ*, **737**, 13
- Krumholz, M. R. 2015, *arXiv e-prints*, [arXiv:1511.03457](https://arxiv.org/abs/1511.03457)
- Krumholz, M. R. & McKee, C. F. 2005, *ApJ*, **630**, 250
- Lada, C. J., Muench, A. A., Rathborne, J., Alves, J. F., & Lombardi, M. 2008, *ApJ*, **672**, 410
- Larson, R. B. 1981, *MNRAS*, **194**, 809
- Leung, H. O. & Thaddeus, P. 1992, *ApJS*, **81**, 267
- Li, D., Goldsmith, P. F., & Menten, K. 2003, *ApJ*, **587**, 262
- Li, D., Kauffmann, J., Zhang, Q., & Chen, W. 2013, *ApJ*, **768**, L5
- Li, S., Zhang, Q., Liu, H. B., et al. 2020, *ApJ*, **896**, 110
- Liu, J., Qiu, K., & Zhang, Q. 2022, *ApJ*, **925**, 30
- Liu, J., Zhang, Q., Qiu, K., et al. 2020, *ApJ*, **895**, 142
- Lu, X., Zhang, Q., Liu, H. B., Wang, J., & Gu, Q. 2014, *ApJ*, **790**, 84
- Mangum, J. G. & Shirley, Y. L. 2015, *PASP*, **127**, 266
- Marseille, M. G., van der Tak, F. F. S., Herpin, F., & Jacq, T. 2010, *A&A*, **522**, A40
- McKee, C. F. & Ostriker, E. C. 2007, *ARA&A*, **45**, 565
- McKee, C. F. & Tan, J. C. 2002, *Nature*, **416**, 59
- McKee, C. F. & Tan, J. C. 2003, *ApJ*, **585**, 850
- McMullin, J. P., Waters, B., Schiebel, D., Young, W., & Golap, K. 2007, in *Astronomical Society of the Pacific Conference Series*, Vol. 376, *Astronomical Data Analysis Software and Systems XVI*, ed. R. A. Shaw, F. Hill, & D. J. Bell, **127**
- Merello, M., Molinari, S., Rygl, K. L. J., et al. 2019, *MNRAS*, **483**, 5355
- Molinari, S., Baldeschi, A., Robitaille, T. P., et al. 2019, *MNRAS*, **486**, 4508
- Motte, F., Bontemps, S., & Louvet, F. 2018, *ARA&A*, **56**, 41
- Motte, F., Bontemps, S., Schilke, P., et al. 2007, *A&A*, **476**, 1243
- Ohashi, S., Sanhueza, P., Chen, H.-R. V., et al. 2016, *ApJ*, **833**, 209
- Ott, J., Henkel, C., Braatz, J. A., & Weiß, A. 2011, *ApJ*, **742**, 95
- Padoan, P., Pan, L., Juvela, M., Haugbølle, T., & Nordlund, Å. 2020, *ApJ*, **900**, 82
- Palau, A., Zhang, Q., Girart, J. M., et al. 2021, *ApJ*, **912**, 159
- Pan, X., Qiu, K., Yang, K., Cao, Y., & Zhang, X. 2023, *arXiv e-prints*, [arXiv:2312.17455](https://arxiv.org/abs/2312.17455)
- Pillai, T., Kauffmann, J., Wyrowski, F., et al. 2011, *A&A*, **530**, A118
- Pillai, T., Wyrowski, F., Carey, S. J., & Menten, K. M. 2006, *A&A*, **450**, 569
- Pokhrel, R., Myers, P. C., Dunham, M. M., et al. 2018, *ApJ*, **853**, 5
- Qian, L., Li, D., Gao, Y., Xu, H., & Pan, Z. 2018, *ApJ*, **864**, 116
- Rathborne, J. M., Whitaker, J. S., Jackson, J. M., et al. 2016, *PASA*, **33**, e030
- Robitaille, T. & Bressert, E. 2012, *APLpy: Astronomical Plotting Library in Python*
- Röllig, M., Szczerba, R., Ossenkopf, V., & Glück, C. 2013, *A&A*, **549**, A85
- Roman-Duval, J., Jackson, J. M., Heyer, M., Rathborne, J., & Simon, R. 2010, *ApJ*, **723**, 492
- Rosen, A. L., Li, P. S., Zhang, Q., & Burkhart, B. 2019, *ApJ*, **887**, 108
- Rygl, K. L. J., Brunthaler, A., Sanna, A., et al. 2012, *A&A*, **539**, A79
- Sánchez-Monge, Á., Palau, A., Fontani, F., et al. 2013, *MNRAS*, **432**, 3288
- Seiwilo, M., Wiseman, J., Indebetouw, R., et al. 2017, *ApJ*, **849**, 68
- Shu, F., Najita, J., Galli, D., Ostriker, E., & Lizano, S. 1993, in *Protostars and Planets III*, ed. E. H. Levy & J. I. Lunine, **3**
- Singh, A., Matzner, C. D., Friesen, R. K., et al. 2021, *ApJ*, **922**, 87
- Sokolov, V., Wang, K., Pineda, J. E., et al. 2018, *A&A*, **611**, L3
- Swift, J. J., Welch, W. J., & Di Francesco, J. 2005, *ApJ*, **620**, 823
- Tafalla, M., Myers, P. C., Caselli, P., & Walmsley, C. M. 2004, *A&A*, **416**, 191
- Takekoshi, T., Fujita, S., Nishimura, A., et al. 2019, *ApJ*, **883**, 156
- Tang, X. D., Henkel, C., Menten, K. M., et al. 2018, *A&A*, **609**, A16
- Tobin, J. J., Hartmann, L., Chiang, H.-F., et al. 2011, *ApJ*, **740**, 45
- Traficante, A., Fuller, G. A., Duarte-Cabral, A., et al. 2020, *MNRAS*, **491**, 4310
- Traficante, A., Lee, Y. N., Hennebelle, P., et al. 2018, *A&A*, **619**, L7
- Tursun, K., Esimbek, J., Henkel, C., et al. 2020, *A&A*, **643**, A178
- Uyaniker, B., Fürst, E., Reich, W., Aschenbach, B., & Wielebinski, R. 2001, *A&A*, **371**, 675
- Wang, Y., Qiu, K., Cao, Y., et al. 2022, *ApJ*, **927**, 185
- Wendker, H. J., Higgs, L. A., & Landecker, T. L. 1991, *A&A*, **241**, 551
- Wienen, M., Wyrowski, F., Schuller, F., et al. 2012, *A&A*, **544**, A146
- Wolfire, M. G. & Cassinelli, J. P. 1987, *ApJ*, **319**, 850
- Wu, G., Qiu, K., Esimbek, J., et al. 2018, *A&A*, **616**, A111
- Wu, Y., Zhang, Q., Yu, W., et al. 2006, *A&A*, **450**, 607
- Yang, K., Qiu, K., & Pan, X. 2023, *arXiv e-prints*, [arXiv:2312.04880](https://arxiv.org/abs/2312.04880)
- Young, K. E., Lee, J.-E., Evans, Neal J., I., Goldsmith, P. F., & Doty, S. D. 2004, *ApJ*, **614**, 252
- Yue, N.-N., Li, D., Zhang, Q.-Z., et al. 2021, *Research in Astronomy and Astrophysics*, **21**, 024
- Zhang, C.-P., Csengeri, T., Wyrowski, F., et al. 2019, *A&A*, **627**, A85
- Zhang, C.-P., Li, G.-X., Pillai, T., et al. 2020, *A&A*, **638**, A105
- Zhang, Q., Wang, K., Lu, X., & Jiménez-Serra, I. 2015, *ApJ*, **804**, 141
- Zinnecker, H. & Yorke, H. W. 2007, *ARA&A*, **45**, 481

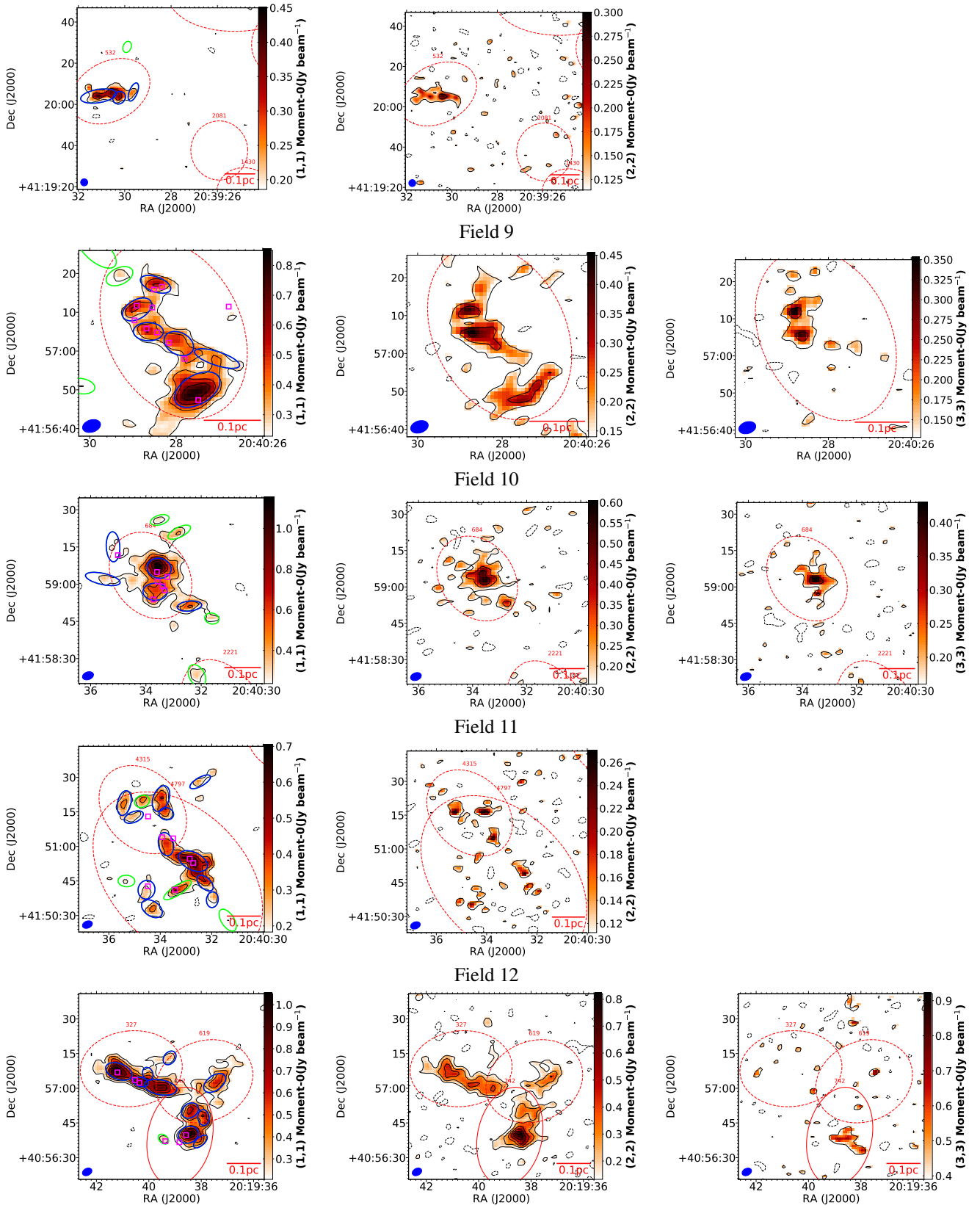
Appendix A: Overview of observations of detected spectral lines



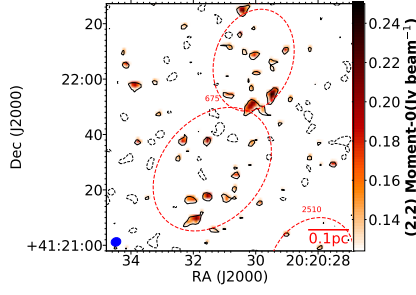
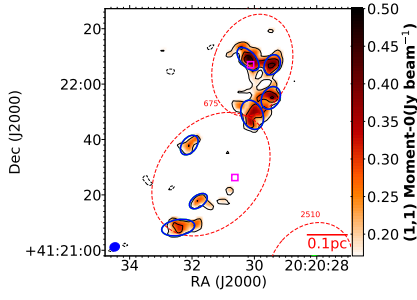
Field 5  
Fig. A.1. continued.



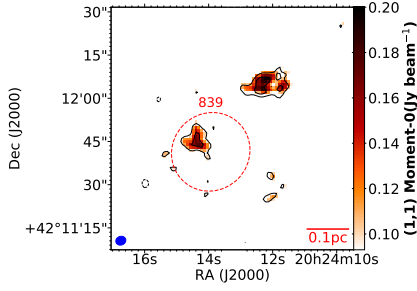
Field 8  
Fig. A.1. continued.



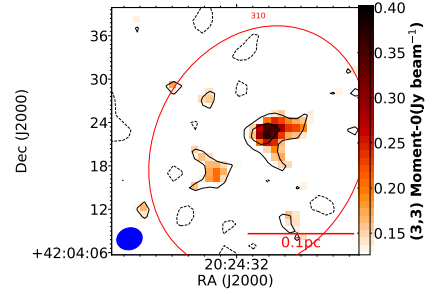
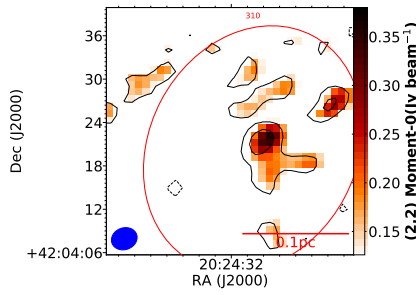
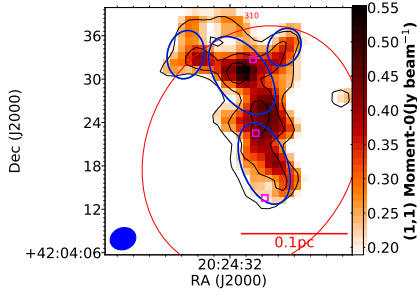
Field 13  
Fig. A.1. continued.



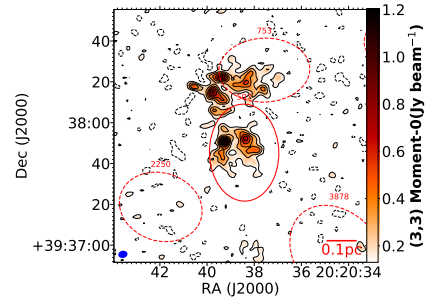
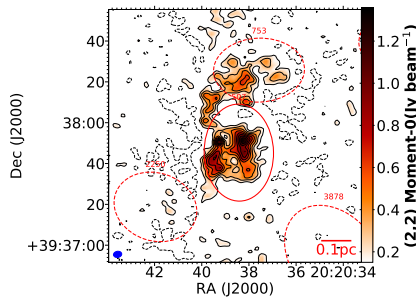
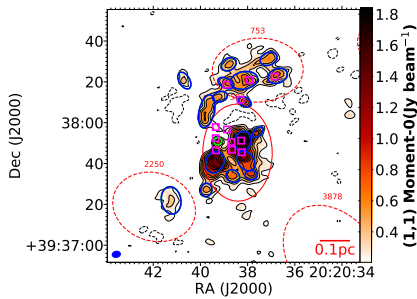
Field 14



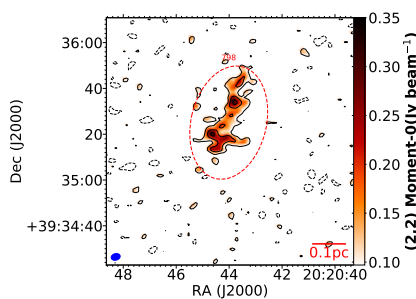
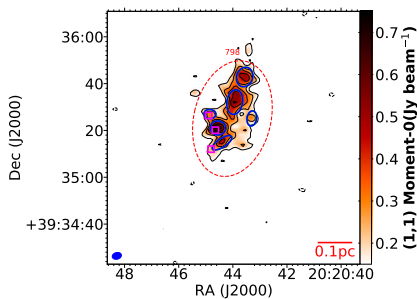
Field 15



Field 16



Field 17



Field 18

Fig. A.1. continued.

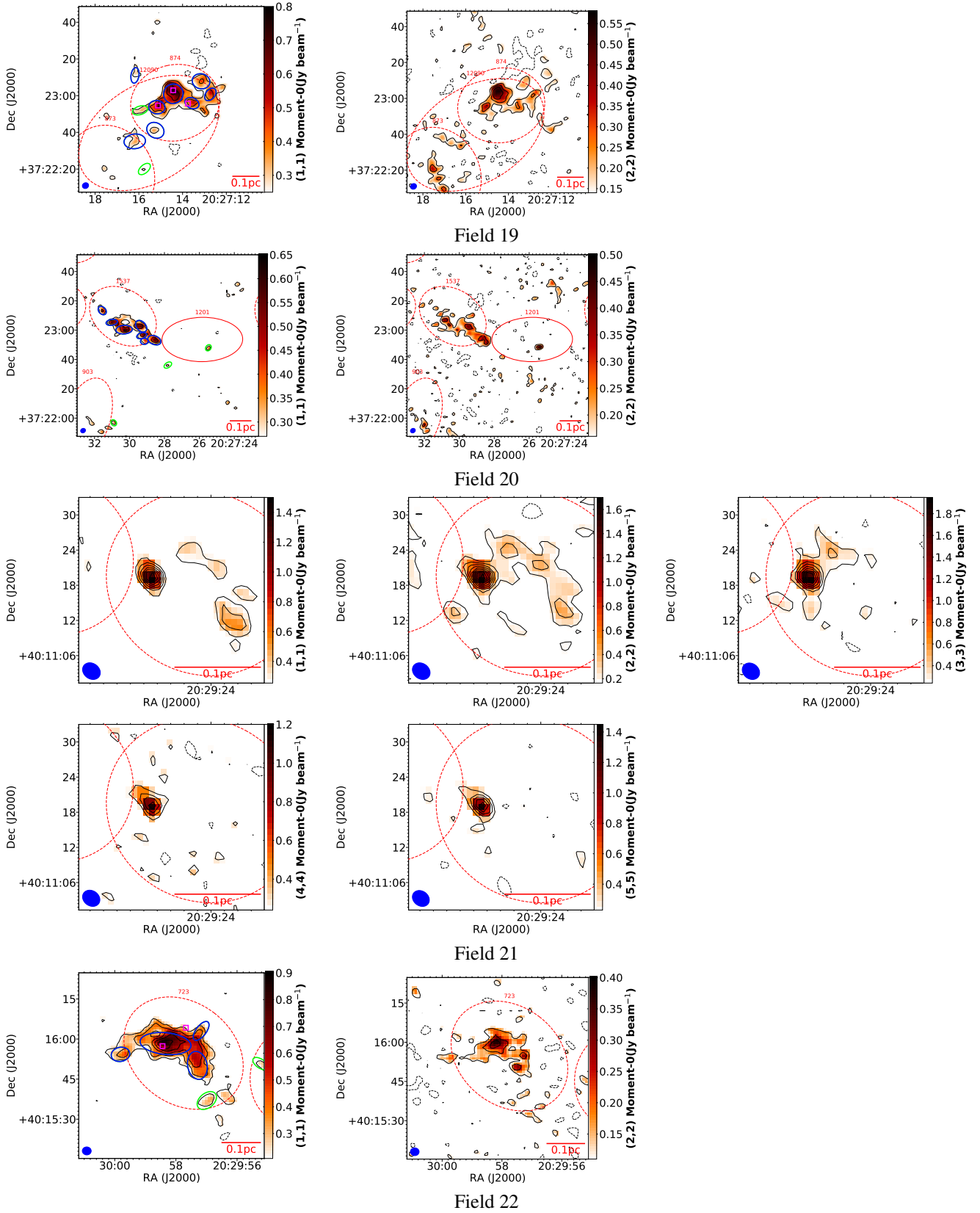


Fig. A.1. continued.

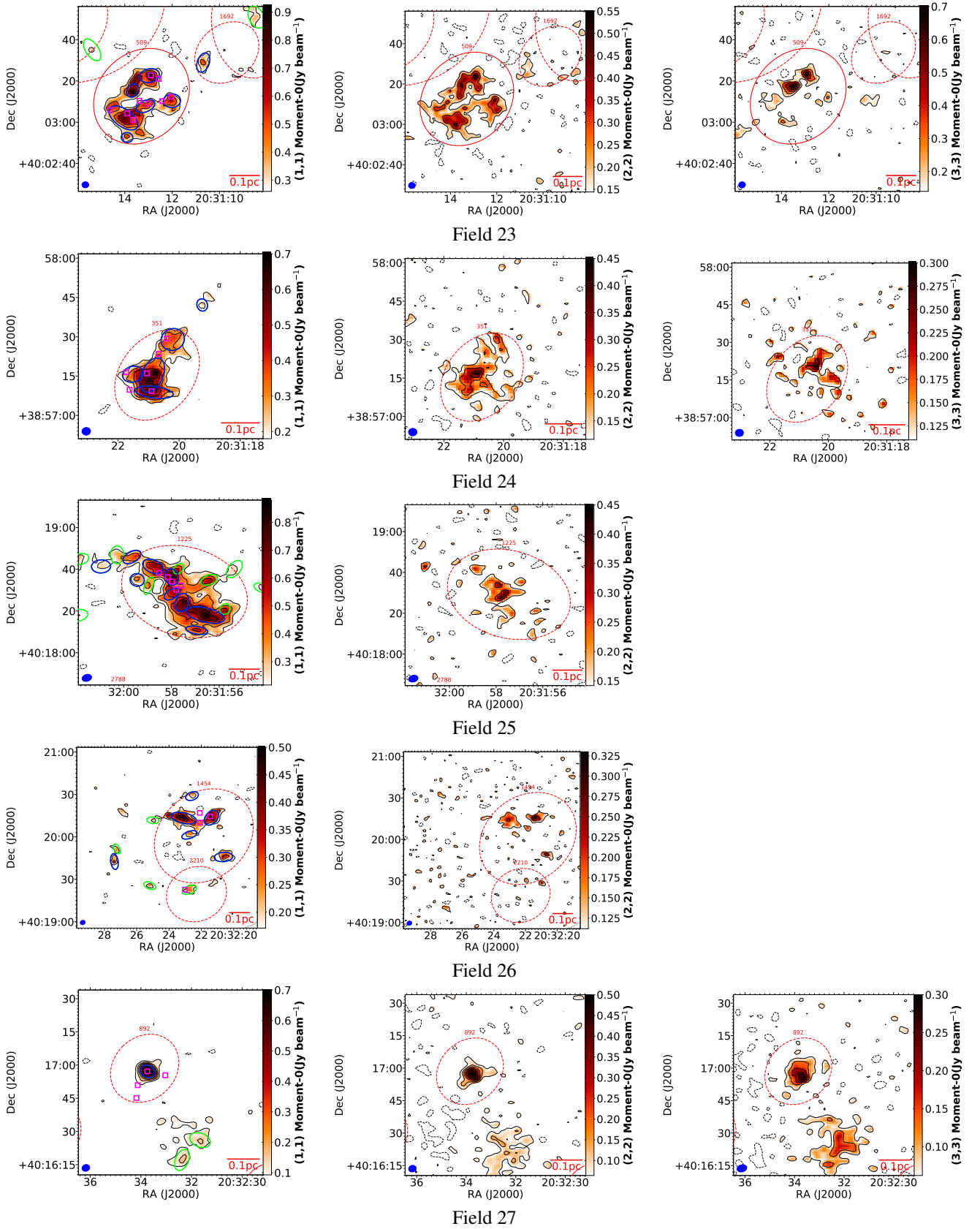


Fig. A.1. continued.

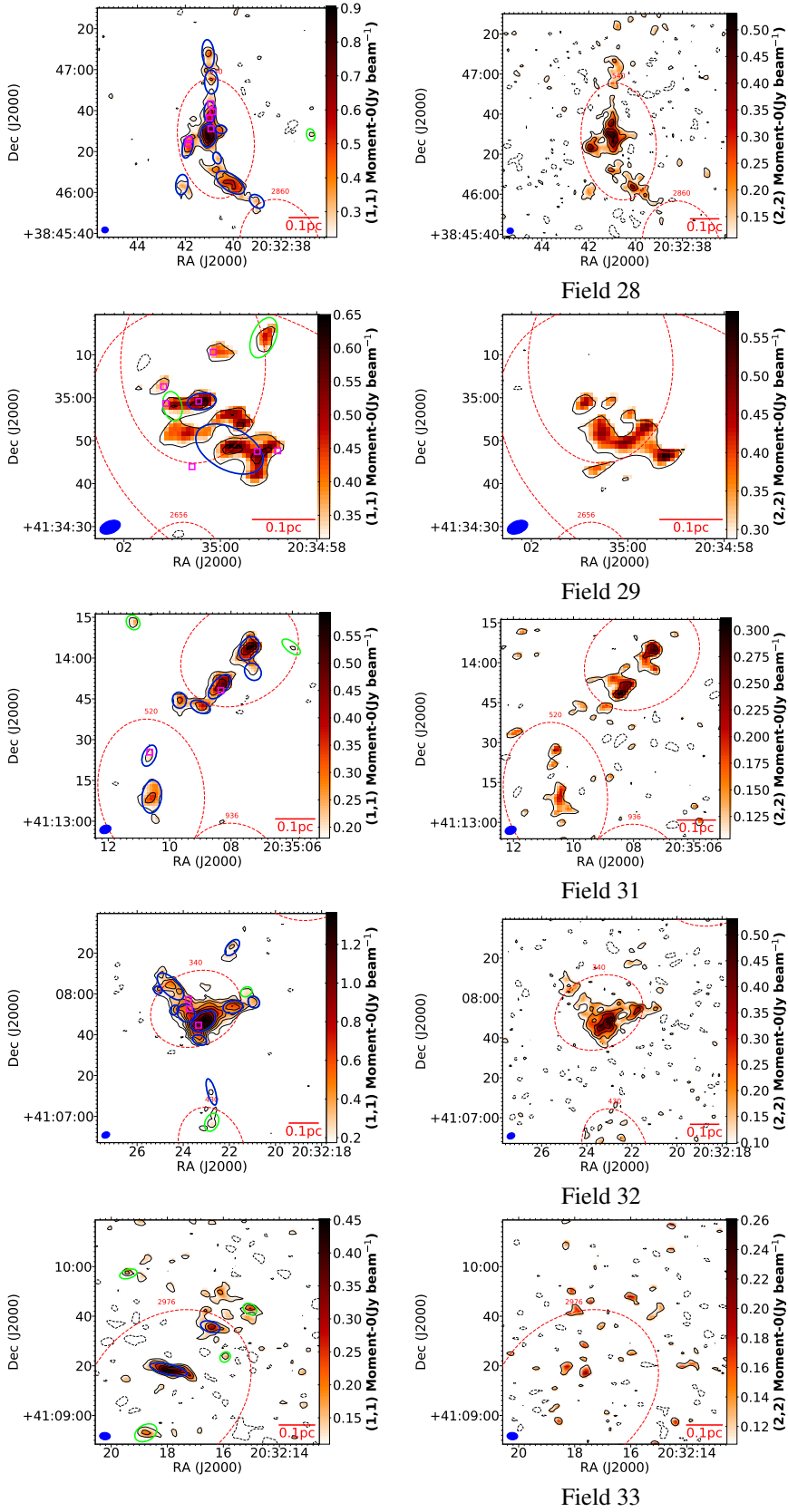
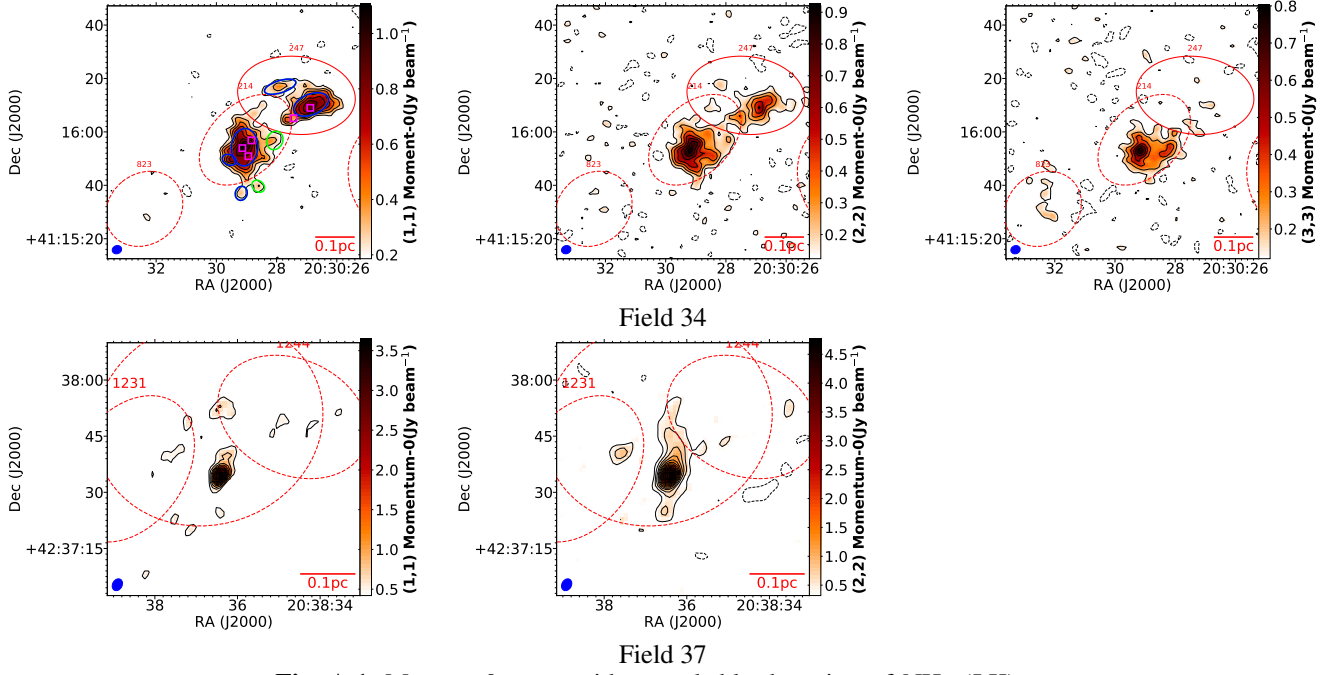
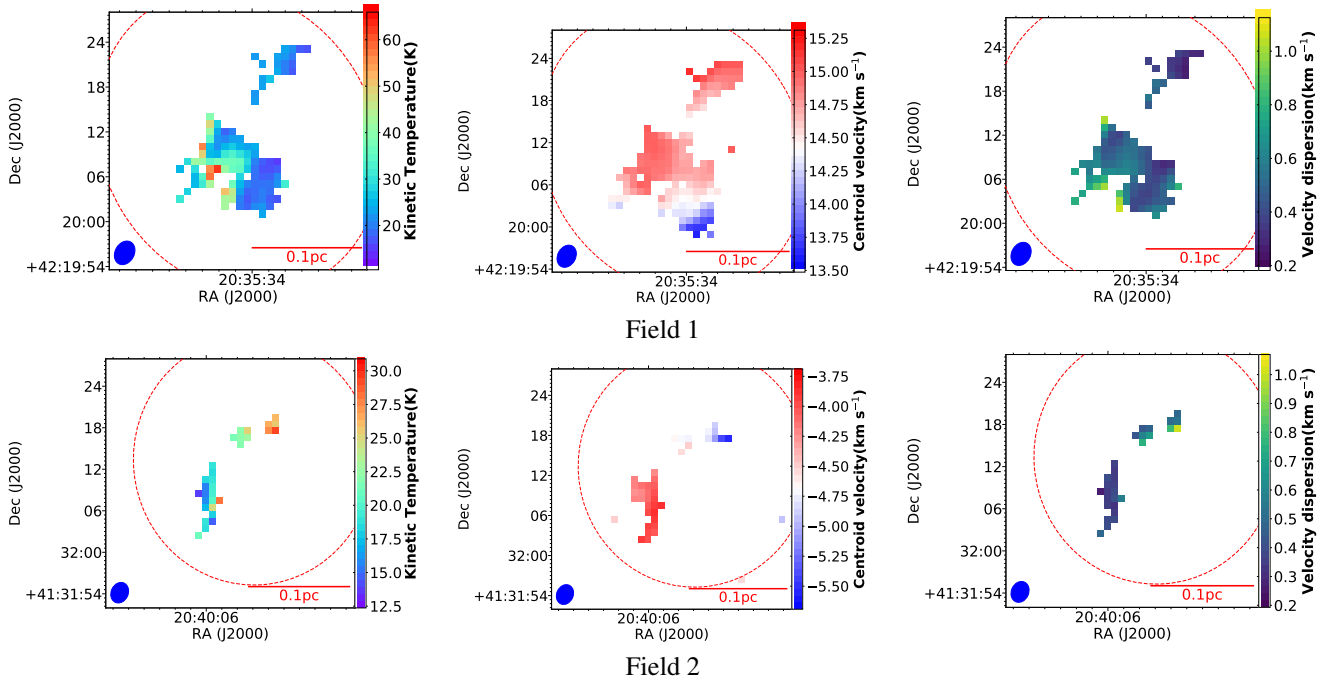


Fig. A.1. continued.



**Fig. A.1.** Moment-0 maps with remarkable detection of  $\text{NH}_3$   $(J,K) = (1,1), (2,2), (3,3), (4,4),$  and  $(5,5)$  inversion lines among our observations. The  $(1,1)$  maps are plotted from a  $3 \text{ rms}$  level and in steps of  $2\sigma$ , while others are plotted from the  $2 \text{ rms}$  level and in steps of  $2\sigma$ . The IR-bright, IR-quiet, and starless MDCs are shown as red solid, red dashed, and pink dashed ellipses, respectively. The smaller ellipses present the fragments extracted using the GAUSSCLUMPS algorithm. The blue ones are included in the parameter analysis while the green ones are not.

## Appendix B: Distributions of kinetic temperature, centroid velocity and velocity dispersion



**Fig. B.1.** continued.

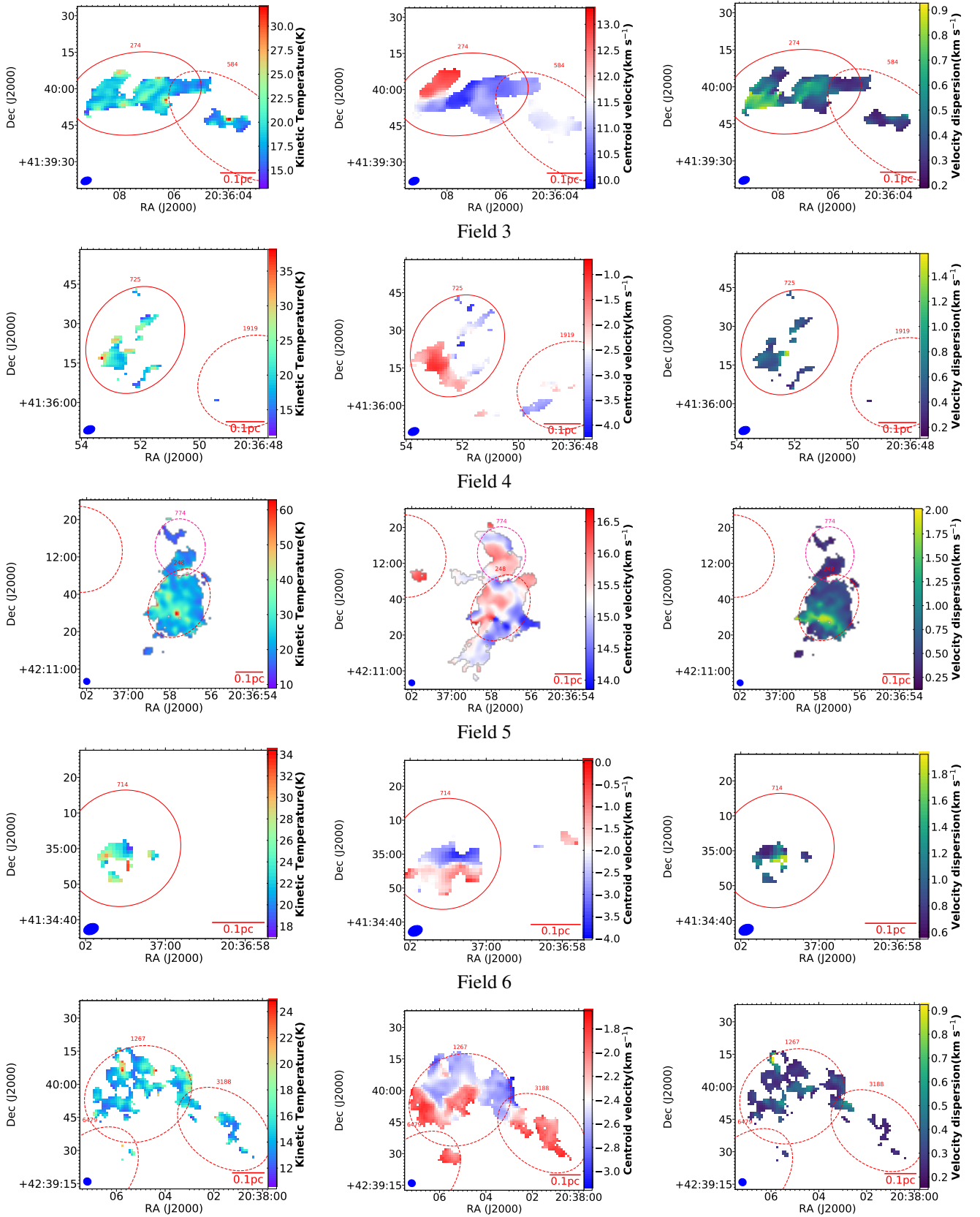
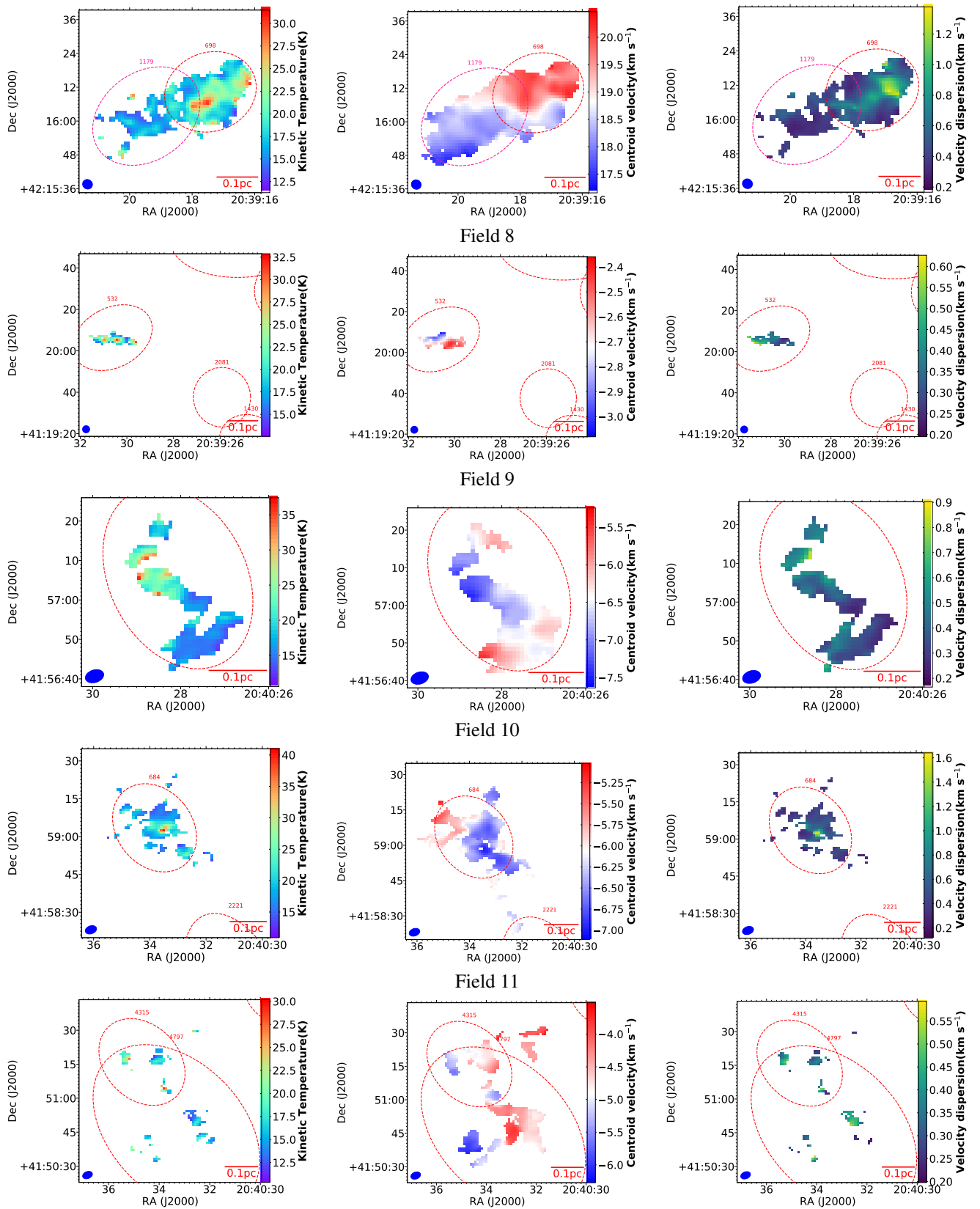
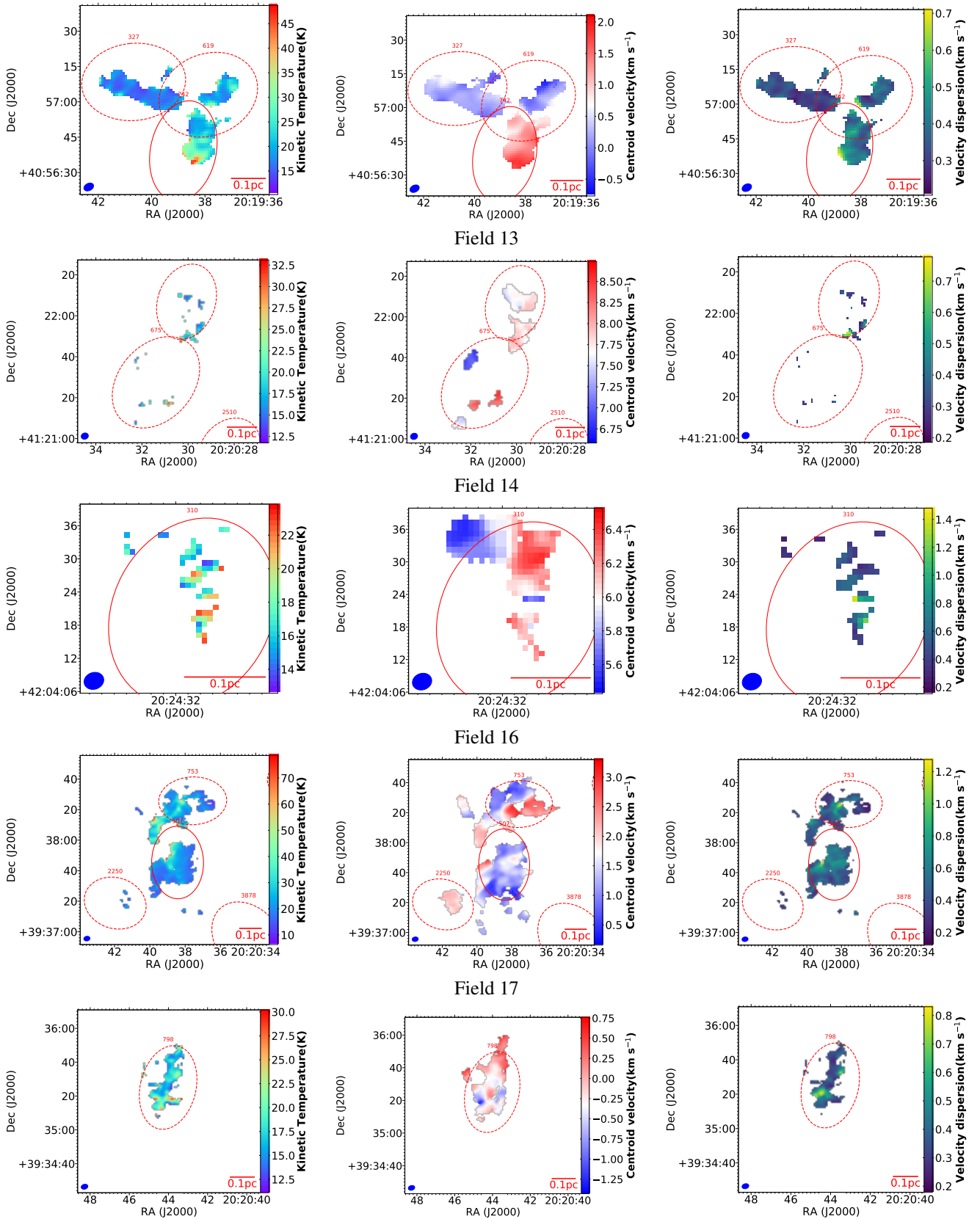


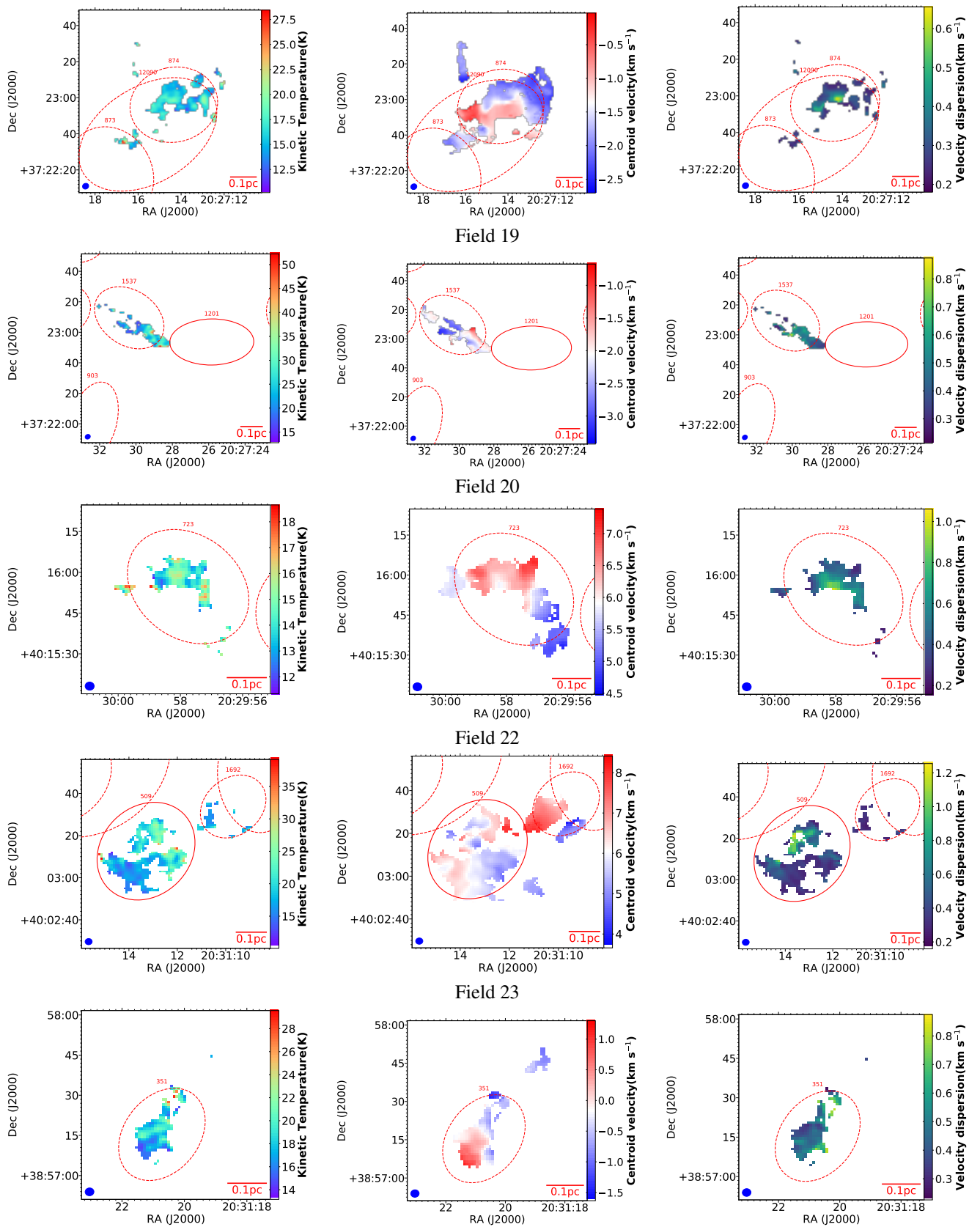
Fig. B.1. continued.



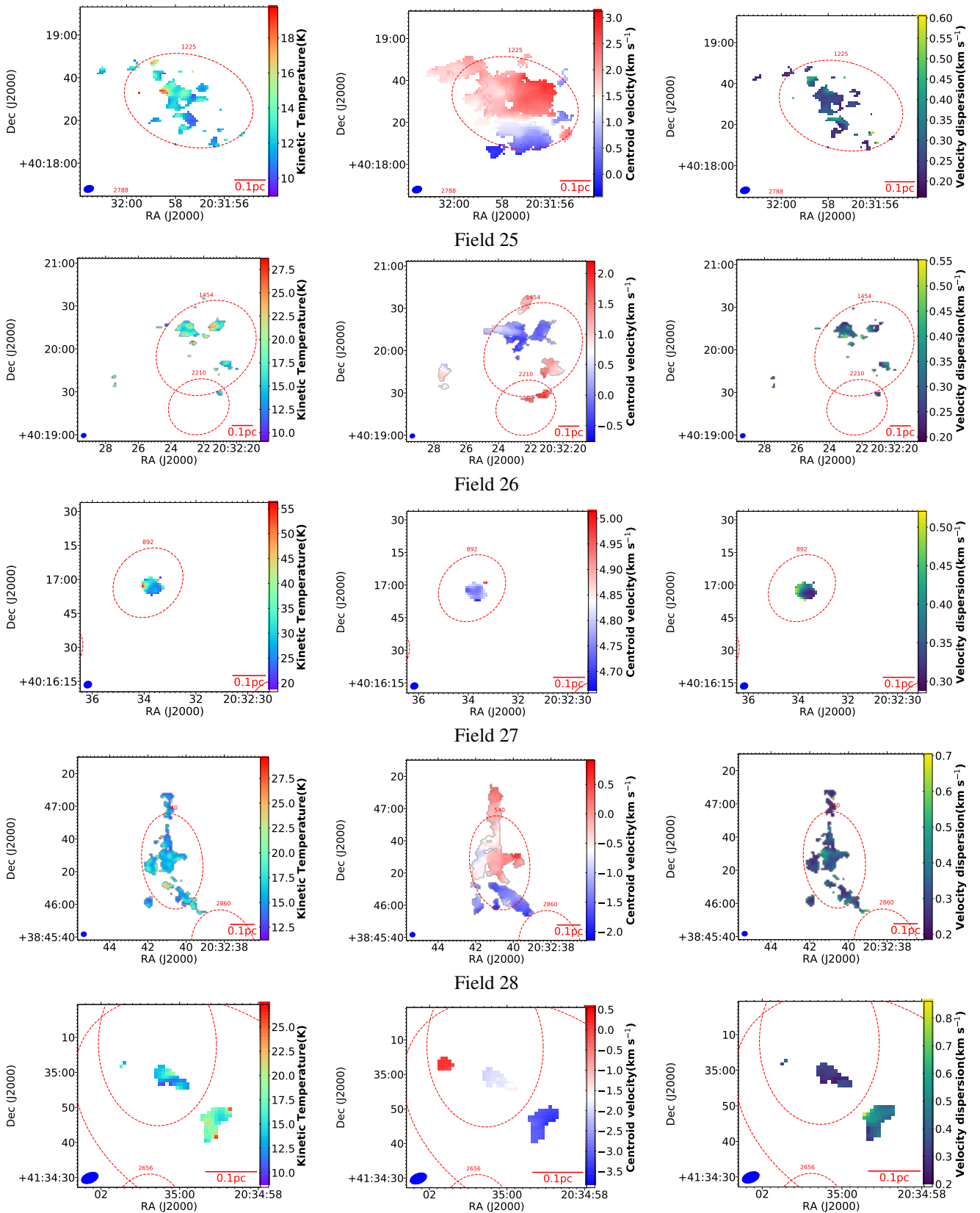
Field 12  
Fig. B.1. continued.



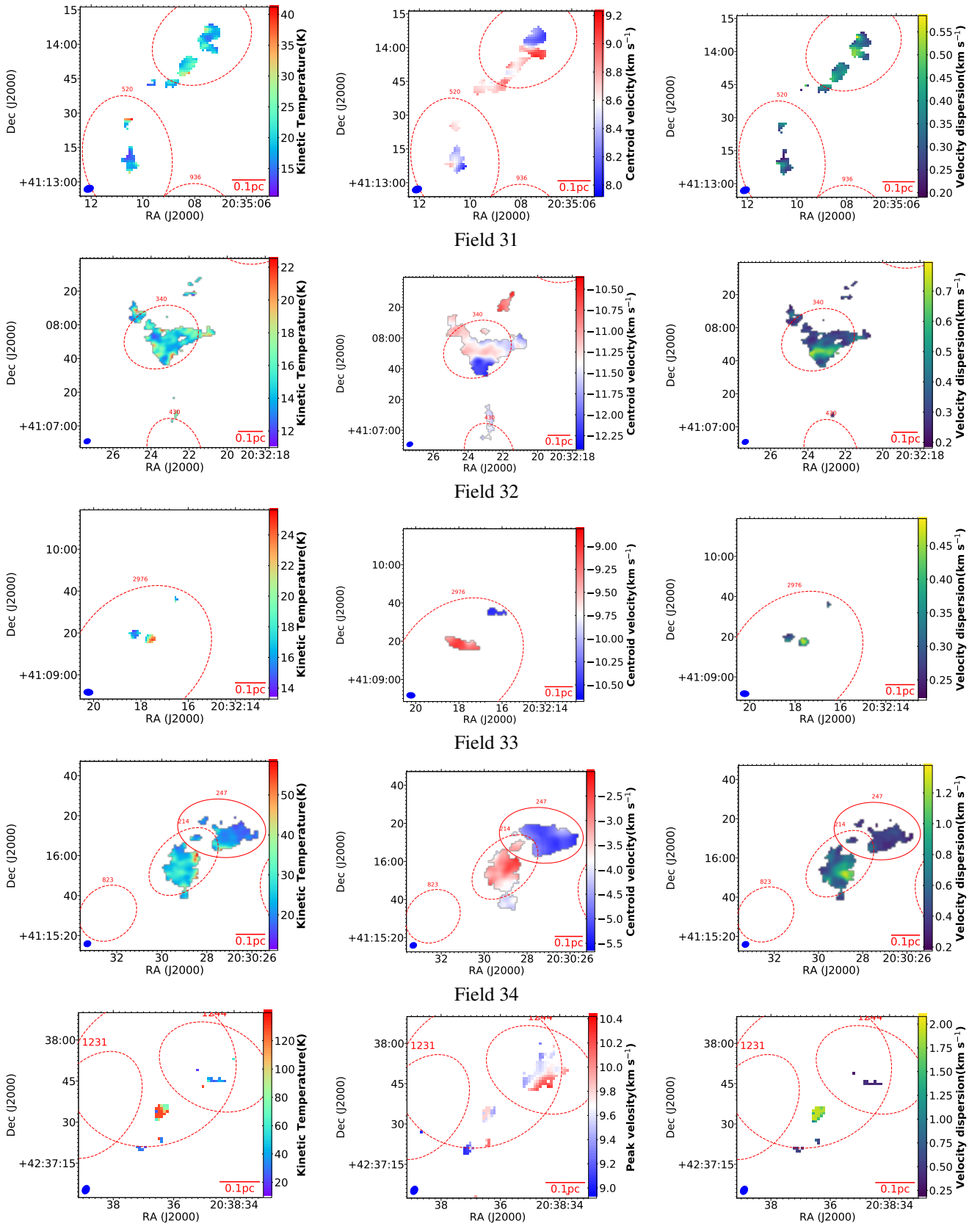
Field 18  
**Fig. B.1.** continued.



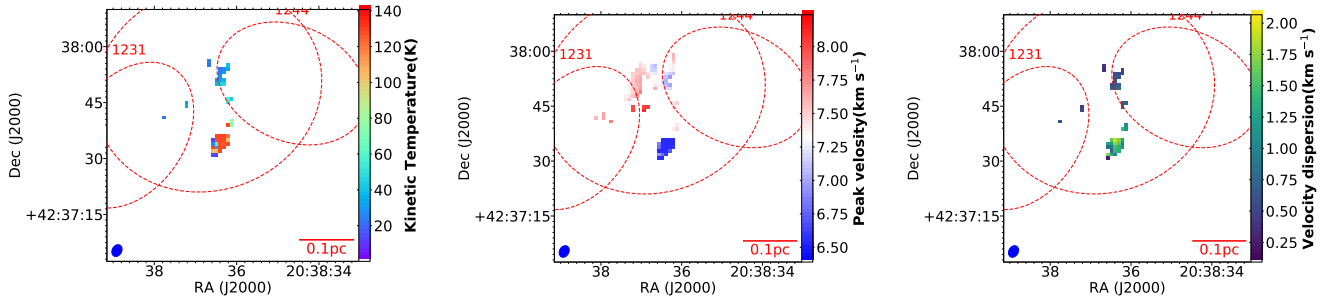
Field 24  
**Fig. B.1.** continued.



Field 29  
Fig. B.1. continued.



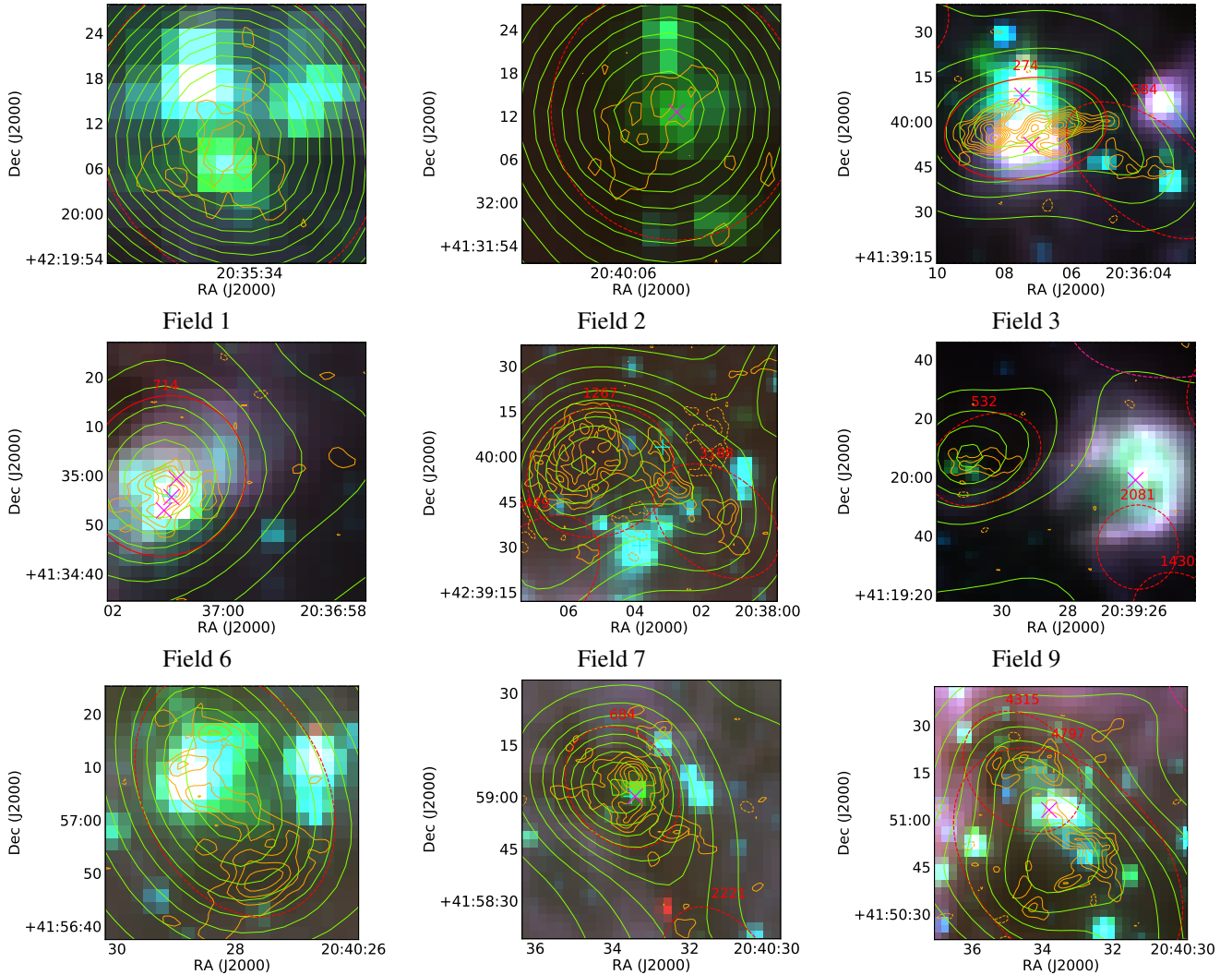
Field 37 - Component 1  
Fig. B.1. continued.



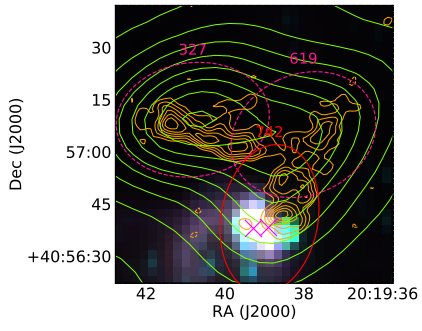
Field 37 - Component 2

**Fig. B.1.** Distributions of kinetic temperature (left panel), centroid velocity (middle panel), and velocity dispersion (right panel) derived from the simultaneous fitting of NH<sub>3</sub> (1,1) and (2,2) inversion lines. The ellipses are the same as those in Fig. A.

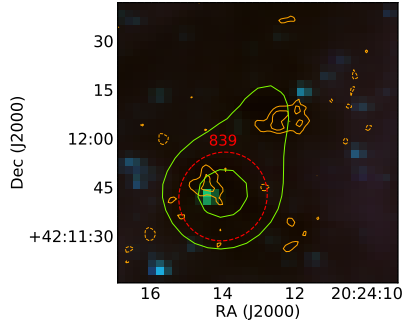
### Appendix C: Compositive images



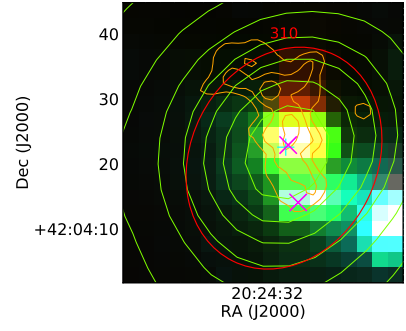
Field 11  
**Fig. C.1.** continued.



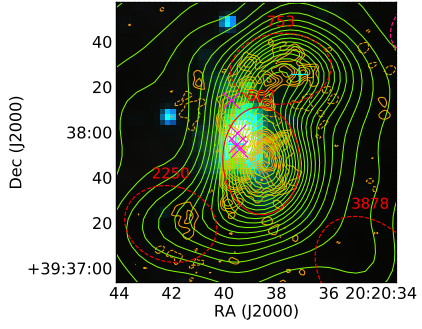
Field 13



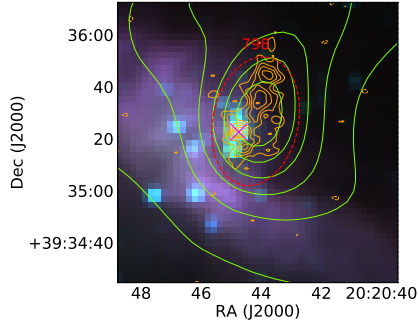
Field 15



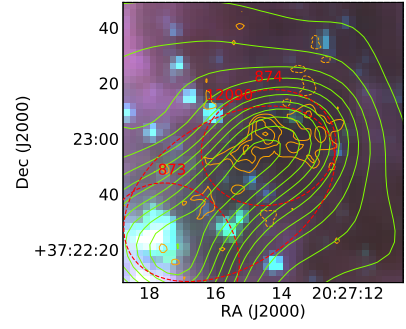
Field 16



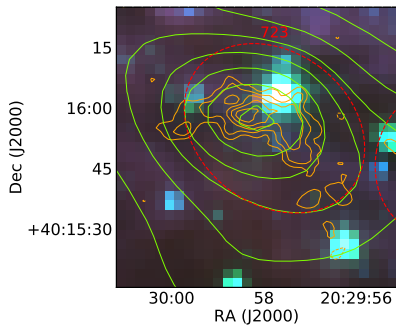
Field 17



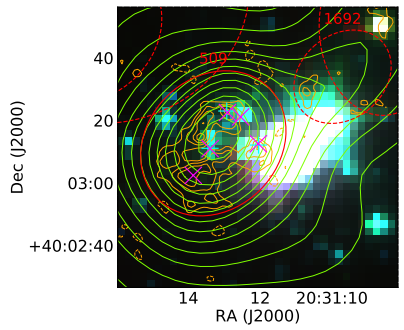
Field 18



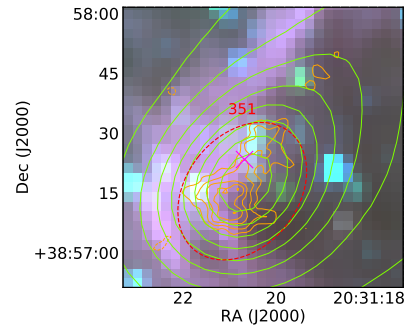
Field 19



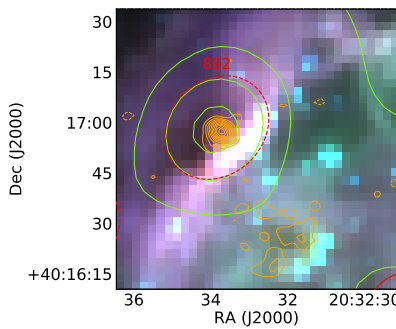
Field 22



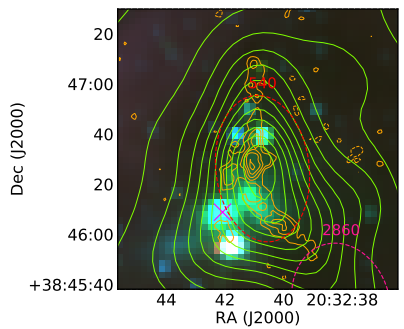
Field 23



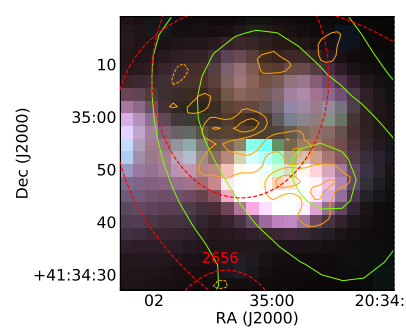
Field 24



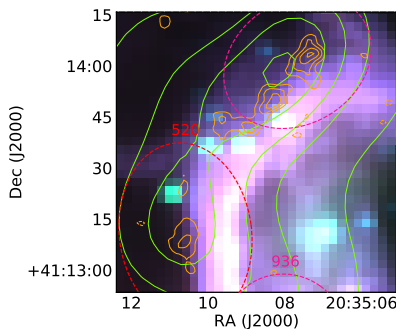
Field 27



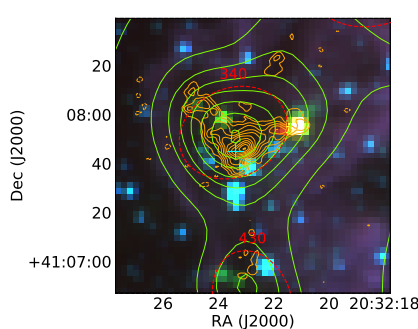
Field 28



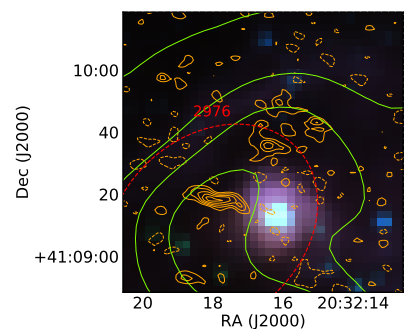
Field 29



Field 31

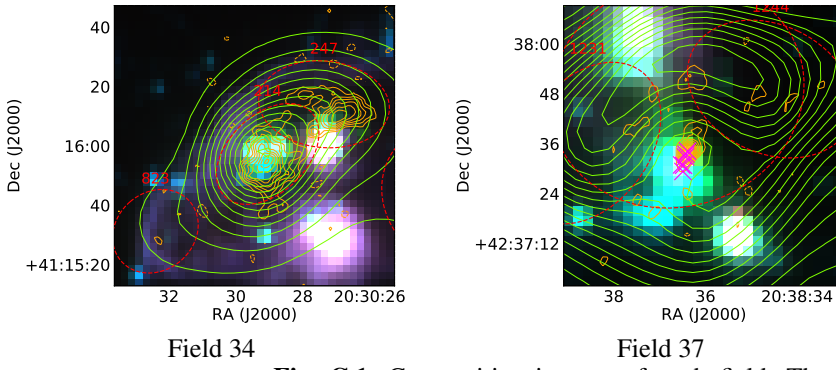


Field 32



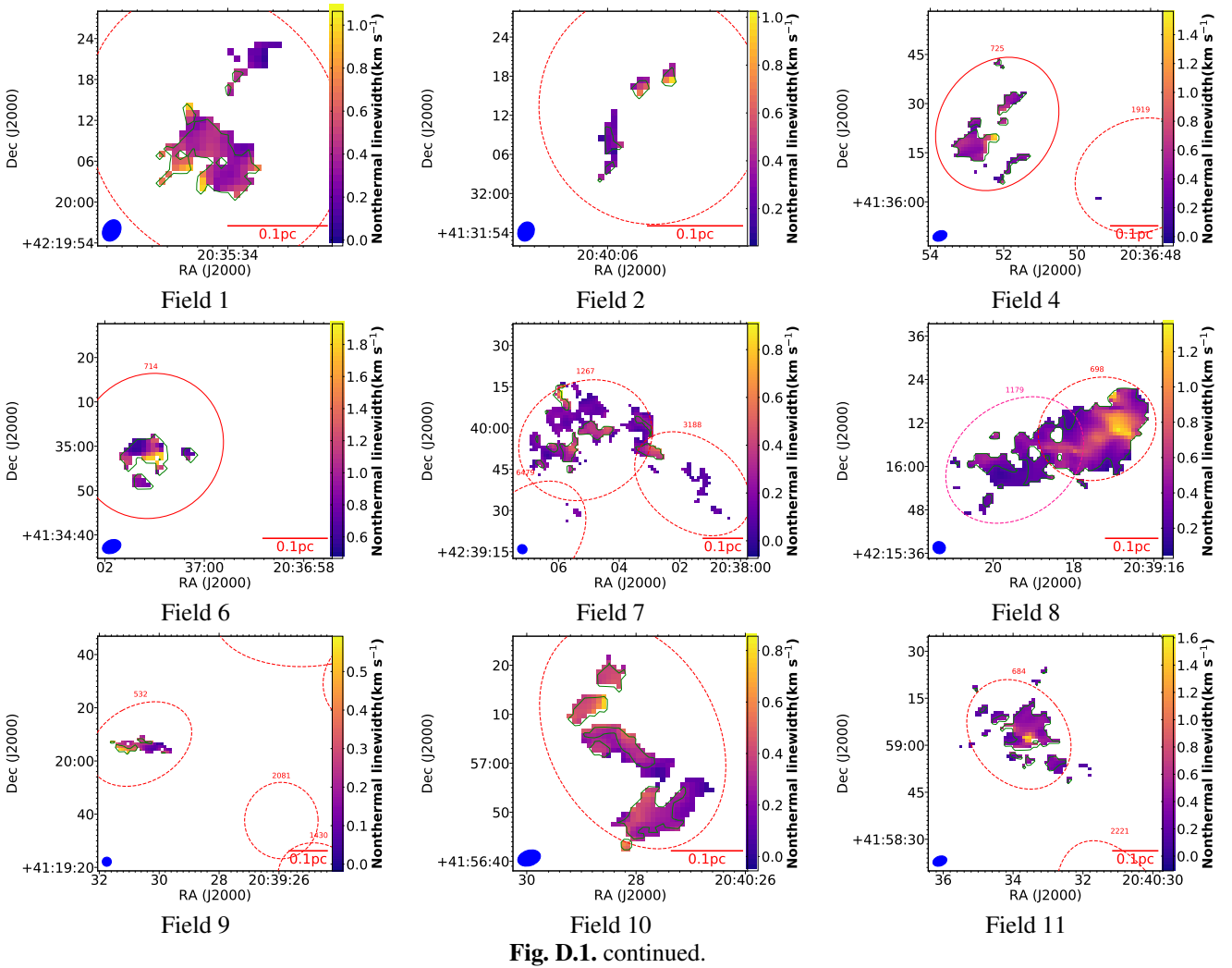
Field 33

Fig. C.1. continued.



**Fig. C.1.** Composite images of each field. The background is the *Spitzer* three-color images using 8 $\mu$ m (R), 4.5 $\mu$ m (G), and 3.6 $\mu$ m (B) bands. The column density contours and NH<sub>3</sub> (1,1) integrated emission contours are over-plotted with green and orange. Cyan and magenta crosses mark the positions of any H<sub>2</sub>O masers or radio continuum sources, respectively. The ellipses are the same as those in Fig. A.

### Appendix D: Maps of non-thermal velocity dispersion



**Fig. D.1.** continued.

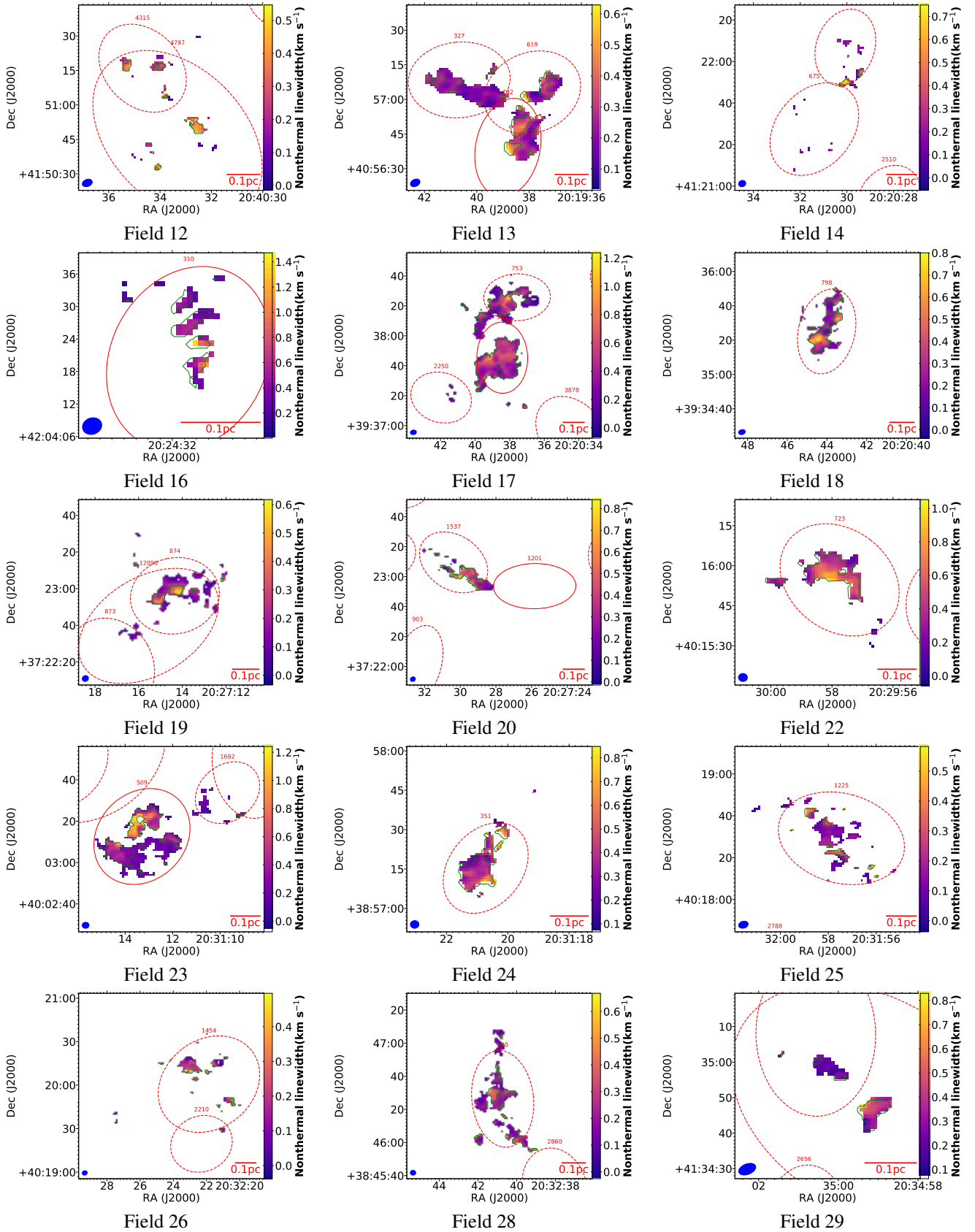
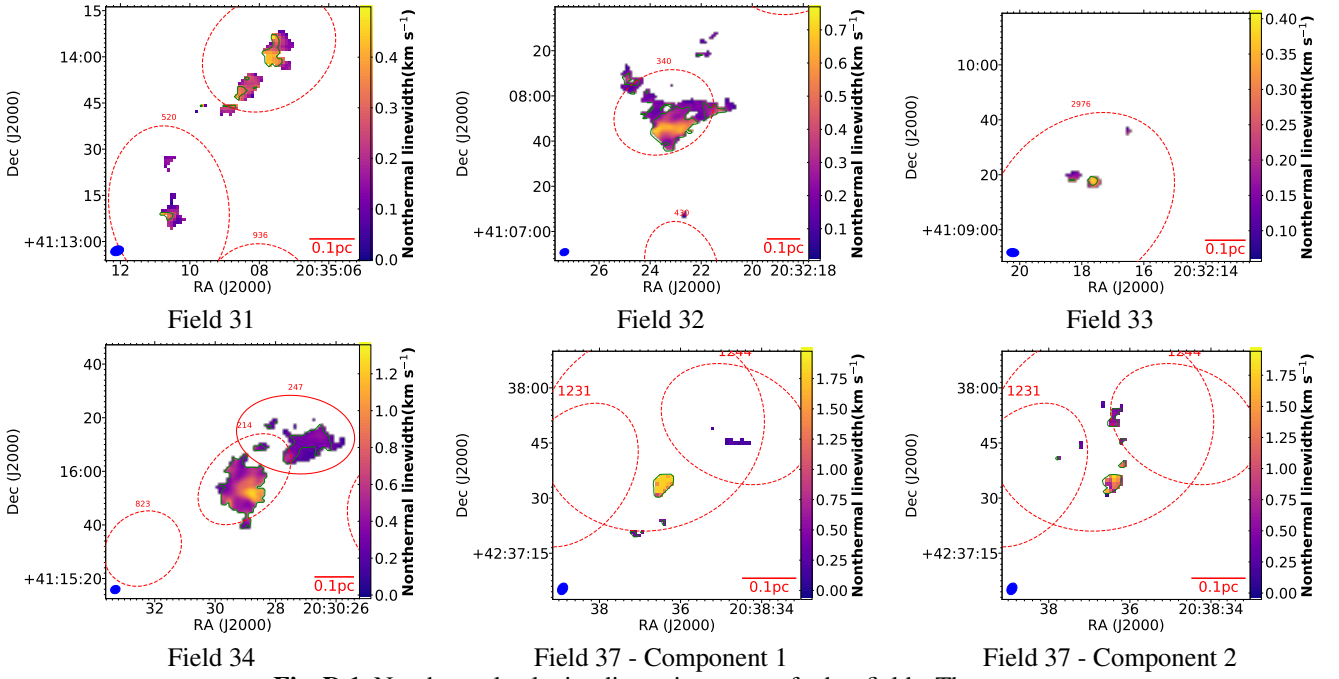


Fig. D.1. continued.



**Fig. D.1.** Nonthermal velocity dispersion maps of other fields. The green enclosing areas show the regions with Mach numbers larger than 1. The ellipses are the same as those in Fig. A.

## Appendix E: Derivation of different velocity dispersions

There are three velocity dispersions used in our analyses of MDCs and NH<sub>3</sub> fragments: the total velocity dispersion  $\sigma_v$ , the nonthermal velocity dispersion including the bulk motions  $\sigma_{v,NT}$ , and the nonthermal velocity dispersion excluding the bulk motions  $\sigma_{v,ng}$ .

First, for the total velocity dispersion,  $\sigma_v$ , both the velocity dispersion of a certain beam,  $\sigma_{v,i}$ , and the gradient of  $v_{lsr}$  need to be taken into account. The mean value of  $\sigma_{v,i}$  is calculated as root mean square (RMS) weighed by the integrated flux of the (1,1) line; that is,

$$\overline{\sigma_{v,i}} = \sqrt{\Sigma(w \times \sigma_{v,i}^2) / \Sigma(w)}, \quad (\text{E.1})$$

where  $w$  is the integrated flux of the NH<sub>3</sub> (1,1) line from their moment-0 maps. The contribution of  $v_{lsr}$  is derived as

$$\Delta v_{lsr} = \sqrt{\Sigma[w \times (v_{lsr,i} - \overline{v_{lsr,i}})^2] / \Sigma(w)}, \quad (\text{E.2})$$

where  $v_{lsr,i}$  is the centroid velocity of a certain beam, and  $\overline{v_{lsr,i}} = \Sigma(w \times v_{lsr,i}) / \Sigma(w)$  is the weighted mean value  $v_{lsr,i}$ . Here,  $\sigma_v$  is then derived as

$$\sigma_v = \sqrt{\overline{\sigma_{v,i}}^2 + \Delta v_{lsr}^2}. \quad (\text{E.3})$$

Generally,  $\sigma_v$ , including all the observed motions, is used in the virial analysis.

Similarly,  $\sigma_{v,NT}$  is calculated as the weighted RMS value from the nonthermal velocity dispersion maps combined with the contribution of  $v_{lsr}$ , which is

$$\sigma_{v,NT} = \sqrt{\Sigma(w \times \sigma_{v,NTi}^2) / \Sigma(w) + \Delta v_{lsr}^2}, \quad (\text{E.4})$$

where  $\sigma_{v,NTi}$  is the nonthermal velocity dispersion of a certain beam.

In order to calculate  $\sigma_{v,ng}$ , we fit the bulk motions of  $v_{bm}$  with a 2D linear function on the centroid velocity maps following the method provided in Goodman et al. (1993):

$$v_{bm} = v_0 + a \times \delta\alpha + b \times \delta\beta, \quad (\text{E.5})$$

where  $\delta\alpha$  and  $\delta\beta$  are the offsets in right ascension (RA) and declination (Dec). Then, the contribution of the bulk motion is estimated as

$$\Delta v_{bm} = \sqrt{\Sigma[w \times (v_{bm,i} - \overline{v_{bm,i}})^2] / \Sigma(w)}, \quad (\text{E.6})$$

where  $v_{bm,i}$  is the fitted velocity of a certain beam. Deducting  $\Delta v_{bm}$  from  $\sigma_{v,NT}$ , we can obtain  $\sigma_{v,ng}$  as

$$\sigma_{v,ng} = \sqrt{\sigma_{v,NT}^2 - \Delta v_{bm}^2}. \quad (\text{E.7})$$

Both  $\sigma_{v,NT}$  and  $\sigma_{v,ng}$  are used in the calculation of the Mach numbers of different molecular structures.